Quantum sensing with large two-dimensional crystals of ions in a Penning trap

by

Kevin A. Gilmore

B.S., B.A., Auburn University, 2013

A thesis submitted to the

Faculty of the Graduate School of the

University of Colorado in partial fulfillment

of the requirements for the degree of

Doctor of Philosophy

Department of Physics

2020

Committee Members:

Ana Maria Rey, Chair

John Bollinger

Murray Holland

James Thompson

Longji Cui

Gilmore, Kevin A. (Ph.D., Physics)

Quantum sensing with large two-dimensional crystals of ions in a Penning trap

Thesis directed by Prof. Ana Maria Rey and Dr. John Bollinger

Quantum sensing protocols using trapped-ions can enable detection of weak electric fields by sensing displacements surpassing the Standard Quantum Limit (SQL) – the sensitivity achievable with a coherent state. This thesis will focus on recent work directed towards enhancing the capabilities of the NIST Penning trap platform and, in particular, pushing the limits of displacement and electric field sensing with hundreds of ions in a two-dimensional crystal.

Preparing a quantum system in its ground state can be advantageous. In particular, for the trapped ion experiments performed with the NIST Penning trap, motional ground state cooling can enhance the fidelity of quantum simulation experiments as well as heighten the sensitivity of displacement amplitude and electric field sensing measurements. By exploiting the phenomena of electromagnetically-induced transparency, we demonstrate near ground state cooling of all the axial modes of over one hundred ions in a two-dimensional crystal.

Additionally, we present results for a series of quantum sensing experiments. By employing spin-dependent optical dipole forces to couple mechanical motion of the ions to their spin states, the displacement of the ion crystal can be read out through measurements of the spin state. Initial experiments were conducted far off-resonance from the center-of-mass (COM) mode. In this regime, free from thermal and frequency noise of the COM mode, measurements imply an imprecision for resolving the displacement of an ion crystal in a single measurement that is 30dB smaller than the ground state wave function extent. Probing on-resonance with the COM mode provides the maximum sensitivity to electric fields, though this sensitivity will be limited by the frequency stability of the mode. Recently, displacements of 7dB below the SQL are detected in a single measurement and an electric field of 250 nV/m is measured in 1 second.

Dedication

For Mom and Dad.

Acknowledgements

There are many people whose contributions - scientific, personal, or both - I gratefully acknowledge. I am deeply thankful for the support I have received from so many friends, colleagues, and mentors. I will do my best to give credit and share my appreciation for the effort all these people have made, and apologize in advance for any names unintentionally left out.

First, I'd like to thank the entire Ion Storage group for making NIST a great place to work. I've had the tremendous pleasure of working and interacting with so many fantastic scientists and wonderful people in my time here. There is not space to list every one of you, but to all the Ions I overlapped with: thank you.

The Penning trap team has been a small but close-knit group, and everyone has made critical contributions to the work I describe in this thesis. Joe Britton, Brian Sawyer, and Justin Bohnet built the current apparatus, and so it is upon their shoulders I stand. All that I describe in this document is the result of extensions to their efforts - I am intellectually indebted to each of them. In my early days in the lab, Joe and Justin got me up to speed and taught me a lot about what being a physicist is about. I am personally and professionally grateful for this. In the following years, I had the pleasure of working closely with Elena Jordan and Matt Affolter. They both played prominent roles in the research I present here (Elena with the EIT cooling, and Matt with the displacement sensing) and I am certain we would not have had these successes without them. I have greatly enjoyed their company both in the lab and outside of it. Thank you for your colleagueship and your friendship. We have had many fruitful collaborations with the theory groups of Murray Holland and Ana Maria Rey at JILA, and both Murray and Ana Maria have been instrumental in guiding

our work. Thank you to Athreya Shankar, Robert Lewis-Swan, Arghavan Safavi-Naini, and Diego Barbarena for all your hard work, guidance, and answers to stupid experimentalist questions.

Most importantly, I want to thank John Bollinger, my advisor. John is a brilliant physicist and the mastermind of the NIST Penning trap experiment, and also just generally a really great person. Without him, there would be nothing else in this document. Thank you, John, for giving me the chance to work on this project and for the years of support and direction. And thanks to you and Lynn for sharing your home and hospitality with me. It has been a privilege to work with you.

In graduate school, I have been fortunate to have a supportive group of friends. Thank you Bryan, Dan, Karl, Tim, Shaun and Caroline, Peter, Zach, Ryan and Jackie, Stijn and Julia, Laura, and Katy for everything over the last few years. Especially thanks to Raghu and Nigel, who have been confidants, sounding boards, and a lot of fun. Since college, Joey, Matt, Kathryn, and Phillip have been true and steady friends, through good times and bad. Thank you for being there for me. The guys from Pace have held together for more than 10 years now: Michael, Scott, Tim, and Ben, thanks for sticking with me all this time.

My parents, Roger and Casey, and brothers, Nathan and Hayden, have been a constant source of support. This PhD has been a long time coming, and you have been there every step of the way. Thank you for everything.

Finally, and perhaps most importantly, is Koshka and also Quito - the cats. They have been a furry source of stress relief, fun, and affection.

Actually, the most important person is the one who has been with me every day for the last six years, and without whom I don't imagine I'd have gotten this far without. Gargi, you have been a light in the dark and an endless source of love and support. Thank you.

Contents

Tables

Table

Figures

Figure

Chapter 1

Introduction

Trapped ions are an ideal platform for testing both fundamental and applications driven research in quantum physics. In particular, the fields of quantum metrology and quantum information processing are rich and fruitful to explore, and offer the promise of quantum enhancement over classical alternatives. Much of this promise relies on the ability to perform well-controlled measurements with many interacting quantum elements. Thus, there is motivation to test the limits of large systems: in this case, large arrays of trapped ions. This is the objective of the NIST Penning trap.

This thesis will focus on recent work directed towards enhancing the capabilities of the NIST Penning trap platform and, in particular, pushing the limits of displacement and electric field sensing with trapped ions.

1.1   Quantum sensing

Quantum sensing refers to the use of a quantum mechanical system as a tool for measurement. A quantum sensor turns the inherent fragility of quantum systems into a useful feature: sensitivity to external perturbations. A prominent type of quantum sensor - and the variety pertinent to this work - uses a two-level system, or qubit, as the sensitive quantum system. Implementations of two-level quantum sensors include the electronic, magnetic, vibrational, or motional levels of neutral and Rydberg atoms, solid-state spins, superconducting circuits, or trapped-ions.

Following [1] and in analogy to the DiVincenzo criteria for quantum computing [2], there are

several attributes required for this type quantum sensor:

(1) Two levels separated by a transition energy $E = \hbar\omega$;

(2) Initialization into a known state and read out of the final state;

(3) Coherent manipulation of the spin(s);

(4) Interaction with a physical quantity leading to a shift in or transition between the energy levels.

So, with a two-level system prepared in a particular state and coupled to an external physical quantity (for example, an electric field) a shift in the transition frequency can be read out in some fashion. A typical measurement (and again, relevant for this work) might use Ramsey interferometry [3, 4]. For the trapped-ion sensor, a coupling between the spin and motional degrees of freedom (produced via a spin-dependent optical dipole force) provides the link between the measured transition frequency and the external perturbation (an electric field).

Such a quantum sensor need not necessarily improve the sensitivity beyond what is classically possible by making use of entanglement. However, we can refer to entanglement-assisted sensing as 'quantum-enhanced', which requires more than one qubit [5, 6]. Maximally entangled states can allow for a Heisbenberg-limited measurement, with a scaling that goes as $1/N$ (as opposed to $1/\sqrt{N}$). As a result, a system with large N is (more) advantageous for quantum-enhanced measurement.

1.2   Penning trap platform

The NIST Penning trap is a novel platform that has been useful in exploring a variety of physics. Large numbers of ions can be confined and controlled in a Penning trap and subsequently cooled into a Coulomb crystal. From here, lasers can be used to address the ions and produce a coupling between the spin and motional degrees of freedom. In trapped-ions, this spin-motion coupling allows for high fidelity quantum logic gates [7, 8], engineering Ising interactions [9, 10, 11],

and measuring displacements [12]. Recent work has focused on quantum metrology and quantum simulation [13, 14, 15, 16]. The combination of a large and well-controlled quantum system makes this an appealing platform for pushing the limits of quantum physics experiments.

1.3   Overview of thesis

This thesis will focus on four sets of experiments performed with the NIST Penning trap. The first, in Ch. 5, achieved near-ground state cooling of all the axial drumhead modes of more than 100 ions [17]. The other three are a continuum of experiments related to testing the limits of the sensitivity of our system to displacements due to electric fields [18, 19]. Chapter 6 covers a pair of experiments where center-of-mass motion is driven at frequencies far detuned from any of the motional modes of the ion crystal, providing a lower limit to the displacements that can be resolved. Chapter 7 summarizes recent, as-of-yet unpublished work wherein the center-of-mass mode of the ion crystal is resonantly excited and subsequently detected, allowing for greatly enhanced sensitivity to electric fields and surpassing the standard quantum limit for both displacement and electric field sensing.

In addition to detailing these results, this thesis will also give an overview of the relevant physics (Ch. 2) and the NIST Penning trap apparatus (Ch. 3), as well as details of the calibration and alignment procedures used (Ch. 4). Finally, the results will be summarized and some future directions outlined in Ch. 8.

Chapter 2

Trapped ion physics in a Penning trap

Trapped ions are an appealing platform for quantum sensing experiments. In this section, I describe some basics of ion trapping focusing on the type of trap relevant for this work: a Penning trap.

2.1 Penning trap physics

Ions, being charged particles, may be confined with electric and/or magnetic fields - however, from Earnshaw's theorem, doing so with either a static electric or magnetic field is not possible in three dimensions. This results from Gauss's law that (in the absence of charge density) electric fields have no divergence $\boldsymbol{\nabla} \cdot \boldsymbol{E} = 0$. Thus there can be no minimum locally to confine a charge in three dimensions; only saddle points are possible. However, using oscillating electric fields (effectively rapidly flipping a saddle point) one can trap a charged particle: the time-averaged effect of the oscillating field is to produce a 'pseudopotential' that confines the charge. Another approach, and the one that will be the focus of this chapter, is to use a static magnetic field in addition to a static electric field - a Penning trap.

Put another way, confinement in three dimensions would require restoring forces in the $\hat{x}$, $\hat{y}$, and $\hat{z}$ directions and as a result an electric potential

$$\Phi = \Phi_0(\alpha x^2 + \beta y^2 + \gamma z^2), \tag{2.1}$$

where α, β, γ are all positive. However, Laplace's equation requires that $\nabla^2 \Phi = 0$, and so, also that $\alpha + \beta + \gamma = 0$. Thus, the condition that α, β, γ all be positive cannot be met and three

dimensional confinement is not possible in this way. Confinement along the $\hat{z}$-axis is possible by assuming cylindrical symmetry and setting $\gamma = 2$ and $\alpha = \beta = -1$ such that $\Phi = \Phi_0(2z^2 - x^2 - y^2)$, which results in a restoring force along $\hat{z}$ and a deconfining force in the radial plane.

2.1.1   Single ion in a Penning trap

A Penning trap uses a homogeneous magnetic field along one axis $\boldsymbol{B} = B\hat{z}$ as well as a static electric field $\boldsymbol{E} = -\nabla\Phi$. For a pure quadrupole potential

$$\Phi(x, y, z) = \frac{V_0}{R^2}(2z^2 - x^2 - y^2), \tag{2.2}$$

where V_0 is an applied voltage and R parameterizes the trap electrode geometry (higher order corrections may be relevant and will be considered later). In the presence of the magnetic field $\boldsymbol{B}$, a single charge q moving with velocity $\boldsymbol{v}$ will experience a force

$$\boldsymbol{F} = -q\nabla\Phi + q(\boldsymbol{v} \times \boldsymbol{B}). \tag{2.3}$$

Using the definition $\omega_c = qB/m$ for the cyclotron frequency of a charge q with mass m, the equations of motion are:

$$\ddot{z} + w_z^2 z = 0$$
$$\ddot{x} - \omega_c \dot{y} - \frac{1}{2}w_z^2 x = 0$$
$$\ddot{y} + \omega_c \dot{x} - \frac{1}{2}w_z^2 y = 0. \tag{2.4}$$

The solution for motion along the $\hat{z}$-axis is simple harmonic motion with an axial (meaning along the axis of the magnetic field, $\hat{z}$) mode frequency

$$\omega_z = \sqrt{\frac{2V_0 q}{R^2 m}}. \tag{2.5}$$

The solution for radial motion results in two motional modes with frequencies

$$\omega_\pm = \frac{1}{2}(\omega_c \pm \sqrt{\omega_c^2 - 2\omega_z^2}), \tag{2.6}$$

where ω_- is the magnetron frequency and ω_+ is reduced cyclotron frequency (also denoted ω_m and ω_c', respectively, in the literature). For an ion in an ideal Penning trap, then, the motion is a superposition of these three degrees of freedom characterized by the frequencies $\omega_z, \omega_-, \omega_+$. These motional frequencies can be further described through the Brown-Gabrielse invariance theorem [20]:

$$\omega_c^2 = \omega_z^2 + \omega_-^2 + \omega_+^2, \tag{2.7}$$

which holds true even in the case of misalignments and some nonidealities in the trapping potential. Since the solutions of Eq. 2.6 must be real to be physical, this sets the requirement that $\omega_z < \omega_c/\sqrt{2}$ for stable trapping.

One unusual feature of the motion characteristic of an ion in a Penning trap is that the total energy of the magnetron motion is negative. This results from the small kinetic energy (due to its low motional frequency) associated with this motion relative to its potential energy, which is negative. Cooling this mode, then, typically means adding energy to it: removing energy would increase the radius of the magnetron motion (see Sec. 2.3).

2.1.2 Many ions: non-neutral plasma

With many ions confined in a Penning trap, it is appropriate to consider their motion and behavior in the trap collectively as a single component, non-neutral plasma. Key features of a non-neutral (i.e. ionic) plasma at low temperature is that it has a constant, uniform density and aspect ratio determined by the rotation frequency (as well as the trapping parameters). The aspect ratio is defined as the ratio of the axial extent to the diameter of the plasma $\alpha = z_{\text{plas}}/d_{\text{plas}}$. For a plasma at zero temperature, the density is given by

$$n = \frac{2\epsilon_0}{q^2} m \omega_r (\omega_c - \omega_r), \tag{2.8}$$

where ω_r is the rotation frequency of the plasma. The plasma frequency is defined as $\omega_p^2 = 2\omega_r(\omega_c - \omega_r)$. Figure 2.1 illustrates the dependence of the density and aspect ratio on the rotation

frequency. At low rotation frequencies approaching the magnetron frequency ω_m, the plasma is an oblate spheroid and eventually a two-dimensional array (the regime relevant for this thesis). As the rotation frequency is increased, the radial confinement increases. The maximum plasma density occurs at a rotation frequency equal to have the cyclotron frequency $\omega_r = \omega_c/2$, which is a regime known as Brillouin flow. Beyond this rotation frequency, the centrifugal force begins to dominate over the radially confining Lorentz force and the plasma beings to expand. As a result, the density and aspect ratio of the plasma as a function of rotation frequency is symmetric about $\omega_r = \omega_c/2$.

2.1.3   Rotating wall

As was seen in the previous section, the rotation frequency effectively sets the radial confinement for the ions. Thus by controlling the rotation frequency, the aspect ratio of the ion plasma can be set. This can be accomplished by applying an external torque, in practice either from a focused laser aligned off-center from and perpendicular to the trap axis or a rotating electric field - a so called 'rotating wall' [21]. The simplest implementation of such an electric field is an electric dipole or quadrupole field. However, for a single species cloud (i.e. one without impurity ions) a rotating dipole field only couples to the center of mass mode and does not control the rotation frequency. To apply a quadrupole rotating electric field, a segmented electrode with 8 sectors can be used (see Fig. 2.2) with an oscillating voltage $V = V_{\text{wall}} \sin\left(\omega_{\text{drive}} t + \phi\right)$, where ϕ is illustrated in Fig. 2.2 and $\omega_{\text{wall}} = \omega_{\text{drive}}/2$.

2.1.4   Nonidealities

So far, this chapter has assumed a Penning trap with a perfectly harmonic trapping potential. However, in practice there are limits on the experimentally possible (and desirable) trap geometries. To account for this, the trap electrode geometry is modeled and voltages are applied to these electrodes to best approximate a purely harmonic potential.

A convenient way to expresses the simulated potential is with a multipole expansion:
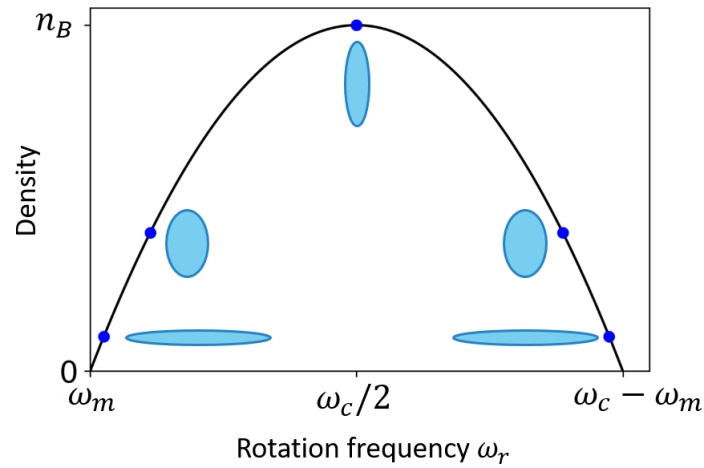
Figure 2.1: Illustration of plasma density and aspect ratio as function of rotation frequency. For a quadratic confining potential like that of Eq. 2.2, the plasma has the shape of a spheroid. At the rotation frequency $\omega_r = \omega_c/2$ the maximum density is achieved. This work focuses on the regime where ω_r approaches the magnetron frequency ω_m.
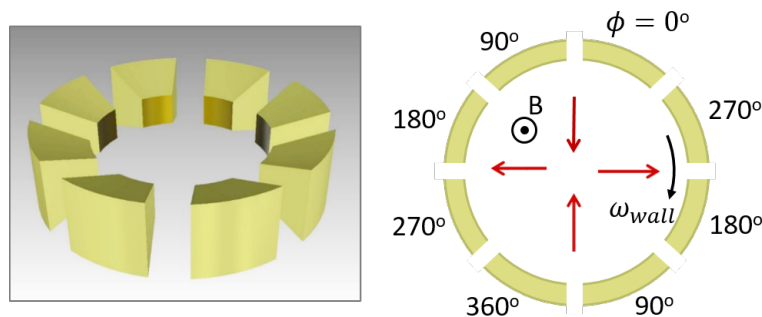
Figure 2.2: On the left, a three dimensional representation of the segmented rotating wall electrodes. On the right, the phases applied to the rotating wall electrodes for a quadrupolar electric field. The magnetic field is directed out of the page, and the ions rotate clockwise. The red arrows illustrate the resulting electric field near the center of the trap, which provides a torque on the ion crystal.

$$\phi_{\text{trap}}(\rho, z) = \sum_{n=0}^{\infty} C_{2n} r^{2n} P_{2n}\left(\frac{z}{r}\right),\tag{2.9}$$

where $P_n(x)$ is a Legendre polynomial, $r = \sqrt{\rho^2 + z^2}$ is the spherical radius, and the coefficients C_{2n} depend on the trap geometry and the voltages applied to the trap electrodes. Odd coefficients C_n vanish under the assumption of a trap potential that is an even function of z. The trap potential can then be expanded for the first few coefficients C_{2n}:

$$\begin{aligned}
\phi_{trap}(\rho, z) = C_0 &+ C_2\left(z^2 - \frac{\rho^2}{2}\right)\\
&+ C_4\left(z^4 - 3\rho^2 z^2 + \frac{3}{8}\rho^4\right)\\
&+ C_6\left(z^6 - \frac{15}{2}\rho^2 z^4 + \frac{45}{8}\rho^4 z^2 - \frac{5}{16}\rho^6\right) + \dots.
\end{aligned}\tag{2.10}$$

For an ideal harmonic trap, coefficients above C_2 vanish. This expression allows for assessing the contributions from these higher order coefficients and calculating voltages to null them. Section 3.2.1 goes into more detail regarding how the values for the C_{2n} coefficients are set for the NIST Penning trap.

2.2 Beryllium electronic structure

Singly ionized beryllium ($^9\text{Be}^+$) is the ion of choice for the experiments described here. Having a single valence electron makes its electronic structure simple and its light mass allows for high trap frequencies. For this work, only the S and P orbitals are considered, as all the relevant states are contained within these manifolds (Fig. 2.3). The transition from S to P has a natural linewidth of 19.4 MHz (lifetime of 8.2 ns) and can be driven by electric dipole radiation at 313 nm (UV).

Figure 2.3 illustrates three relevant energy levels: $1s^2 2s^2 S_{1/2}, 1s^2 2s^2 P_{1/2}$, and $1s^2 2s^2 S_{3/2}$ (using term symbols $^{2S+1}L_J$, where S, L, and J represent the electron spin, orbital angular momentum, and total angular momentum, respectively). The P orbital has fine structure splitting due to the coupling between the spin and orbital angular momentum (the S orbital has no fine structure). The fine structure splitting between the $P_{1/2}$ and $P_{3/2}$ levels at zero magnetic field is

197.2 GHz [22]. Additionally, there is hyperfine structure due to the coupling of the electron's spin to the nuclear spin. As a result of the strong magnetic field, there are also splittings due to the Zeeman interaction of the magnetic field with the spin, orbital, and nuclear magnetic moments. For the ground state, the Hamiltonian is

$$H = hA\mathbf{I} \cdot \mathbf{J} - \mu_{\mathbf{I}} \cdot \mathbf{B} - \mu_{\mathbf{J}} \cdot \mathbf{B}, \tag{2.11}$$

where $\mathbf{J}$ is the total electronic angular momentum, $\mathbf{I}$ is the nuclear spin, $\mathbf{B}$ is a static magnetic field, h is the Planck constant, A is the magnetic dipole hyperfine constant, and $\mu_{\mathbf{I}}$ and $\mu_{\mathbf{J}}$ are the nuclear and electronic magnetic moment operators, respectively. In Eq. 2.11, the first term is the magnetic dipole hyperfine interaction, the second is the nuclear Zeeman interaction, and the third is the electronic Zeeman interaction. Furthermore, the relevant g-factors are defined as $g_J = -\mu_J/(J\mu_B)$ and $g_I' = -\mu_I/(I\mu_B)$, where μ_B is the Bohr magneton. To calculate the energies of the sublevels of the groundstate (which has $J = 1/2$), the Breit-Rabi formula may be used [23]. The energies of the (F, m_F) sublevels with $J = 1/2$ and $I \geq 1/2$ are given by

$$E(F, m_F) = hA\left(-\frac{1}{4} + \frac{g_I' m_F \mu_B B}{hA} \pm \frac{2I+1}{4}\sqrt{1 + \frac{4m_F}{2I+1}X + X^2}\right), \tag{2.12}$$

where $X = \mu_B B(g_J - g_I')/[(I + 1/2)hA]$ [24].

Through optical pumping, the nuclear spin is frozen out such that $m_I = +3/2$, which allows for simplifying the level structure as shown in Fig. 2.3. We define the qubit states as two levels in the $S_{1/2}$ manifold: $|F = 2, m_I = +3/2, m_J = +1/2\rangle \equiv |\uparrow\rangle$ and $|F = 2, m_I = +3/2, m_J = -1/2\rangle \equiv |\downarrow\rangle$. The qubit is, essentially, the $^9\text{Be}^+$ valence electron spin in the ground state. For a magnetic field of $B = 4.46$ T, the splitting between the qubit states $|\uparrow\rangle$ and $|\downarrow\rangle$ is approximately 124 GHz. At this magnetic field, the qubit states diverge linearly at 28 MHz/mT [25] and thus the transition is sensitive to magnetic field fluctuations. Doppler cooling (see subsequent section) and state-selective readout is performed on the cycling transition $|\uparrow\rangle \rightarrow {}^2P_{3/2}(m_J = +3/2)$. State initialization is performed with optical pumping into the $|\uparrow\rangle$ state with the Doppler cooling and repump lasers (see

Fig. 2.3). Optical pumping the nuclear spin into $m_I = 3/2$ occurs as a result of driving transitions to $^2P_{3/2}$ and there being a small admixture of (m_I, m_J) states in the $^2P_{3/2}$ manifold [24, 26].

2.3   Doppler cooling

Doppler cooling is a technique used to reduce the kinetic energy of atoms via velocity dependent momentum transfer. A laser red-detuned from a cycling transition will be Doppler shifted into resonance for an atom moving towards the photons, and thus will scatter photons. The lower limit to the temperature achievable depends on the linewidth of the transition: $T_{\text{Doppler}} = \hbar\gamma/(2k_B)$, where γ is the linewidth of the transition.

In a Penning trap, it is straightforward to apply this type of cooling to the axial drumhead modes. A red-detuned laser directed along the trap axis will cool axial motion (Fig. 2.4). The radial motion, however, is less straightforward to cool. In particular, the magnetron motion has negative total energy and the minimum energy occurs for a diverging radius of motion. A uniform, red-detuned laser in the radial plane would increase the amplitude of magnetron motion, an unstable and undesirable outcome. Thus, to cool the magnetron motion energy must be supplied to it. A focused laser beam offset from the center of the ion crystal is used to cool the cyclotron motion (via Doppler cooling) and to reduce the amplitude of magnetron motion (Fig. 2.5). The beam is offset from center such that it co-propagates with the rotation of the ion crystal and provides a torque that reduces the radius of the crystal. The interplay of the focused perpendicular cooling beam and the rotating wall can lead to the removal of energy from the radial modes [27], but the ultimate temperature that is reached in practice remains under study [28].

2.4   The optical-dipole spin-dependent force

A key component of nearly all experiments performed with the Penning trap apparatus is a spin-dependent force generated by way of an optical dipole force (ODF). This section will describe in detail how this optical dipole force is produced and how it gives rise to a spin-dependent coupling with the motion of the ion crystal.
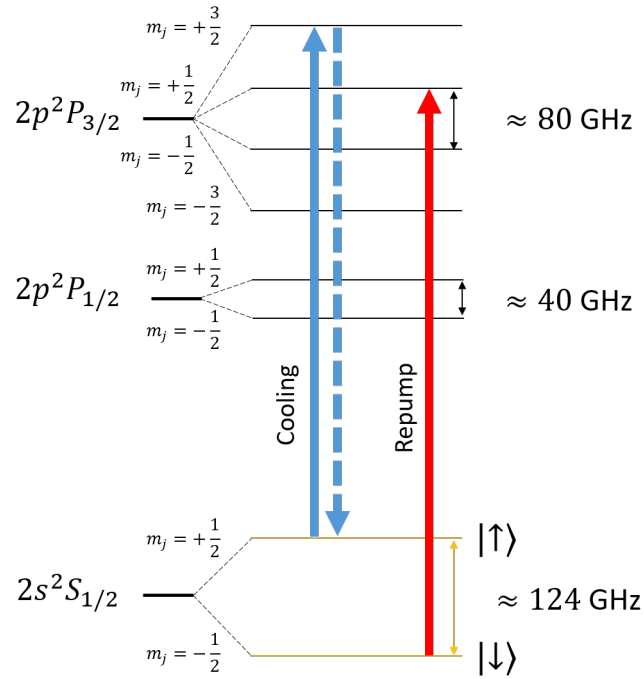
Figure 2.3: Level structure of $^9\text{Be}^+$ at 4.5 T. Only the $m_I = 3/2$ sublevels are shown, as after optical pumping the nuclear spin remains in this state. The qubit states are colored yellow and labeled with $|\uparrow\rangle$ and $|\downarrow\rangle$. Doppler cooling and state-selective readout is performed on the cycling transition $|\uparrow\rangle \rightarrow {}^2P_{3/2}(m_J = +3/2)$ with repumping out of the $|\downarrow\rangle$ state back into the $^2P_{3/2}$ manifold.
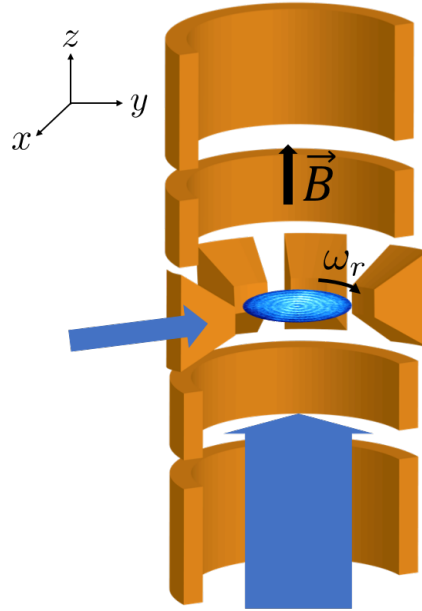
Figure 2.4: Cross-sectional illustration of Penning trap and Doppler cooling beams. The trap electrodes are depicted by the orange surfaces (again, on the cross-section) and the magnetic field is along the $\hat{z}$-axis. Doppler cooling beams are directed along the trap/magnetic field axis (the 'parallel' Doppler cooling beam) and also perpendicular to this axis (the 'perpendicular' beam). The parallel beam has a waist large enough to uniformly illuminate an ion crystal of several hundred ions ($\sim$1 mm) and the perpendicular beam is tightly focused and offset from the center of the crystal.
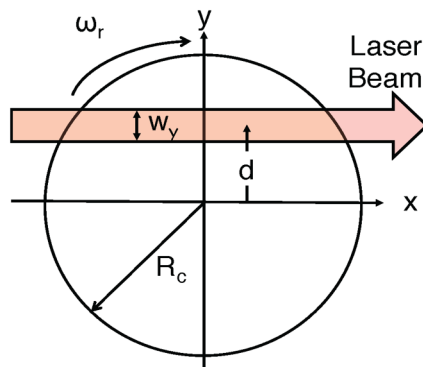
Figure 2.5: Schematic of the perpendicular cooling beam interacting with a rigidly rotating ion crystal [27]. The perpendicular cooling beam has a waist w_y and is offset from the center of the crystal (defined by the $\hat{x}$-axis in this graphic) by an amount d. The crystal has a radius R_c and is rotating at a frequency ω_r.
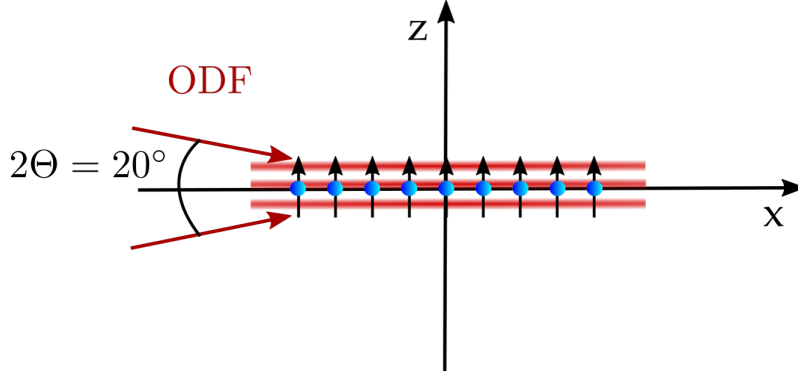
Figure 2.6: Two beams are directed onto the ions at $\pm 10°$ and with a difference frequency μ, resulting in a 1D traveling wave optical potential with δk along $\hat{z}$. The spatial gradient gives rise to an optical dipole force.

2.4.1   Optical-dipole spin-dependent force

To generate the ODF, off-resonant laser light is used to produce AC stark shifts (ACSS) on the spin states $|\uparrow\rangle$ and $|\downarrow\rangle$, previously described as the $2s^2 S_{1/2}(m_j = +1/2)$ and $2s^2 S_{1/2}(m_j = -1/2)$ states, respectively. Two beams are directed onto the ion crystal at angles of $\pm 10°$, as illustrated in Fig. 2.6. These two lasers couple the spin states to excited states in the $2p^2 P_{3/2}$ manifold, as shown in Fig. 2.7. Considering only the nearest transitions, the $|\uparrow\rangle$ state is coupled to the $2p^2 P_{3/2}(m_j = +1/2)$ state with a detuning of approximately 20 GHz and the $|\downarrow\rangle$ state is coupled to the $2p^2 P_{3/2}(m_j = -1/2)$ state with a detuning of approximately -20 GHz. The resulting optical dipole force thus has opposite sign for the two spin states, and the magnitude of these forces may be tuned to be equal. With this, then, there is a spin-dependent force applied to the ions. Note that each laser individually couples these pairs of states off-resonantly, resulting in an ACSS from each beam on both of the spin states. However, as will be shown in the subsequent section, the net ACSS on the qubit from each beam can be nulled. In general, there will be some frequency difference μ between the two beams, but this is a small difference on the order of 1 MHz.

The two lasers will interfere and produce a spatially dependent optical potential. Additionally, the difference frequency μ may be set and controlled. If the difference vector of the two lasers δk is along the $\hat{z}$-axis, then the optical potential is modulated by the term $\sin(\delta k \hat{z} + \mu t)$. The result
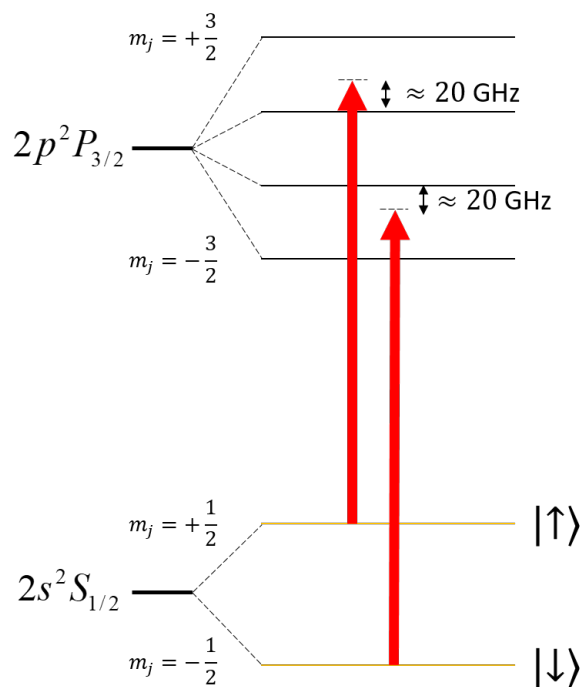
Figure 2.7: Relevant energy levels in Be$^+$ for the ODF. The two beams off-resonantly couple the two spin states to the excited state manifold. The positive (negative) detuning of roughly 20 GHz for the $|\uparrow\rangle$ ($|\downarrow\rangle$) state relative to the nearest excited state level results in a force on each of the spin states with opposite sign.

for a single ion is a Hamiltonian of the form:

$$\hat{H}_{\text{ODF}} = U\sin(\delta k\hat{z} + \mu t)\hat{\sigma}^z, \tag{2.13}$$

where U is the zero-to-peak amplitude of the optical potential and σ^z is the Pauli spin matrix. Assuming the axial spatial extent of the ions is small compared to $2\pi/\delta\text{k}$, this expression may be rewritten as

$$\hat{H}_{\text{ODF}} = F_0\cos(\mu t)\sum_i \hat{z}_i\hat{\sigma}_i^z \tag{2.14}$$

for the case of i ions. Here $F_0 = U\delta k DWF$, where $DWF = \exp(-\delta\text{k}^2\left\langle\hat{z}_i^2\right\rangle/2)$ is the Debye-Waller factor which characterizes the departure from the Lamb-Dicke confinement regime $(\delta\text{k}\sqrt{\langle\hat{z}_i^2\rangle} \ll 1)$ [29]. In the interaction picture, the axial position operator for the ith ion $\hat{z}_i$ can be written in terms of the axial normal modes of the planar array:

$$\hat{z}_i = \sum_{m=1}^{N} b_{jm}\sqrt{\frac{\hbar}{2Mw_m}}\left(\hat{a}_m e^{-iw_m t} + \hat{a}_m^{\dagger}e^{iw_m t}\right) \tag{2.15}$$

where $\vec{b}_m$ and w_m are the eigenvectors and eigenfrequencies of the m modes, respectively.

2.4.2   Polarization and frequency details

Up to this point, the Hamiltonian described took into account only the ACSS from the interference of the two laser beams - individually each beam may also introduce an ACSS. However, with the appropriate choice of polarization given a particular detuning from the excited states the ACSS of each beam on the two spin states can be made equal, and hence the total ACSS on the qubit cancelled. The result is that the qubit decoherence due to laser intensity fluctuations is minimized. Additionally, the force on $|\uparrow\rangle$ can be set equal in magnitude and opposite in sign to the force on $|\downarrow\rangle$ $(F_\uparrow = -F_\downarrow)$.

To null the ACSS from a single beam on the qubit, the ODF laser beams are linearly polarized at an angle ϕ_p with respect to the $\hat{z}$-axis (see Fig. 2.8). The electric fields of the upper and lower ODF beams are
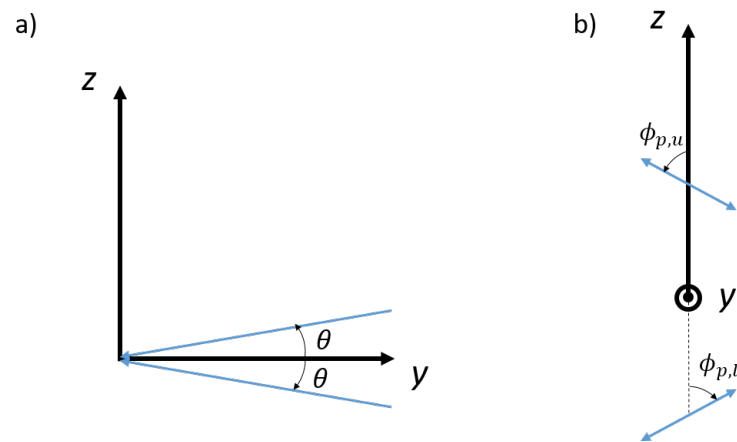
Figure 2.8: Sketch of ODF laser angles and polarizations. a) The ODF laser beams lie in the y-z plane and intersect at an angle of $\pm\theta = 10°$ with respect to the $\hat{y}$-axis. b) View looking in the $-\hat{y}$ direction. Both beams are linearly polarized with different angles of polarization relative to vertical ($\hat{z}$-axis).

$$\vec{E}_U(\vec{r}, t) = \hat{\epsilon}_U E_U \cos(\vec{k}_U \cdot \vec{r} - \omega_U t)$$

$$\vec{E}_L(\vec{r}, t) = \hat{\epsilon}_L E_L \cos(\vec{k}_L \cdot \vec{r} - \omega_L t). \tag{2.16}$$

The ACSS of the qubit states for a single beam, then, are

$$\Delta_{\uparrow,acss} = A_\uparrow \cos^2(\phi_p) + B_\uparrow \sin^2(\phi_p)$$

$$\Delta_{\downarrow,acss} = A_\downarrow \cos^2(\phi_p) + B_\downarrow \sin^2(\phi_p) \tag{2.17}$$

where $A_\uparrow (A_\downarrow)$ is the AC Stark shift of the $|\uparrow\rangle$ $(|\downarrow\rangle)$ state for a π-polarized beam (i.e. $\hat{\epsilon}$ parallel to $\hat{z}$) and $B_\uparrow (B_\downarrow)$ is the AC Stark shift of the $|\uparrow\rangle$ $(|\downarrow\rangle)$ state for a σ-polarized beam (i.e. $\hat{\epsilon}$ perpendicular to $\hat{z}$). The ACSS of the qubit transition is

$$\Delta_{acss} = (A_\uparrow - A_\downarrow) \cos^2(\phi_p) + (B_\uparrow - B_\downarrow) \sin^2(\phi_p). \tag{2.18}$$

If $A_\uparrow - A_\downarrow$ and $B_\uparrow - B_\downarrow$ have opposite signs, then there is an angle such that $\Delta_{acss} = 0$. Thus, each beam has no net ACSS on the qubit transition. For a detuning of $\Delta = -59$ GHz from the cycling transition $(|\uparrow\rangle \to 2p^2 P_{3/2}(m_j = +3/2))$, this occurs at $\phi_p \approx \pm 65°$ (see Sec. 4.3 for experimental calibration). Recall that the difference frequency μ is small compared to the detuning Δ.

We can choose different polarizations of the two beams to get a spatially dependent ACSS through a polarization gradient along the $\hat{z}$-axis, which results in a spin-dependent force along this axis. Specifically, we cross the polarizations of the two beams with $\phi_{p,u} = 65°$ and $\phi_{p,l} = -65°$. The resulting interference gives the previously mentioned axially dependent ACSS, which is the same as previously but with a factor of 2 and a sinusoidal term:

$$\Delta_{\uparrow,acss} = 2(A_\uparrow \cos^2(\phi_p) - B_\uparrow \sin^2(\phi_p)) \cos(\delta k \cdot z - \mu t)$$

$$\Delta_{\downarrow,acss} = 2(A_\downarrow \cos^2(\phi_p) - B_\downarrow \sin^2(\phi_p)) \cos(\delta k \cdot z - \mu t), \tag{2.19}$$

where $\delta k \equiv |\vec{k}_U - \vec{k}_L| = 2k\sin(\theta)$ is the wavevector difference, $\mu = \omega_U - \omega_L$ is the frequency difference (ODF beatnote), and $\phi = |\phi_{p,u}| = |\phi_{p,l}|$. The spin-dependent force resulting from this spatially dependent ACSS is $F_{\uparrow,\downarrow}(z,t) = F_{\uparrow,\downarrow}\sin(\delta k \cdot z - \mu t)$ where

$$F_{\uparrow} = 2\hbar\delta k(A_{\uparrow}\cos^2(\phi_p) - B_{\uparrow}\sin^2(\phi_p))$$

$$F_{\downarrow} = 2\hbar\delta k(A_{\downarrow}\cos^2(\phi_p) - B_{\downarrow}\sin^2(\phi_p)). \tag{2.20}$$

With the appropriate choice of detuning Δ, the ACSS $A_{\uparrow,\downarrow}$ and $B_{\uparrow,\downarrow}$ combine in such a way that $F_{\uparrow} = -F_{\downarrow} \equiv F_0$. This detuning can be found experimentally, and the procedure is described in Sec. 4.3. Note that the above derivations have assumed that $\delta\vec{k}$ is along the $\hat{z}$-axis such that the wavefronts of the 1D optical lattice are aligned perpendicular to the $\hat{z}$-axis. We estimate the misalignment error $|\theta_{err}| \leq 0.01°$. Further discussion of the alignment of the ODF wavefronts and the estimation of the error is provided in Sec. 4.1.

Chapter 3

The NIST Penning trap apparatus

This chapter will provide an overview and some details of the NIST Penning trap apparatus. Joe Britton, Brian Sawyer, Justin Bohnet, and John Bollinger designed and built the apparatus.

3.1 Mechanical and trap assembly

The NIST Penning trap consists of two sets of stacked cylindrical electrodes separated by Macor insulating rings. The two sets of electrodes are used as a loading trap and an experiment trap. Both are comprised of a set of 5 electrodes: two endcap electrodes (which are typically grounded), a central electrode (which is segmented into 8 sectors for the experiment trap), and two middle electrodes on either side of the central electrode. The trap is enshrouded in a fused silica vacuum envelope which is connected to the UHV vacuum system. The trap and vacuum envelope are inserted into the bore of a 4.5 T superconducting magnet in a vertical orientation. The magnet rests on a floatable optical table with the vacuum system mounted to the top of the magnet. A gimbal mount is used to allow for aligning the trap to the magnetic field axis. Laser and imaging optical access both parallel and perpendicular to the trap axis is provided by mirrors fixed to a platform attached to the underside of the magnet and a mount inserted up into the bore (see Fig. 3.1).
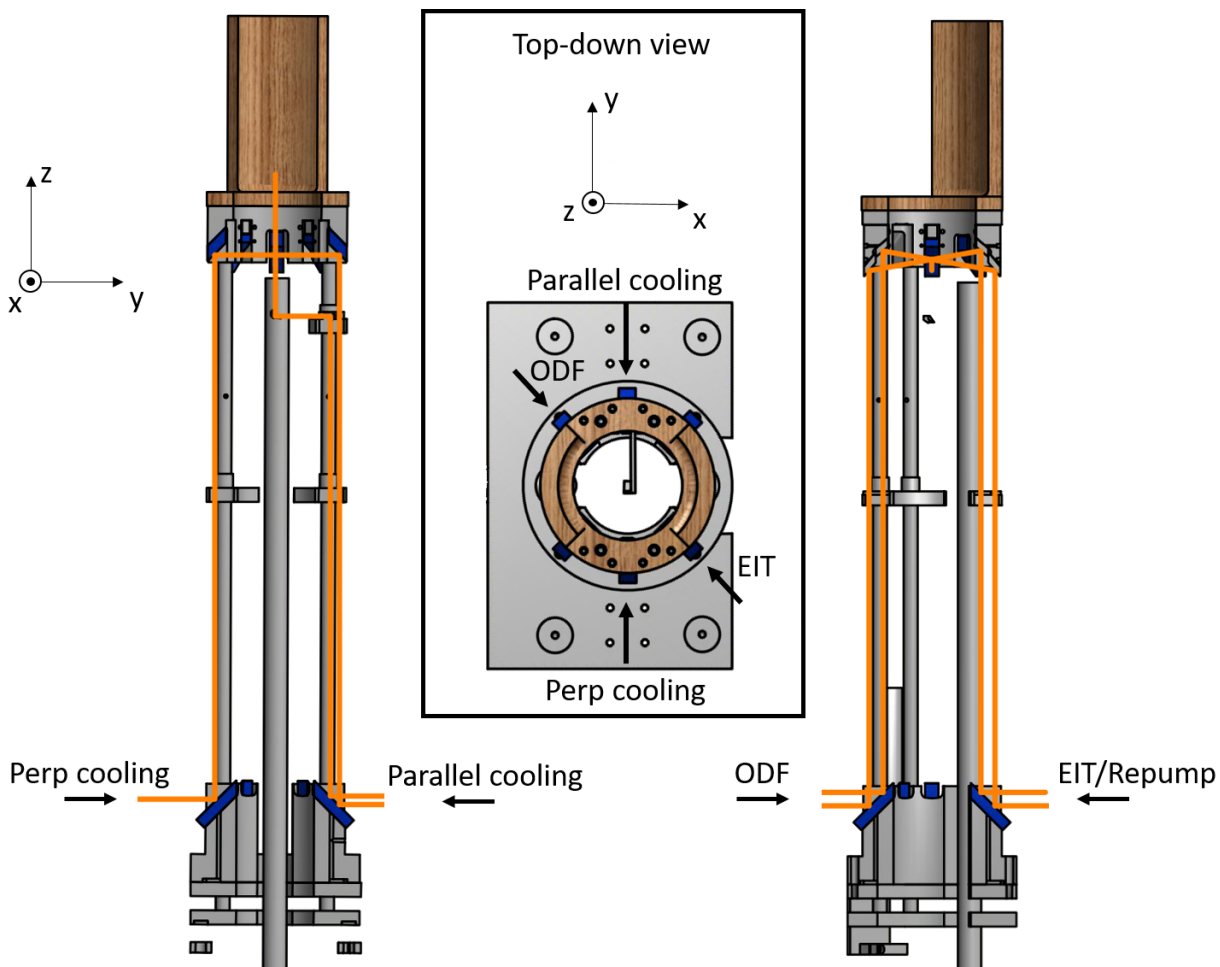
Figure 3.1: Illustration of the laser beam paths to the ions up through the bore of the magnet. Left: view from the side of the perpendicular and parallel beam paths. The perpendicular beam passes through the trap and emerges on the opposite side of the magnet. The parallel beam is reflected up along the axis of the trap and exits through a port on the top of the assembly. Right: Beam paths for the pairs of ODF and EIT beams, where one of the EIT beams doubles as a repumper. These beams are reflected off of static mirrors in the bore which set them at $\pm 10°$ with respect to the plane of the ions. The two pairs of beams are counter-propagating. Middle: top-down view of the beam paths.

L5   L4   L3   L2   L1   T4   T3   W1-8   T2   T1   Mesh
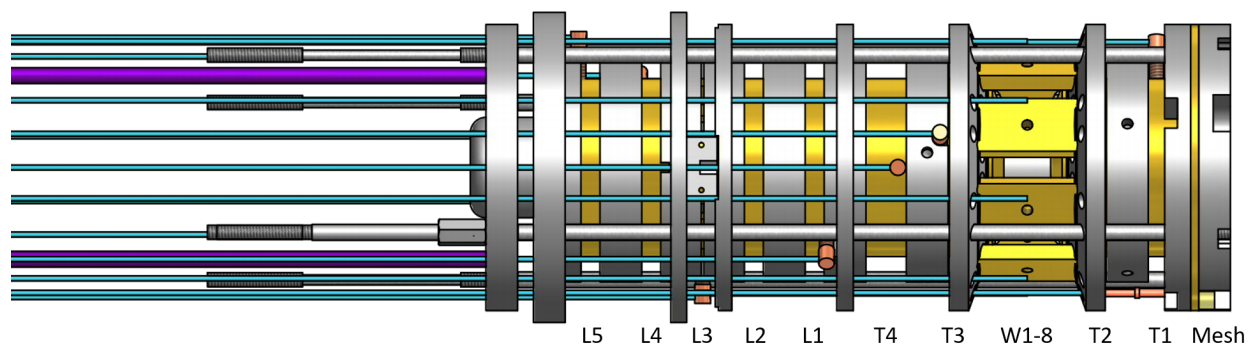
Figure 3.2: Schematic of trap electrodes. Two Penning traps were constructed next to each other. One trap is used for loading ions (delineated by the 'L' names, L1-5) and the other is the experiment trap consisting of T1-4 plus a segmented electrode for the rotating wall (W1-W8).
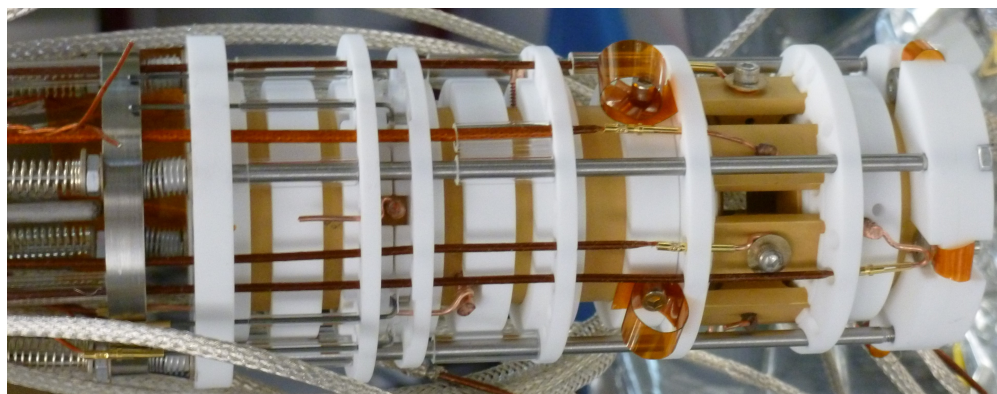
Figure 3.3: Photograph of trap prior to insertion into fused silica vacuum envelope.

Figure 3.4: Photograph of trap inside fused silica vacuum envelope. The view is that of the ODF beam path through the trap.

3.1.1   Magnet

To produce the strong axial magnetic field for radial confinement of the ions, we use a room-temperature bore superconducting magnet. The magnet is a Nalorac Cyrogenics Corporation model 4.5/125 manufactured in 1990 (happy 30th, magnet [1]). The bore is 12.7 cm in diameter and the Niobium Titanium superconducting solenoid produces a 4.5 T magnetic field with a current of $\sim$58 A. The superconducting main and shim coils are submerged in liquid helium contained within an insulated dewar. An outer sheath of liquid nitrogen provides additional thermal shielding. The liquid helium boil off rate is (an impressively low) $\sim$20 mL/h.

3.2   Loading and trapping

This section will give an overview of the typical loading, transport, and trapping parameters for the NIST Penning trap. We load into the loading trap with a shallow trapping potential, then deepen the trapping potential and transport the ions to the experiment trap. To load and collect ions, the beryllium oven is turned on for a few seconds followed by the photoionization laser. Both are left on for several seconds, producing beryllium ions near the center load trap. To collect ions, the central electrode of the load trap (L_3, see Fig. 3.2) is set to -5 V with all other electrodes grounded. Once ions have been collected, they are transported to the experiment trap. The voltage on the central load trap electrode is increased to -100 V, and subsequently the next electrode (L_2) is set at -100 V before L3 is grounded. This continues until the ions reach the segmented rotating wall electrodes ($W_1 - W_8$). At this point the rotating wall electrode voltage is increased to -610 V, and the adjacent electrodes T_2 and T_3 have their voltages set to -534 V. The trap frequency for this potential is $w_z/(2\pi) = 888.2$ kHz (see the following section, 3.2.1). The transport process takes about 1 minute, with 5 seconds between each step of the trap voltages. At this point the Doppler cooling is turned on, and the ions may be 'spun-up' into a cold crystal (see Sec. 4.7).

---

[1] Yes, the magnet is older than I am. Barely. Don't ask about the age of the dye lasers.

3.2.1 Trap potentials and characteristics

As was described in Sec. 2.1.4, the choice of trap geometry plus voltages applied to the electrodes sets the potential at the ions. Through simulations of the trap potential, we determine the electrode voltages that will yield the most desirable trapping potential. In general, a high trap frequency (for better Lamb-Dicke confinement) and minimized higher-order anharmonic contributions is best, though it has been shown theoretically that a somewhat anharmonic potential can lead to more uniform two-dimensional crystals [30].

Modeling of the NIST Penning trap electrodes (performed by Carson Teale) yielded the following matrix of coefficients parameterizing the trap geometry:

	Endcap electrodes (T_1, T_4)	Middle electrodes (T_2, T_3)	Center electrode $(W_1 - W_8)$
C_0	0.0756	0.5157	0.487
C_2	0.19197 cm^{-2}	0.37467 cm^{-2}	-0.56663 cm^{-2}
C_4	0.06738 cm^{-4}	-0.53148 cm^{-4}	0.46410 cm^{-4}
C_6	-0.00983 cm^{-6}	0.29917 cm^{-6}	-0.28934 cm^{-6}

Table 3.1: Table of trap voltage multipole coefficients. The displayed values are multiplied by a vector corresponding to the trap voltages applied to these electrodes ($V_{\mathrm{trap}} = V_{\mathrm{end}}, V_{\mathrm{mid}}, V_{\mathrm{cen}}$) to yield the coefficients C_n for some n.

Using this table of values, it is possible to calculate the expected potential the ions will see in the trap. For a particular set of voltages, the trap frequency (COM mode frequency) ω_z can be estimated: $\omega_z = \sqrt{2qC_2/m_{Be}}$, where C_2 is calculated from Table 3.1. Typically, $V_{\mathrm{trap}} = (V_{\mathrm{end}}, V_{\mathrm{mid}}, V_{\mathrm{cen}}) = (0, -1.715 \text{ kV}, -1.974 \text{ kV})$, where $V_{\mathrm{end}}, V_{\mathrm{mid}}$, and V_{cen} are the voltages applied to the endcap electrodes, the middle electrodes, and the central segmented (rotating wall) electrodes, respectively. With these voltages, $\omega_z/(2\pi) = 1.60$ MHz, which is very close to the empirically measured value $\omega_z/(2\pi) = 1.595$ MHz. These voltages were chosen to empirically minimize anharmonicities in the trapping potential (i.e. the C_4 term in the potential). Based on the simulated trap potential, this value of V_{trap} would result in an anharmonic contribution of $r_w^4 C_4 = -4.6$ V, where $r_w = 1$ cm is the electrode radius. This is a small quantity compared to the harmonic potential coefficient $r_w^2 C_2 = 476$ V.

3.2.2 Photoionization

Neutral beryllium can be ionized in the NIST Penning trap by way of electron impact ionization or photoionization via a two-photon process with continuous 235 nm laser light. Photoionization offers several advantages, including element and isotope selectivity as well as increased efficiency relative to electron impact. An additional advantage in the NIST Penning trap is that it allows for loading ions centrally in the trap, since the photoionization beam can be aligned along the trap axis and its waist controlled.

There are two steps involved in the photoionization process, as illustrated in Fig. 3.5. First, 235 nm photons resonantly drive the transition $^1S_0 \to {}^1P_1$ and subsequently the valence electron is excited from $^1P_1$ to the continuum, a transition that requires less energy and thus can be driven by a second photon resonant with the initial transition. At zero magnetic field, the $^1S_0 \to {}^1P_1$ transition wavelength is well-known to be 234.9329 nm, and the wavelength to reach continuum is 306.5 nm [31]. However, at high magnetic field the $^1P_1$ state is split into 3 components: $m_L = 0$, which is not shifted, and $m_L = \pm 1$, which are shifted by ± 62.28 GHz at 4.5 T. Since the photoionization beam is aligned along the trap axis and thus parallel to the magnetic field, the $\Delta m = 0$ transition cannot be driven (as this would require π polarization parallel to the magnetic field). Taking into account this $\sim$62 GHz shift, either of the $m_L = \pm 1$ transitions may instead be driven.

3.3 Lasers

Four lasers are used to produce the $\sim$313 nm light used for Doppler cooling, the ODF, repumping, and EIT cooling beams. All four lasers continuously output light at 626 nm, which is subsequently frequency doubled by cavity-enhanced second-harmonic generation (SHG) [32]. A pair of Toptica TA-SHG PRO systems produce 626 nm light used for EIT cooling, and one of which doubles as the repumper. These are both grating-stabilized external-cavity diode lasers (ECDL) which are amplified in a tapered semiconductor chip and frequency doubled in a resonant SHG stage. Their specified output power is $\sim$500 mW with a linewidth better than 200 kHz. A second
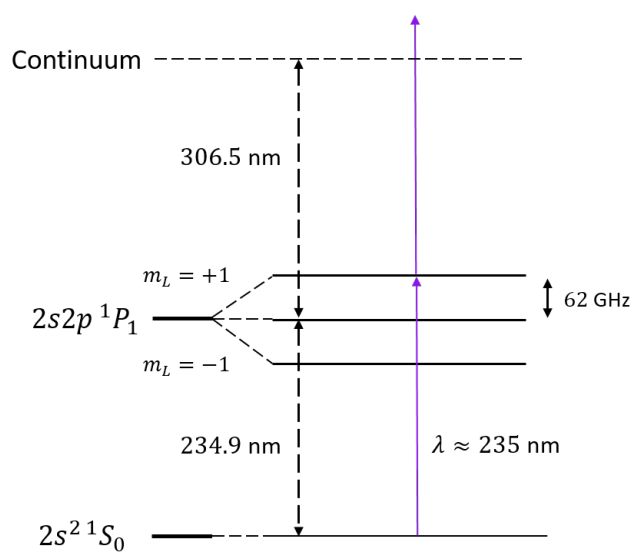
Figure 3.5: Level structure relevant for beryllium photoionization. The first step of the process is a resonant excitation from $^1S_0 \to {}^1P_1$. From there, a second photon excites the electron to the continuum, ionizing the atom.

pair of lasers are used for the Doppler cooling and ODF. These are both Coherent dye lasers [2] which output 626 nm light and are pumped by Coherent Verdi V series diode-pumped solid-state (DPSS) lasers at 532 nm. The 626 nm output power is dependent on the pump power, but typically ranges from $\sim 400 - 800$ mW. The Doppler cooling laser and one of the EIT cooling lasers are both frequency stabilized to separate Iodine saturation spectroscopy setups. The ODF and repump lasers are not frequency stabilized, though when the repump laser is being used for EIT cooling it is phase locked to the other Toptica EIT cooling laser (see Sec. 5.3).

The 626 nm light is sent via optical fiber from the laser table to the experiment table. From there, the light is frequency doubled after which each beam is sent through a double-pass AOM arrangement that allows for rapid on/off switching as well as frequency and phase control. The AOM retroreflection involves a three mirror configuration to mitigate beam steering from thermal refraction effects in the AOM [33]. The ODF, parallel Doppler cooling, and EIT cooling beams are ~ 1 mm in diameter and roughly symmetric, i.e. circular. The diameters are large compared to the size of the crystal, ensuring uniform illumination of the ions. The perpendicular cooling beam is tightly focused with a diameter of < 50 μm at the ions. Typical powers are: ~ 15 mW for the ODF, 150 μW for the parallel cooling, and < 10 μW for the perpendicular cooling. The EIT cooling beam powers are set according to the necessary detuning (see Ch. 5).

3.4   Imaging

Imaging of the ions is performed either along the axis of the trap ('bottom-view') or perpendicular to the trap axis ('side-view'). The bottom-view imaging uses an f/2 objective while the side-view uses an f/5 objective. In either imaging orientation, photons can be collected either on a spatially resolving electron multiplying charge-coupled device (EMCCD) camera (Andor iXon) or a photomultiplier tube (PMT). Additionally, the on-axis bottom-view imaging can be performed with a detector offering precise spatial and temporal resolution: a micro-channel plate (MCP) stack with a photocathode and resistive anode. This MCP-based imaging PMT allows for tagging each

---

[2] See footnote 1
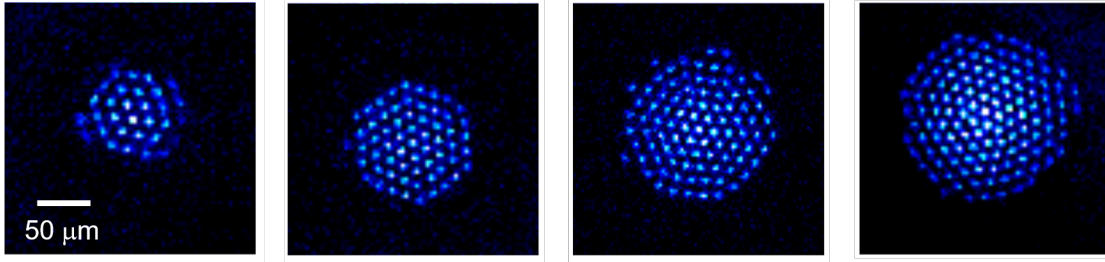
Figure 3.6: Ion crystals of various sizes imaged with single-ion resolution. The view is along the trap axis.

collected photon with (x, y, t) coordinates, enabling a transformation into the rotating frame and the formation of ion crystal images with single ion resolution (as in Figs. 3.6 and 3.7). For the work documented in this thesis, all readout of the ion spin states was performed with global fluorescence imaged onto the side-view PMT.

3.5   Microwaves

For global rotations of the spins, we use a resonant 124 GHz microwave source. The relevant calibrations are described in Sec. 4.4. This section will summarize the microwave and RF components used to produce the 124 GHz. Figure 3.8 provides an overview.

A low noise quartz oscillator at 100 MHz provides the reference signal which ultimately is multiplied up to 124 GHz. This oscillator which serves as the phase reference is an LNFR-100, produced by Spectra Dynamics. The LNFR-100 consists of two phase-locked quartz oscillators, one at 5 MHz and the other at 100 MHz. For frequency offsets greater than 100 Hz, the phase noise is determined by the 100 MHz crystal oscillator. By default, the phase noise for offsets below 2 Hz are set by the external reference (5 MHz maser) though this frequency offset has been reduced to 0.25 Hz for the device used here. Between 100 Hz and 0.25 Hz, the 100 MHz output is disciplined by the 5 MHz oscillator. Phase locked to the 100 MHz oscillator is a Lucix Inc. 15.2 GHz dielectric resonator oscillator (DRO). An FPGA controlled DDS phase locked to the 5 MHz maser outputs $\sim$300 MHz which is mixed with the 15.2 GHz source. This allows for agile control of the phase and frequency of the 124 GHz microwave source. A Polyphase Microwave single-sideband modulator (SSB140180A)
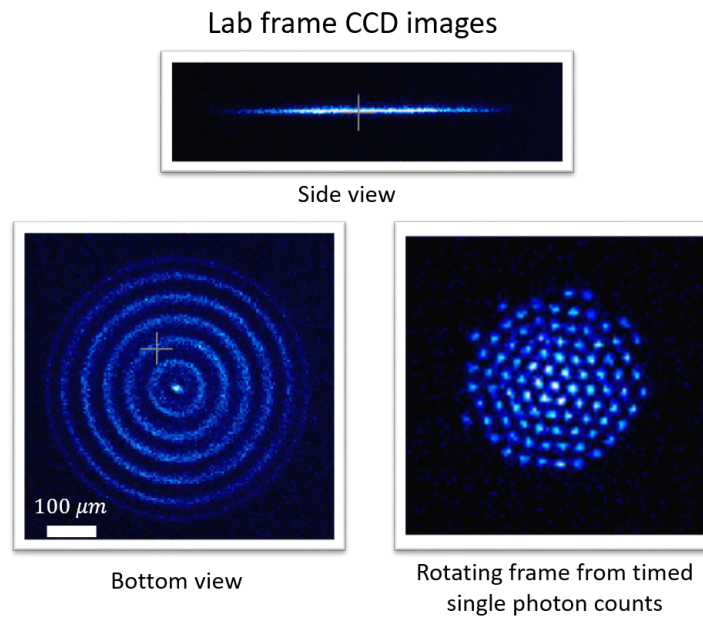
Figure 3.7: Comparison of side-view and bottom-view (on-axis) imaging in the lab frame and also in the rotating frame. Top: a view from the side of a 2D array of ions imaged on a CCD camera. Bottom left: on-axis image of 2D ion crystal in the lab frame, again imaged on a CCD camera. Rings appear because the crystal is rotating. Bottom right: on-axis image of a 2D ion crystal in the rotating frame. Here each photon has been tagged with (x, y, t) coordinates and, because the rotation frequency is known, a transformation into the rotating frame is possible.

serves as the mixer and outputs ∼15.5 GHz. For rapid switching, a TTL-controlled absorptive switch (HMC-C011 from Hitite) is used. Before the final amplification and multiplication stage, the signal is sent through an Anatech 15.5 GHz bandpass filter. Finally, an amplifier-multiplier chain (AMC) from Virginia Diode Inc. multiplies and amplifies up to ∼200 mW at 124 GHz (x8). The output is routed to the ions by way of a WR8 waveguide left open-ended.
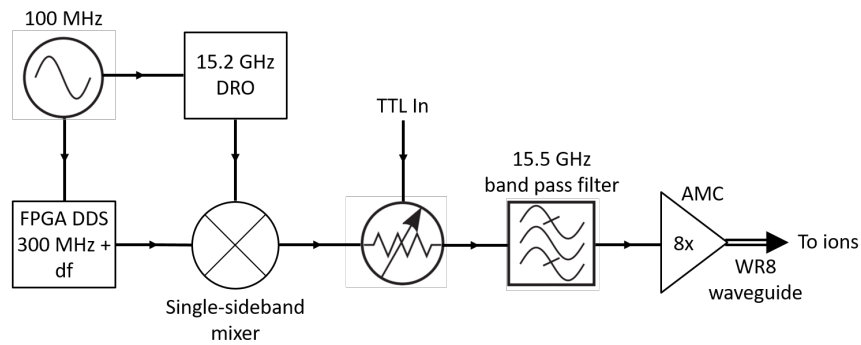
Figure 3.8: Schematic of microwave chain used to produce 124 GHz. 100 MHz reference signal is produced by a Spectra Dynamics Inc. LNFR-100 low noise quartz oscillator. A Lucix Inc. 15.2 GHz DRO is phase locked to the 100 MHz oscillator, as is the ∼300 MHz output of an FPGA controlled DDS used for fine phase and frequency control. These two signals are mixed together with a single-sideband mixer from Polyphase Microwave. A TTL-controlled absorptive switch (Hitite) allows for rapid switching. The ∼15.5 GHz signal is sent through a 100 MHz band pass filter centered at 15.5 GHz from Anatech Inc. Finally, the 15.5 GHz is sent to an amplifier-multiplier chain (AMC) from Virginia Diode Inc. which outputs 124 GHz. This is sent via WR8 waveguide to the ions, which is left open-ended (i.e. no horn is used).

Chapter 4

Alignment and calibrations

This chapter is concerned with experimental alignment and calibration techniques. For the experimental work discussed in this thesis, certain parameters must be measured and controlled. So, in what follows the processes for performing these measurements and calibrations will be delineated.

4.1   ODF alignment and rotating wall harmonics

The ODF Hamiltonian was discussed in detail in Sec. 2.4.1. In that section, the wavevector $\delta\vec{k}$ of the 1D optical lattice produced by the two interfering laser beams was assumed to be parallel to the $\hat{z}$-axis. If the wavefronts of the lattice are not normal to the $\hat{z}$-axis (see Fig 4.1), then the ODF for a particular ion in the crystal will depend on the (x, y) position of that ion, complicating the interaction generated. In this section, the procedure for aligning the ODF wavevector $\delta\vec{k}$ and estimating the misalignment error will be described. With the technique described here, we estimate the misalignment error can be $|\theta_{err}| \leq 0.01°$.

To minimize θ_{err} and sensitively align $\delta\vec{k}$, we minimize the decoherence of the spins with $\hat{H}_{\text{ODF}}$ applied and the difference frequency μ tuned to a harmonic of the rotation frequency of the ion crystal such that $\mu = n\omega_r$. Comparing the decoherence from pairs of harmonics allows for extracting an estimate of the misalignment error θ_{err}.

The sequence used is shown in Fig. 4.2. This is a Ramsey sequence with interaction time τ during which $\hat{H}_{\text{ODF}}$ is turned on with $\mu = n\omega_r$. The final $\pi/2$ pulse about the $\hat{y}$-axis rotates the spins down. With some misalignment of $\delta\vec{k}$, there will be a coupling of the (harmonic of the)
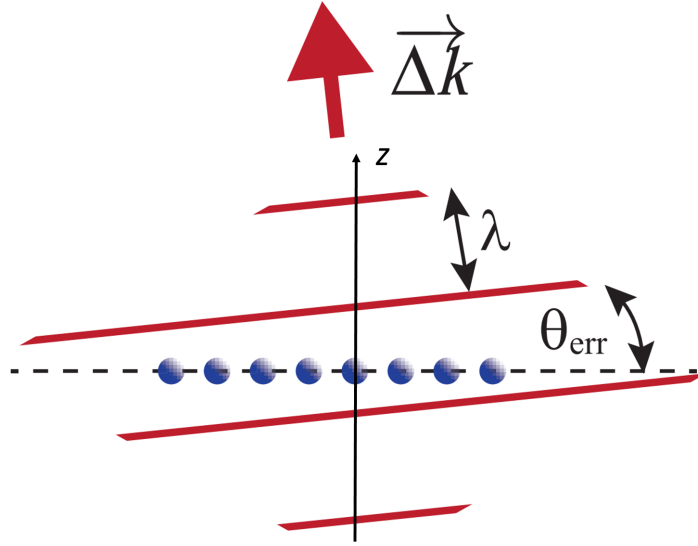
Figure 4.1: Illustration of ODF 1D lattice wavefronts (red lines). Ideally these wavefronts are aligned with the ion array (blue dots) such that $\theta_{err} = 0$. For this work, $\lambda = 2\pi/\delta\vec{k} = 900$ nm.
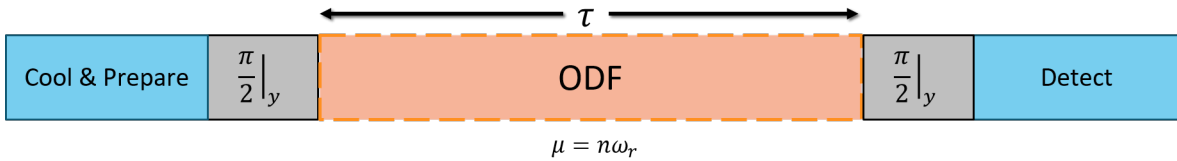
Figure 4.2: Illustration of experimental sequence used to optimize ODF wavefront alignment. a Ramsey sequence with interaction time τ is used. The interaction $\hat{H}_{\mathrm{ODF}}$ is applied for τ with the frequency of the resulting spin-dependent force tuned to a harmonic of the rotation frequency of the ion crystal, $\mu = n\omega_r$. The final $\pi/2$ rotation about the $\hat{y}$-axis rotates the spins down such that any dephasing due to coupling into the rotation of the crystal appears on average as decoherence - a shortening of the Bloch vector.

rotation of the ion crystal to the spins that will result in precession of the spins. Averaged over many iterations this signal becomes an inhomogeneous dephasing of the spins, which in this sequence is translated into an effective shortening of the Bloch vector. Thus the signal to be minimized is increased spin population in $|\uparrow\rangle$, where ideally the spins would end in $|\downarrow\rangle$ (with some shortening of the Bloch vector due to photon scattering).

In more detail (and following notes from John Bollinger), the full interaction is

$$\hat{H}_{\mathrm{ODF}} = \sum_i U \cos(\vec{k}_{eff} \cdot \vec{r}_i(t) - \mu t)\hat{\sigma}_z^i, \qquad (4.1)$$

where $\vec{k}_{eff} = (\vec{k}_\perp, k_z)$ is the effective wavevector of the 1D optical lattice and $\vec{r}_i(t) = (\rho_i \cos(\omega_r t + \phi_i), \rho_i \sin(\omega_r t + \phi_i), \hat{z}_i)$ is the position of ion i. Here the ion crystal is defined as being in the $x - y$ plane and the ODF wavevector is assumed to be in along the $\hat{z}$-axis with some component $\vec{k}_\perp$ in the $x - y$ plane.

The interaction can be rewritten as

$$\hat{H}_{\mathrm{ODF}} = U/2 \sum_i e^{ik_z \hat{z}_i} e^{i\left(k_{\perp,x}\rho_i \cos(\omega_r t + \phi_i) + k_{\perp,y}\rho_i \sin(\omega_r t + \phi_i) - \mu t\right)}\hat{\sigma}_z^i + \text{c.c.}. \qquad (4.2)$$

The above expression is accurate for a general misalignment in the $x - y$ plane, but we can redefine the axes, assume that $k_{\perp,y} = 0$, and set $k_{\perp,x} = k_\perp$. Then, in the Lamb-Dicke regime:

$$\hat{H}_{\mathrm{ODF}} = DWF\, U/2 \sum_i e^{i(k_\perp \rho_i \cos(\omega_r t + \phi_i) - \mu t)}\hat{\sigma}_z^i + \text{c.c.}, \qquad (4.3)$$

where $DWF = \exp(-\delta k^2 \langle \hat{z}_i^2 \rangle /2)$ is the Debye-Waller factor.

The exponential terms in the summation can be written in terms of Bessel functions:

$$e^{ik_\perp \rho_i \cos(\omega_r t + \phi_i)}e^{-i\mu t} + \text{c.c.} = \sum_{n=-\infty}^{+\infty} i^n \mathrm{J}_n(k_\perp \rho_i)e^{in(\omega_r t + \phi_i)}e^{-i\mu t} + \text{c.c.}. \qquad (4.4)$$

Next we consider the cases where $\mu = n\omega_r$. For each value of n, Eq. 4.4 reduces to a static term plus other terms with time-dependent exponentials that will tend to average to zero if the interaction time τ is large compared to a rotation period. Thus, for $\mu = \omega_r$ Eq. 4.4 reduces to

$$iJ_1(k_\perp\rho_i)e^{i\phi_i} - iJ_1(k_\perp\rho_i)e^{-i\phi_i} = -2J_1(k_\perp\rho_i)\sin(\phi_i). \tag{4.5}$$

Then, for this harmonic of the rotation frequency Eq. 4.3 becomes

$$\hat{H}_{\text{ODF}} = DWF\, U/2 \sum_i -2J_1(k_\perp\rho_i)\sin(\phi_i). \tag{4.6}$$

Similarly, for $\mu = 2\omega_r$, $\hat{H}_{\text{ODF}} = DWF\, U/2 \sum_i 2J_2(k_\perp\rho_i)\cos(2\phi_i)$ and for $\mu = 3\omega_r$, $\hat{H}_{\text{ODF}} = DWF\, U/2 \sum_i 2J_3(k_\perp\rho_i)\sin(3\phi_i)$, and so on.

For $\mu = \omega_r$, Eq. 4.6 results in precession of the spins by an angle

$$\theta_{n=1} = DWF\, U\tau/\hbar \sum_i -2J_1(k_\perp\rho_i)\sin(\phi_i). \tag{4.7}$$

The sequence depicted in Fig. 4.2 is sensitive to $\cos(\theta)$, where θ is an angle relative to the $\hat{x}$-axis, and the measured signal is

$$\langle P_\uparrow \rangle = 1/2 - 1/2 \langle \cos(\theta) \rangle. \tag{4.8}$$

Using Eq. 4.7, where we now integrate over all ρ (for an ion crystal of radius R) and ϕ, and the fact that $\int_0^{2\pi} \cos(x\sin(\phi))d\phi = 2\pi J_0(x)$, Eq. 4.8 can be rewritten as

$$\langle P_\uparrow \rangle_{n=1} = \frac{1}{2} - \frac{1}{2}\left(\frac{2}{R^2} \int_0^R \rho J_0 \left(\frac{2DWF\, U\tau}{\hbar} J_1(k_\perp\rho) \right) d\rho \right). \tag{4.9}$$

Assuming the argument of J_0 is small, Eq. 4.9 can be generalized to

$$\langle P_\uparrow \rangle_n = \frac{1}{2} - \frac{1}{2}\left(1 - \left(\frac{DWF\, U\tau}{\hbar} \right)^2 \langle J_n(k_\perp\rho)^2 \rangle \right), \tag{4.10}$$

where $\langle J_n(k_\perp\rho)^2 \rangle = 2/R^2 \int_0^R \rho J_n(k_\perp\rho)^2 d\rho$ represents an average over the area of the crystal.

Since the signal $P_\uparrow$ is proportional to $\langle J_n(k_\perp\rho)^2 \rangle$, then the ratio of the signal from adjacent harmonics is

$$\frac{\langle P_\uparrow \rangle_{n=m}}{\langle P_\uparrow \rangle_{n=m-1}} = \frac{\langle J_m(k_\perp\rho)^2 \rangle}{\langle J_{m-1}(k_\perp\rho)^2 \rangle} \tag{4.11}$$

If $k_\perp\rho \ll 1$ (that is, the alignment is good), then another small argument simplification is possible ($J_n(x) \approx \frac{1}{n!}(\frac{x}{2})^2$ for $x \ll 1$) and a quantitative analysis of the alignment is possible. Performing some algebra and integrating, Eq. 4.11 becomes
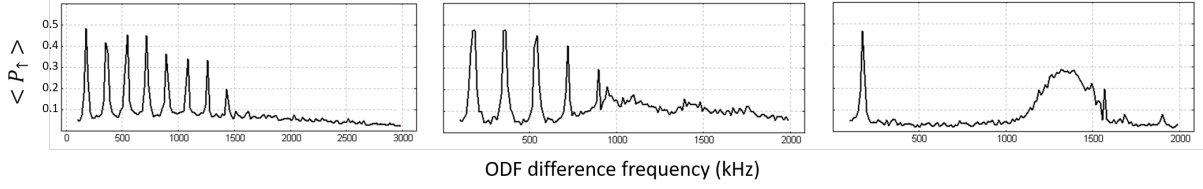
Figure 4.3: Rotational harmonics for various angles of misalignment. From left to right, the alignment is improved. The leftmost plot shows many harmonics of the rotational frequency and sign of the axial drumhead modes - indicative of very poor alignment of the ODF wavefronts. In the middle, the alignment has been improved but still several higher order harmonics are visible. On the right, now the drumhead mode spectrum is clear and only the first harmonic of the rotational frequency is visible - indicating good alignment of the ODF wavefronts. By comparing the ratios of the peaks of these harmonics, it is possible to back out a quantitative estimate of the misalignment angle (see main text).

$$\frac{\langle P_\uparrow \rangle_{n=m}}{\langle P_\uparrow \rangle_{n=m-1}} = \frac{1}{4m(m+1)} k_\perp^2 R^2. \tag{4.12}$$

Then, by solving for $k_\perp$, the angle of misalignment can be estimated given the radius R of the ion crystal since

$$\tan(\theta_{err}) = \frac{k_\perp}{\delta k} = k_\perp \frac{900 \text{ nm}}{2\pi}. \tag{4.13}$$

So, with that it is possible to estimate the misalignment error of the ODF wavefronts. To minimize such an error, the procedure we use is to perform the sequence in Fig. 4.2 and jump the difference frequency μ between the first four harmonics of the rotation frequency. By minimizing these features - and in particular, by minimizing the higher order harmonics first and then moving to lower order harmonics - by walking the two beams with sets of motorized mirror mounts $k_\perp$ can likewise be minimized.

The alignment procedure is robust week-to-week and can be checked by scanning the ODF difference frequency μ across several of the rotation frequency harmonics. By taking the ratio of pairs of the features associated with the rotation harmonics, Eqs. 4.12 and 4.13 can be used to ascertain the misalignment angle and determine if improvement is required.

4.2   Spin-dependent force amplitude calibration

For many experiments performed with the NIST Penning trap, an independent calibration of the applied spin-dependent force is necessary. In particular, for the theory used in extracting the mode occupation or measuring displacements of the ion crystal (techniques used extensively in the main experimental results of this thesis, Chs. 5, 6, 7) the amplitude of the force is a necessary parameter. This section will explain two procedures used to measure the amplitude of the ODF. The first involves measuring the ACSS of the beams individually with a known polarization, and then translating this into the expected optical dipole force amplitude. The second method is a more direct measure of the force, but relies on a more detailed analysis. The idea is to measure the precession of the spins under the influence of the ODF Hamiltonian in a regime where $\hat{H}_{\mathrm{ODF}}$ is dominated by mean field spin interactions [13].

4.2.1   ACSS calibration

Measuring the ACSS of the ions actually serves two purposes: it allows for aligning the beams by maximizing the intensity of the light on the ions, and allows for a measurement of the ACSS that can be used to calibrate the amplitude of the ODF. To do this measurement, first the spin-flip frequency (the qubit frequency, that is) is measured in a Rabi experiment. Then the Rabi sequence is repeated, but now with one of the two ODF beams on during the microwave π-pulse. The polarization for both ODF beams is rotated such that they are π-polarized, i.e. are linearly polarized along the $\hat{z}$-axis. The spin-flip frequency will be shifted by an amount $\Delta_{acss,0}$. In general, $\Delta_{acss} = (A_\uparrow - A_\downarrow)\cos^2(\phi_p) + (B_\uparrow - B_\downarrow)\sin^2(\phi_p)$, where $A_\uparrow(A_\downarrow)$ is the AC Stark shift of the $|\uparrow\rangle$ $(|\downarrow\rangle)$ state for a π-polarized beam (i.e. $\hat{\epsilon}$ parallel to $\hat{z}$) and $B_\uparrow(B_\downarrow)$ is the AC Stark shift of the $|\uparrow\rangle$ $(|\downarrow\rangle)$ state for a σ-polarized beam (i.e. $\hat{\epsilon}$ perpendicular to $\hat{z}$). However in this case, $\phi_p = 0$ and $\Delta_{acss,0} = A_\uparrow - A_\downarrow$. The spin-dependent force is set up such that $\Delta_{acss} = 0$ by rotating the polarization of the beams to $\phi_p \approx 65°$ (see Sec 4.3) subsequent to the ACSS measurement, and thus

$$(A_\uparrow - A_\downarrow) \cos^2(\phi_p) = -(B_\uparrow - B_\downarrow) \sin^2(\phi_p). \tag{4.14}$$

With the additional requirement that $F_\uparrow = -F_\downarrow$ (again, described in Sec. 4.3, and also from Eq. 2.20),

$$F_0 = 2\hbar\delta k(A_\uparrow \cos^2(\phi_p) - B_\uparrow \sin^2(\phi_p)) = 2\hbar\delta k(A_\downarrow \cos^2(\phi_p) - B_\downarrow \sin^2(\phi_p)), \tag{4.15}$$

it can be shown that $B_\uparrow = A_\downarrow \cos^2(\phi_p)/\sin^2(\phi_p)$. Thus,

$$F_0 = 2\hbar\delta k\Delta_{acss,0} \cos^2(\phi_p), \tag{4.16}$$

where $\Delta_{acss,0}$ is the ACSS (in units of angular frequency) with $\phi_p = 0$ for both beams measured separately and then averaged together. This is, then, a simple way to get an estimate of the expected ODF.

4.2.2 Mean field spin precession calibration

A more rigorous approach to measuring F_0, the amplitude of the spin-dependent force resulting from the ODF, involves applying the Ising Hamiltonian

$$H = \frac{1}{N} \sum_{i<j} J_{i,j} \hat{\sigma}_i^z \hat{\sigma}_j^z, \tag{4.17}$$

where $\hat{\sigma}_i^z$ is the z-component of the Pauli spin matrix for ion i, and $J_{i,j}$ is the amplitude of a coupling between ions i and j. This interaction is produced by way of the usual spin-motion coupling Hamiltonian, $\hat{H}_{\mathrm{ODF}} = F_0 \cos(\mu t) \sum_i \hat{z}_i \hat{\sigma}_i^z$, with the detuning $\delta = \mu - \omega_z = 2\pi/\tau$ (where τ is the interaction time) chosen to decouple the spin and motional degrees of freedom at the end of the sequence [34]. By selecting a detuning significantly closer to the COM mode than any other mode (for example, $\delta/(2\pi) = 1$ kHz), the Ising interaction is independent of the distance between the ions and the pairwise coupling between spins is homogeneous:

$$J_{i,j} \approx \bar{J} = \frac{F_0^2}{4\hbar m_{Be}\omega_z\delta}. \tag{4.18}$$
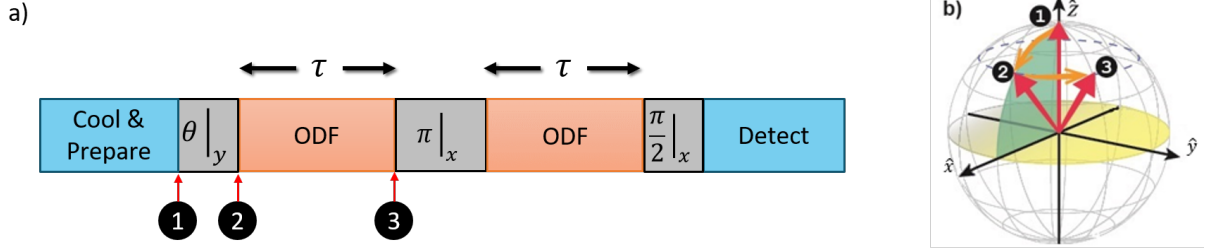
Figure 4.4: Illustration of the sequence used to measure mean field spin precession. a) After the ions are prepared in the state $|\uparrow\rangle$, a spin echo sequence is applied with an initial variable rotation of the spins by an angle θ and a final $\pi/2$ rotation about the $\hat{x}$-axis. b) Bloch sphere illustration of the spins precessing [13]. The numbers in black circles correspond to the point in the sequence with the same number in a).

From this expression, F_0 can be extracted if the quantity $\bar{J}$, which is the spin-spin coupling in the all-to-all coupling regime, is measured. This can be done by applying the Hamiltonian in Eq. 4.17 and measuring the resulting mean field spin precession [13, 14]. The mean field prediction for Eq. 4.17 is that this interaction for ion j can be modelled as an effective magnetic field due to the remaining $N-1$ ions, $H_{MF} = \sum_{j=1}^{N} \bar{B}_j \hat{\sigma}_j^z / 2$ with $\bar{B}_j = 2/N \sum_{i \neq j} J_{i,j} \langle \hat{\sigma}_i^z \rangle$ [13, 14]. Mean field theory refers to treating a Hamiltonian that describes the interactions between component objects to first order in the fluctuations about the average value of the components. For this to be a valid approximation, the product of the interaction strength and duration ($\bar{J}2\tau$) must be small. This effective magnetic field $\bar{B}_j$ will give rise to spin precession about the $\hat{z}$-axis in excess of what would result from Larmor precession, which can be measured.

Figure 4.4 illustrates the sequence used to measure the mean field precession of the spins. Following preparation of the spins in the $|\uparrow\rangle$ state, a variable duration microwave pulse rotates the spin by an amount θ. Upon application of the ODF Hamiltonian Eq. 4.17 the spins undergo precession about the $\hat{z}$-axis by an amount that depends on the initial tipping angle θ. A final $\pi/2$ microwave rotation about the $\hat{x}$-axis maps rotations into excursions above or below the equator of the Bloch sphere. Read out is performed with global fluorescence imaging, and the probability of detecting the $|\uparrow\rangle$ state is:
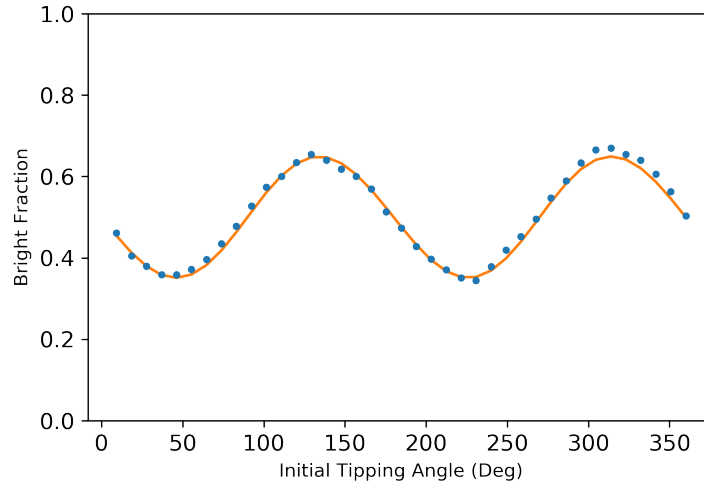
Figure 4.5: Mean field precession experimental data used for calibration of F_0, the amplitude of the spin-dependent force. The sequence used is depicted in Fig. 4.4. Here, the detuning $\delta/2\pi = 8$ kHz and the arm time $\tau = 125$ μs. The y-axis is the probability of the ions being in the $|\uparrow\rangle$ state, and the x-axis is the initial angle of rotation for the spins, θ. The blue points are experimental data and the orange line is a fit for $\bar{J}$ in Eq. 4.19. From the fit, $\bar{J} = 1276.7$ 1/s and so, $F_0 = 63.6$ yN from Eq. 4.18

.

$$P_\uparrow = \frac{1}{2}\left(1 - e^{(-\Gamma 2\tau)}\sin(\theta)\sin(2\bar{J}\cos(\theta)2\tau)\right). \tag{4.19}$$

Fitting to Eq. 4.19 allows for extracting the value of $\bar{J}$, which in turns yields the amplitude of the ODF, F_0. Figure 4.5 shows an example of such an experiment and fit.

4.3   ODF wavelength and polarization calibration

As was explained in Secs 2.4.1 and 2.4.2, the wavelength and polarization of the light used to produce the ODF are tuned such that the force on an ion in the state $|\uparrow\rangle$ is equal and opposite to the force on an ion in $|\downarrow\rangle$ ($F_\uparrow = -F_\downarrow$) and such that there is no net (time-independent) ACSS on the qubit transition. This section will explain the empirical calibrations used to determine the optimal wavelength and polarizations for the ODF beams.

The process for optimizing the ODF parameters involves multiple stages. After ensuring the ODF beams are well-aligned (see Sec. 4.1) and for a particular value of the laser frequency, the polarizations for the beams should be checked. The ODF laser beam path is schematized in Fig. 4.6. The 313 nm output of a resonant cavity doubler is split into two paths, both of which pass through a double-pass AOM arrangement to allow for precise and rapid frequency, phase, and amplitude control. Ideally, both beams will have linear polarization at the ions, with the angle of polarization relative to vertical (the trap axis) controlled by a computer-controlled $\lambda/2$ waveplate. To counteract circular or elliptical polarization that can be mixed in due to reflections off of mirror surfaces along the way to the ions, each beam passes through an $\lambda/4$ waveplate.

Setting the polarization of each beam nominally vertical (i.e. $\phi_p = 0$, see Fig. 2.8), we rotate $\lambda/4$ waveplate to maximize the ACSS's individually using an experiment like that described in the previous section 4.2.1. This should provide a good starting point with vertically polarized laser beams at the ions. With the linear polarization of both beams optimized, the $\lambda/2$ waveplates can now be set such that the ACSS on the qubit is nulled - that is that the ACSS's on the $|\uparrow\rangle$ and $|\downarrow\rangle$ are equal. This calibration can be performed with a Rabi experiment (4.2.1), but a Ramsey sequence

with a longer interrogation time allows for finer frequency resolution and thus more precise nulling of the ACSS on the qubit. The sequence is simply to rotate the spins to the equator of the Bloch sphere, turn on one of the two ODF beams, let the spins freely evolve for some period of time, and then attempt to rotate down. If the presence of the single ODF beam does not shift the qubit transition frequency, then the spins will end up in the dark $|\downarrow\rangle$ state. The sequence is repeated as a function of the computer-controlled $\lambda/2$ waveplates, and fitting to the fringe allows for precisely determining the optimal angle for achieving the desired polarization that nulls the ACSS on the qubit. With long Ramsey sequences (~ 1 ms), care must be taken to be centered on the proper fringe - typically this is done by reducing the interaction time until it's clear which feature should be focused on.

When the polarizations of the laser beams are not purely vertical or horizontal, reflections off of dielectric mirrors are no longer pure S- or P-polarized. This can result in some elliptical polarization at the ions when the $\lambda/2$ waveplates are rotated by angles other than $0°$ or $45°$ (corresponding to vertical or horizontal polarization). For an individual beam this does not change the condition that nulls the ACSS (i.e. the rotation angle of the $\lambda/2$ waveplate). However, if the relative phase shifts between the vertical and horizontal polarization components of the individual beams are not identical, then it is possible to acquire a spin-independent force that has a $90°$ phase shift relative to the spin-dependent force. To null this spin-independent force and maximize the spin-dependent force, the relative phase shift between the vertical and horizontal polarization of the second beam needs to be set to π relative to the first beam. We do this by introducing a variable phase shift to the horizontal polarization component relative to vertical for one beam, specifically a $\lambda/2$ waveplate is introduced to the beam path with its fast axis aligned vertically but on a rotation stage such that it may be twisted about an axis normal to the optical table. By performing a spin-echo Ramsey type experiment (with final rotation down, such that the spins ideally end in the $|\downarrow\rangle$ state) with the ODF tuned resonantly with the COM mode, the spin-dependent force will drive a spin-dependent displacement and subsequently reverse this displacement. However, if a spin-independent force is present a signal will remain. Repeating this experiment many times while
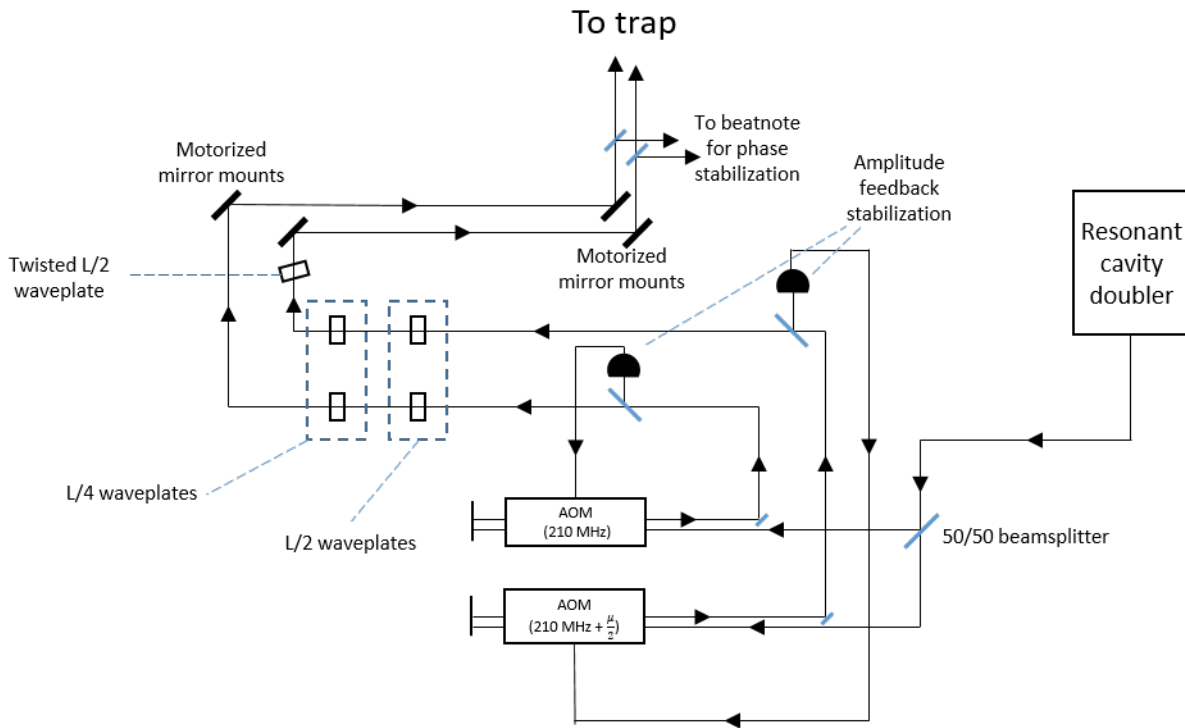
Figure 4.6: Schematic of the ODF laser beam paths. 626 nm laser light is piped over to the experiment optical table via fiber (not shown) and is coupled into a resonant doubling cavity, which outputs ∼100 mW of 313 nm light. A 50/50 beamsplitter directs two beams into a twin pair of double-pass AOM setups, with the frequency of one set to $\mu/2$ higher frequency such that there is a difference frequency between the two beams of μ. Feedback stabilization is used to control the power level in each beam and mitigate both noise and drift in the amplitude. Both beams pass through a $\lambda/2$ and $\lambda/4$ waveplate - which allow for setting the proper linear polarization of the beams - and one beam passes through a twisted $\lambda/2$ waveplate that acts as a phase shifter for horizontal relative to vertical polarization of that beam. Sets of computer controlled motorized mirror mounts are used for precise alignment of the beams on the ions. Finally, a pair of pickoffs just before the magnet are used to set up an interferometer to monitor the beatnote between the two beams and phase stabilize this signal.

twisting the $\lambda/2$ waveplate allows for nulling the spin-independent force, and thus maximizing the spin-dependent force.

Finally, the condition that $F_\uparrow = -F_\downarrow$ should be verified. Satisfying this condition depends on choosing the appropriate frequency for the ODF laser, as it is the detuning from the nearest transitions out of the two qubit states that sets the ACSSs, and thus the spin-dependent force, for these two states. The experimental sequence used to set this condition is similar to that described in Sec. 4.2.2, except the initial microwave pulse is set to be a $\pi/2$ rotation and the second application of the ODF has detuning $-\delta$ i.e. μ is switched from positively detuned relative to the COM mode to negative. The result is spin squeezing in the first arm that is - ideally - subsequently undone in the second arm. The π pulse in the middle of the sequence flips $|\uparrow\rangle \to |\downarrow\rangle$ such that if $F_\uparrow \neq -F_\downarrow$ there will be a rotation of the spins about the $\hat{z}$-axis. Varying the duration of the final rotation about the $\hat{x}$-axis will reveal this rotation by way of oscillations about the equator of the Bloch sphere. This experiment can be repeated for different laser frequencies until the signal is flat, and no oscillations are observed.

4.4   Qubit calibrations

Any quantum experiment relies on coherence in some form: the ability of the elements of the system to interfere with each other is a crucial part of what makes the experiment 'quantum'. Loss of coherence (decoherence) results in degradation (or in some cases destruction) of the experiment. The longevity of a quantum state is important because experiments are not instantaneous. Thus it is critical that the coherence time of our qubit exceed the duration of a single iteration of an experiment. However, noise in some form invariably finds its way in, and must either be mitigated or measured. This section will address calibrations performed to measure the regular and dominant noise sources present in our system that affect the qubit.

4.4.1 Spin flip frequency

The first steps with performing any measurements with the qubit involve calibrating the rotations required. That is, π and $\pi/2$ qubit rotations about different axes resonantly driven with our microwave source must be calibrated by measuring both the transition frequency between the two levels in the qubit (i.e. the spin-flip frequency) as well as the time required to drive the transition (the π time, t_π).

The simplest way to do this is to perform a Rabi experiment, where - after cooling and preparing the spins in the $|\uparrow\rangle$ state - the microwave drive is tuned to near the spin-flip frequency and turned on for a period of time t, causing the spins to rotate away from $|\uparrow\rangle$ and populate $|\downarrow\rangle$. The population in $|\uparrow\rangle$ is written

$$< P_\uparrow >= 1 - \frac{1}{1 + \left(\frac{\Delta}{\Omega}\right)^2} \sin^2 \left(\frac{\Omega t}{2}\sqrt{1 + \left(\frac{\Delta}{\Omega}\right)^2}\right), \tag{4.20}$$

where Δ is the frequency detuning of the driving field relative to the transition frequency, t is the driving time, and $\Omega = \pi/t_\pi$ is the Rabi rate.

By varying the detuning Δ across the transition frequency, the population is transferred from $|\uparrow\rangle$ to $|\downarrow\rangle$ and the minimum in $< P_\uparrow >$ can be fit to extract the spin-flip frequency. Figure 4.7 a) shows an example of such a Rabi experiment frequency scan where the data is fit to with Eq. 4.21 to extract the spin-flip frequency. Likewise, the driving time t can be varied with $\Delta = 0$ and t_π can be determined (Fig. 4.7 b)).

The frequency resolution of this Rabi experiment is limited by the time the drive is applied, t_π, which for the NIST Penning trap is typically ≈ 45 μs. For improved frequency resolution, a Ramsey sequence may instead be used. Here, the frequency resolution is instead set by the free evolution period by between two microwave $\pi/2$ rotations. The population in the state $< P_\uparrow >$ as a function of detuning Δ is

$$< P_\uparrow >= 1 - \sin^2 \left(\frac{\Delta T}{2}\right), \tag{4.21}$$

where T is the free precession time. Figure 4.8 illustrates a calibration of the spin-flip frequency using a Ramsey sequence with $T = 700$ μs.
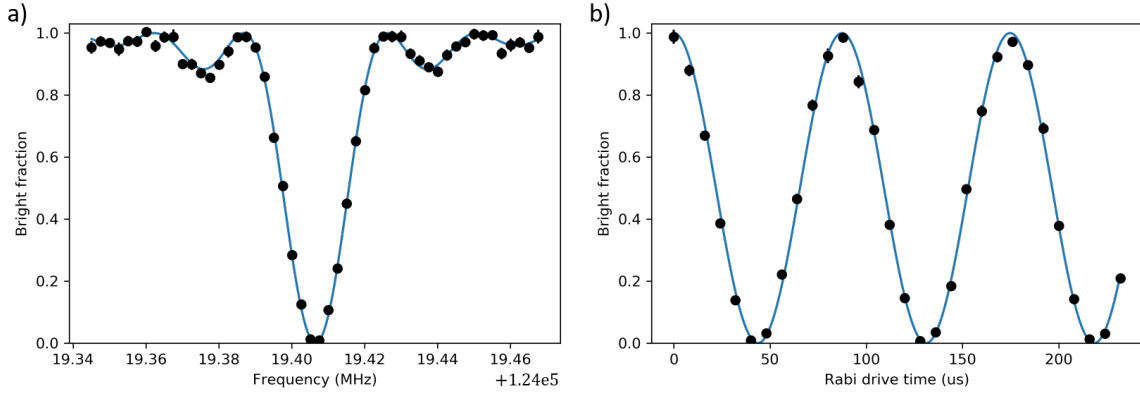
Figure 4.7: a) Rabi experiment where the frequency of the drive is scanned across the spin-flip transition. The black points are data with $t_\pi = 43.68$ μs, from b). The blue line is a fit using Eq. 4.20 and gives a spin-flip frequency of $f_{sf}/(2\pi) = 124.01940657(4)$ GHz. Note: the x-axis is offset by 124 GHz, for readability. b) Rabi experiment where the duration of the drive is varied. The black points are data using a spin-flip transition frequency measured just before, as in a). The blue line is a fit using Eq. 4.20 and from it $t_\pi = 43.683(2)$ μs.
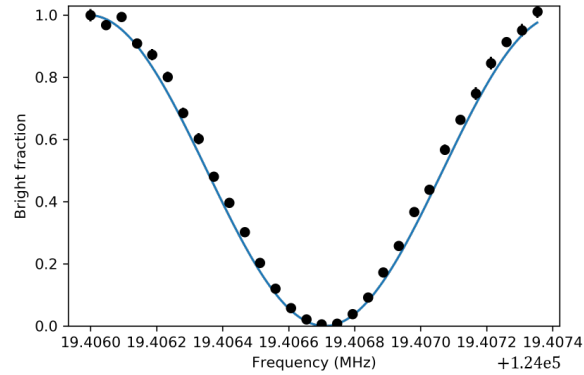
Figure 4.8: Central fringe of Ramsey experiment where the frequency of the drive is scanned across the qubit spin-flip transition. Black points are experimental data for a Ramsey interaction time $T = 700$ μs. The blue line is a fit using Eq. 4.21. The fit yields a spin-flip transition frequency of $f/(2\pi) = 124.019405995(3)$ GHz. Note: the x-axis is offset by 124 GHz, for readability.

4.4.2   Spin dephasing: magnetic field fluctuations and photon scattering

Noise is the limitation for most experiments, and characterizing the noise present in the system is crucial for understanding it. In the NIST Penning trap experiment - aside from (the (nearly) unavoidable) projection noise - spin dephasing due to magnetic field fluctuations and photon scattering from the off-resonant lasers used to produce the ODF (since Rayleigh rather than Raman scattering is dominant [35]) is the predominant source of noise. This section will explain the characterization that is regularly performed to ascertain the spin dephasing present in the system.

Since magnetic field fluctuations are an important source of noise that gives rise to dephasing of the spins, and though this noise can be mitigated by floating the optical table [36], nearly all experiments performed with the NIST Penning trap are in a spin-echo Ramsey sequence. So, to characterize the relevant spin dephasing due to magnetic field fluctuations, we perform a spin-echo Ramsey experiment while varying the free evolution time. Figure 4.9(a) shows the experimental data and a fit used to extract the observed dephasing, which we model as Gaussian noise due to magnetic field fluctuations. The contrast ($\hat{y}$-axis) represents the the length of the Bloch vector with 1 being fully coherent and a contrast of 0 meaning the state has decohered. If δ is the shot-to-shot frequency deviation of the spin-flip frequency from its mean, then the length of the Bloch vector can be written as $< \hat{\sigma}_x >=< \cos\phi >= \exp(-0.5(2\tau\delta_{rms})^2)$, where $\phi = \delta 2\tau$ is the phase difference between the microwaves driving the spin flip and the spins and 2τ is the total interaction time of the sequence. By fitting to the decay of the Bloch vector length (the contrast) as plotted in Fig. 4.9, the rms frequency fluctuations of the spin-flip frequency due to magnetic field fluctuations can be extracted. Typically, δ_{rms} is on the order of 10s of Hz.

Having characterized the background noise due to magnetic field fluctuations, the next step is to turn on the ODF beams - the other significant contributor to spin dephasing. Each of the two ODF beams causing spin dephasing due to off-resonant light scattering. In the regime the NIST Penning trap operates in, Rayleigh scattering is the dominant source of decoherence over Raman
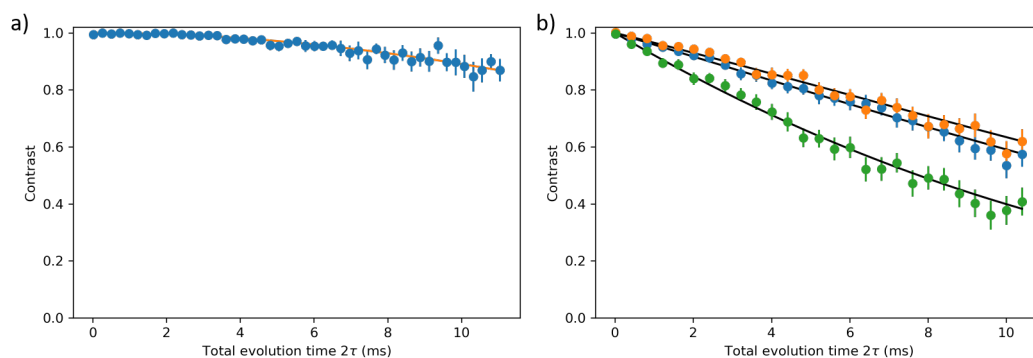
Figure 4.9: a) Dephasing due to magnetic field fluctuations. Blue points are data and the orange line is a fit that yields rms spin-flip frequency fluctuations of 48 Hz. b) Dephasing due to photon scattering from the off-resonance lasers that produce the ODF. The blue and orange points are data for the single ODF beam decoherence rates, 'upper' and 'lower' beams respectively. The green points are data for both beams on together. The black lines are fits to the data. In this case, the upper, lower, and combined rates are 34, 41, and 81 1/s, respectively.

scattering [35]. Typically, $\Gamma_{el} \approx 4\Gamma_{ram}$. As a result, the dominant effect of photon scattering here is spin dephasing rather than spin-flip errors. To empirically measure this dephasing rate, again a spin-echo Ramsey sequence is used - now with the ODF turned on during the two free evolution periods each of time τ (for a total interaction time of 2τ). Similar to before, the contrast is given by $< \hat{\sigma}_x >= \exp(-\Gamma_{tot}2\tau)$, where $\Gamma_{tot} = \frac{1}{2}(\Gamma_{ram} + \Gamma_{el})$. This procedure is performed with each beam individually, followed by both beams together. Figure 4.9(b) is an example of such a dataset. As a result of the ACSS being nulled as well as the amplitudes stabilized for each beam, decoherence due to laser power fluctuations is negligible. Additionally, good agreement between the sum of the individual decoherence rates and the combined decoherence rate indicates additional decoherence due to spin-motion entangelement is not present. Thus the dominant noise source - spin dephasing due to photon scattering (in particular, elastic Rayleigh scattering) - may be characterized.

4.5   Spin precession induced by ion motion

Measuring the spin precession that is produced through the application of a spin-dependent force (Eq. 2.14) gives information that can be used to evaluate the occupation of a particular motional mode of the ion crystal (Sec. 4.6 and Ch. 5) as well as driven motion of the crystal (Ch. 6). This technique is useful in the Penning trap setup, as it is simpler to implement than using Raman sidebands for the case of a qubit frequency of 124 GHz. This section will summarize results [12] that describe the observed spin precession due to the appropriate application of Eq. 2.14, which is relevant for much of the rest of this thesis. More details are available in that paper, as well as [37].

The COM mode is, for the Penning trap experiment, the most used mode. Therefore, the derivation in [12] outlined here considers just the COM mode. The interaction Hamiltonian 2.14 for the spins coupling just with the COM mode is

$$\hat{H}_{\text{ODF}} = F_0 \cos(\mu t + \phi) \frac{z_0}{\sqrt{N}} \left(\hat{a} e^{-i\omega_z t} + \hat{a}^\dagger e^{i\omega_z t} \right) \sum_{i=1}^{N} \hat{\sigma}_i^z, \tag{4.22}$$

where $z_0 = \sqrt{\hbar/(2m_{Be}\omega_z)}$ is the ground state wave function size of a single ion, $\hat{a}(\hat{a}^\dagger)$ is the lowering (raising) operator for the COM mode, and ϕ is the phase of the ODF. With the ODF frequency $\mu \approx \omega_z$, the resulting spin-dependent displacement dominates over other signals (for moderately large excitations, see Sec. 5 for details) and the evolution of the system due to Eq. 4.22 is dictated by the product of spin-dependent displacement operators

$$\hat{D}(\alpha) = \prod_{i=1}^{N} \exp([\alpha\hat{a}^\dagger - \alpha^\star\hat{a}]\hat{\sigma}_i^z).$$
(4.23)

For $\mu = \omega_z$, the amplitude of the spin-dependent excitation of the COM mode is

$$\alpha(\tau, \phi) = -i\frac{F_0 z_0 \tau}{2\hbar\sqrt{N}}e^{i\phi},$$
(4.24)

where τ is the time the ODF is applied. A spin-independent displacement is defined as

$$\hat{D}(\alpha_0) = \exp([\alpha_0\hat{a}^\dagger - \alpha_0^\star\hat{a}].$$
(4.25)

If the ions begin in a coherent state of COM motion, then the initial state is $|\psi\rangle = |\uparrow\rangle |\alpha_0\rangle$. With a $\pi/2$ qubit rotation, the state becomes $|\psi\rangle = 1/\sqrt{2}(|\uparrow\rangle + |\downarrow\rangle)\hat{D}(\alpha_0) |0\rangle$. After application of the ODF for a time τ, the state evolves to

$$|\psi\rangle = \frac{1}{\sqrt{2}}e^{-i\theta} |\uparrow\rangle |\alpha + \alpha_0\rangle + \frac{1}{\sqrt{2}}e^{i\theta} |\downarrow\rangle |-\alpha + \alpha_0\rangle$$
(4.26)

where $\theta = \text{Im}(\alpha\alpha_0^\star)$. By evaluating the expectation values $\langle \hat{S}_x \rangle$ and $\langle \hat{S}_y \rangle$, it can be shown that the effect of the ODF is to cause a coherent rotation of the spins about the $\hat{z}$-axis by an amount $\theta_{\text{coh}} = 4\text{Im}(\alpha\alpha_0^\star)$. This angle can then be read out by applying another qubit rotation and performing state-dependent readout. The spin precession θ_{coh} is a sensitive measure of COM motion excited by electric fields (see Chs. 6 and 7) and also can be used as a diagnostic for the occupation of a motional mode, as will be outlined in the subsequent section (and also used extensively in Sec. 5).

4.6   Measuring the mode occupation

The thermal occupation of the COM mode is a useful diagnostic, and also a parameter needed for other experimental analysis. This section will give an overview of the procedure used to perform this measurement, as well as the theory needed to extract a value for the COM mode occupation.

From the previous section, application of the ODF resonant with the COM mode $\mu = \omega_z$ results in a rotation of the spins by an angle $\theta_{\mathrm{coh}} = 4\mathrm{Im}(\alpha\alpha_0^\star)$. If the sequence used is instead a spin echo (useful for mitigating noise from magnetic field fluctuations) as depicted in Fig. 4.10, then the spin-dependent displacement is modified to

$$\alpha = \frac{F_0 z_0}{2\hbar\sqrt{N}} \frac{(1 - e^{i\delta\tau})}{\delta} \left(1 - e^{(i\delta(\tau+t_\pi)+\phi_{\mathrm{ODF}})}\right),\tag{4.27}$$

where τ is the duration of each ODF application on either side of the π-pulse, t_π is the duration of the $\pi-$ pulse, $\delta = \mu - \omega_z$, and ϕ_{ODF} is the phase of the ODF in the second arm relative to the first. For the sequence in Fig. 4.10, $\phi_{\mathrm{ODF}} = 0$ and the final qubit rotation results in a signal

$$< P_\uparrow >= \frac{1}{2} \left(1 - e^{-\Gamma_{tot}2\tau} e^{-2|\alpha|^2(2\bar{n}+1)} \cos(4J)^{N-1}\right),\tag{4.28}$$

where $\bar{n}$ is the COM mode mean phonon number, and Γ_{tot} is the dephasing rate due to photon scattering from the ODF lasers (Sec. 4.4.2). The spin-spin coupling J (described in Sec. 4.2.2) has a dependence on the frequency detuning δ, which is given by

$$J = \frac{F_0^2 z_0^2}{4\hbar^2 N\delta^2}(2\delta\tau + \sin(\delta(2\tau + t_\pi)) + \sin(\delta t_\pi) - 2\sin(\delta\tau) - 2\sin(\delta(\tau + t_\pi))).\tag{4.29}$$

Using the sequence in Fig. 4.10 and varying the ODF frequency μ across the COM mode frequency ω_z, the lineshape of the COM can be fit to and the COM mode thermal occupation can be extracted. Figure 4.11 shows one such scan with typical parameters, $F_0 = 66$ yN and $\tau = 200$ μs and with a fitted value of $\bar{n} = 4.92 \pm 0.4$ consistent with the Doppler cooling limit. Note that for the sequence used here, the signal exactly on resonance with the COM mode is nulled: the spin precession accumulated in the first arm of the ODF is cancelled by that accumulated in the second
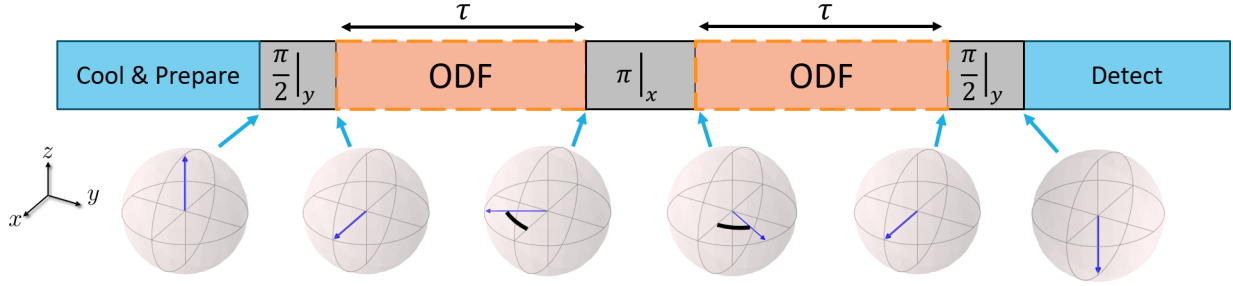
Figure 4.10: Sequence used to read out the COM mode occupation. The spins are prepared in the $|\uparrow\rangle$ state before being rotated down along $\hat{x}$. With the ODF frequency tuned to resonance with the COM mode frequency $\mu = \omega_z$, the ODF is applied for a time τ and spin precession occurs. The amplitude and phase of the motion will be governed by a thermal distribution, which is reflected in shot-to-shot variation of the angle of precession. Following a π rotation of the spins around the $\hat{x}$-axis, another application of the ODF results in an equal amount of spin precession (again, for the case $\mu = \omega_z$) - but since $|\uparrow\rangle \rightarrow |\downarrow\rangle$ due to the π-pulse, the initial rotation is undone. The result for the case $\mu = \omega_z$, then, is that the spins end up in the dark $|\downarrow\rangle$ state.
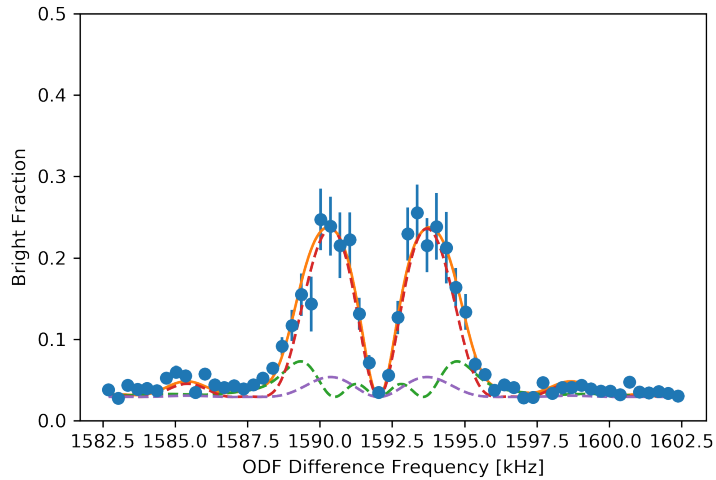
Figure 4.11: Experimental data, fit, and theory curves illustrating the COM mode thermometry. The blue dots are experimental data for the sequence in Fig. 4.10 with $\tau = 200$ μs and $F_0 = 66$ yN. The orange solid line is a 2-parameter fit to the data for the mode frequency $\omega_z = 1592.04 \pm 0.03$ kHz and mean phonon number $\bar{n} = 4.92 \pm 0.4$. The fit makes use of Eq. 4.28. The red dashed line is a theory curve from Eq. 4.28 but with $J = 0$, i.e. ignoring the contribution of the spin-spin interactions. The purple dashed line is the same expression but with $\bar{n} = 0$, illustrating the contribution of the zero-point motion. The green dashed line is a theory curve (again, Eq. 4.28) but now with $\alpha = 0$, i.e. ignoring the spin-motion coupling term and highlighting the spin-spin component of the interaction.

arm. If the phase of the ODF in the second arm was shifted by π relative to the first arm, then these two signals would accumulate coherently and instead there would be a peak on resonance. This feature will come in handy later, when cancelling thermal noise is crucial for sensing small displacements caused by resonant electric fields (see Ch. 7). The dashed lines are theory for different limits. The orange dashed line neglects the contribution from the spin-spin interactions (that is, $J = 0$ in Eq. 4.28). In the regime relevant for this data, this is a reasonable approximation. The spin-spin contribution is in green ($\alpha = 0$) and the zero-point motion ($\bar{n} = 0, J = 0$) is in purple. An interesting feature of this technique is that it is sensitive to the zero-point motion. In a different parameter regime (in particular, when F_0 is large and/or $\bar{n}$ is small), both the zero-point motion and the spin-spin interactions play a significantly larger role in the COM mode lineshape (see Ch. 5).

4.6.1 COM mode heating rate

The same experiment described in the preceding section can be used to ascertain the heating rate of a mode. In particular, we are interested in the heating rate of the COM mode. This can be done by applying the sequence from Sec. 4.6 but with a variable wait time after the state preparation. The mode will heat during this wait, and by measuring the mode occupation for various wait times the heating rate can be extracted. Figure 4.12 shows an example of this heating rate measurement following EIT cooling. A fit to this data yields a heating rate of 58 ± 5 quanta/s. A typical upper bound on the heating rate is approximately 100 quanta/s. Note that the COM mode heating rate due to electric field noise increases linearly with the number of ions. Therefore, this measurement performed with $N = 100$ ions provides a single-ion heating rate (due to noisy electric fields) limit of 0.6 quanta/s.

4.7 Spinning up the ions

The method for loading ions has been detailed in Ch. 3. However, after loading ions we follow a protocol to gather the ions to the center of the trap and cool them to a Coulomb crystal,
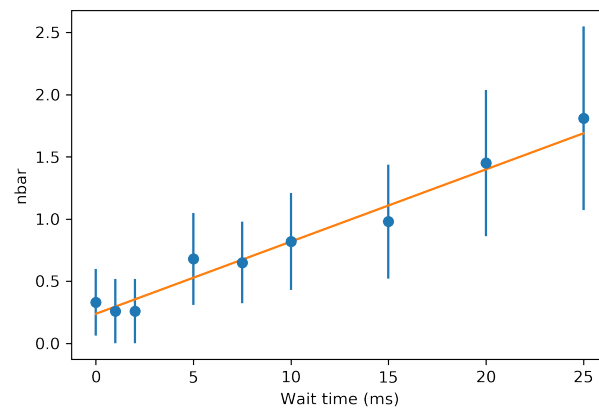
Figure 4.12: By measuring the COM mode occupation after a variable wait, the heating rate can be extracted. Blue points are data following a fit to the COM mode lineshape, as was demonstrated in Sec. 4.6. The orange line is a fit to the data and gives a heating rate of 58 ± 5 quanta/s.

which is what this section will describe.

When loading via electron impact ionization, it has been empirically observed that the ions do not appear in the center of the trap. This could be due to off-center loading, or it could be related to higher-than-desired energy in the ions due to the ionization or transport processes. As a result, the parallel Doppler cooling (Ch. 2) laser does not interact with the ions and they are not cooled. Thus, steps must be taken to gather and cool the ions: 'spinning up' the ions. With photoionization, the ions appear in the center of the trap and are cold immediately after loading. However, due to an effect currently not understood, the COM mode of the ion crystal immediately after loading is excited (has an elevated mode occupation). To mitigate this, the ions are left in the trap for some time (typically more than one hour) without the Doppler cooling lasers on (to avoid converting to BeH^+), whereupon the COM mode has relaxed to a more typical state. At this point, the ions need to be spun up because they have expanded outwards due to a small net torque.

To gather the ions to the center of the trap, a torque is applied with the perpendicular cooling laser (Ch. 2). The intensity of the perpendicular laser is maximized and the focusing lens is displaced by ≈ 2 mm such that the focused beam is displaced as far from the center of the trap as the trap geometry allows. Moving the perpendicular beam off-center enables this light to interact with ions in this region. To compress the ions and move them toward the center of the trap, where the parallel cooling laser will more effectively cool them, the perpendicular cooling laser frequency is swept from red- to blue-detuned with respect to the typical Doppler cooling frequency (Ch. 2). The parallel cooling light is blocked with a remotely controlled shutter prior to sweeping to higher frequencies to prevent heating the axial modes of the ions. At a blue-detuned frequency, photons interact with the magnetron (rotational) motion of the ions. The effect is that the perpendicular cooling laser provides a torque by giving energy to the magnetron motion, compressing the ions. The laser position is stepped back (in roughly 200 μm increments) to close to the center, and the laser frequency is swept to the blue at each step. At the conclusion of this process, the ions have been compressed ('spun-up') and are effectively cooled by both parallel and perpendicular Doppler

cooling beams, resulting in a Coulomb crystal of ions.

4.8   Ion number calibration

Once the ions have crystallized and the Doppler cooling lasers are aligned, it is useful to learn the number of $^9Be^+$ ions that are present in the crystal. To do this, we vary the radial confinement by changing the rotation speed of the crystal with the rotating wall. If the ions are initially relaxed into a 2D array, increasing the rotation speed will compress the ions and at some point transition to a 3D crystal with 2 planes. This transition from a single plane to two planes of ions occurs at a particular frequency that depends on the number of ions. The axial, out-of-plane, drumhead modes can be characterized with a stiffness matrix. When the eigenvalues of this matrix are real, the crystal is stable. The point at which the ion crystal transitions between one and two planes is an instability that occurs when the eigenfrequencies become imaginary. This is analogous to the zigzag transition for ions in a linear string. By numerically varying the rotation frequency and determining the eigenvalues of the stiffness matrix, the frequency for the transition from 1 to 2 planes is identified as the point when the eigenvalues become imaginary [38].

As a result, the transition frequency may be used as a proxy for ion number (Fig. 4.13). Typically, this allows for estimating the ion number with an uncertainty of ∼5%. Of course, on-axis imaging with single ion resolution allows for exactly counting the number of ions. In practice, this imaging has not always been set up and is more cumbersome to use. However, it serves as a good check and has been used to confirm the validity of the one-to-two plane transition proxy as an ion number calibration.

4.9   Trap alignment via zero-frequency modes

Ideally, the symmetry axis of the Penning trap and the axis of the magnetic field would be identical. The magnetic field defines the symmetry axis for the ion crystal: a planar crystal will be perpendicular to the magnetic field. However, in practice this is challenging to achieve. A misalignment between the magnetic field and electrode symmetry axis will thus result in an
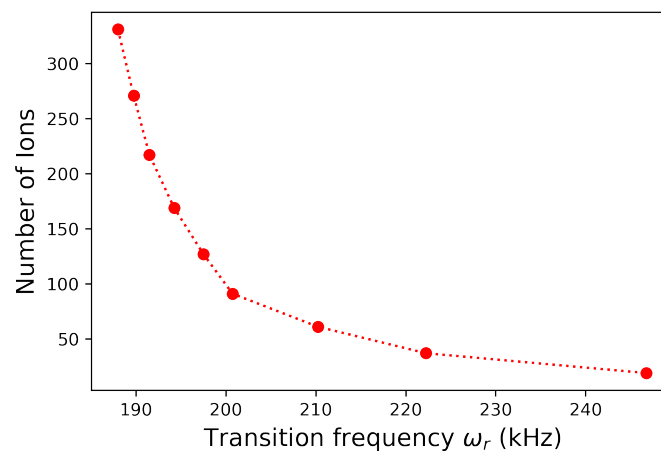
Figure 4.13: One-to-two plane transition frequency for different numbers of ions, calculated numerically [38]. The red points correspond to the number of ions that provides a closed hexagonal shell structure (with the number of shells $s = 10, 9, 8, 7, 6, 5, 4, 3, 2$ from left to right). The dashed line is a linear interpolation between the points.
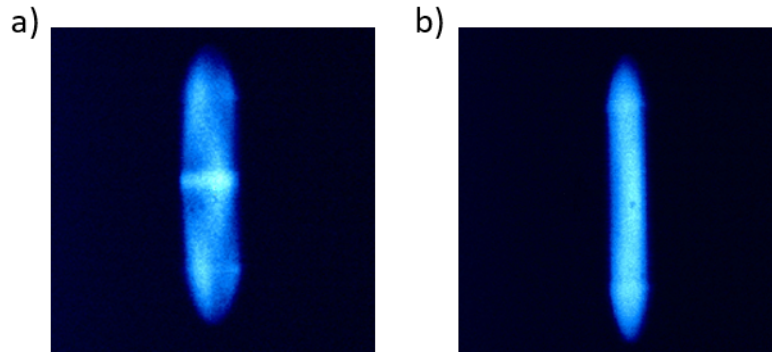
Figure 4.14: Sideview images of excited zero-frequency plasma modes. The excitation of these modes at particular rotation frequencies is indicative of a misalignment of the trap relative to the magnetic field (see main text). a) A mode is visibly excited with just the perpendicular cooling beam. At this point the trap is not well-aligned. b) After some effort to better align the trap to the magnetic field axis, the crystal rotation frequency can be increased up to 1.1 MHz (pictured) with no observable excitations of plasma modes.

asymmetry in the trap. This will result in torques produced both by ion image charges in the electrodes (that otherwise would cancel) and by the restoring force of the harmonic potential from the electrodes. The resulting net torque will tend to expand the ions, and may also lead to heating of the radial modes. Thus, static magnetic field errors (i.e. a tilt of the trap with respect to the axis of the magnetic field) can excite plasma modes [39] and cause heating of the ions, as well as unwanted torques and mixing of radial and axial degrees of freedom. Measuring the excitation of plasma modes provides a way of minimizing the magnetic field misalignment error.

To align the trap to the magnetic field, heating due to excitation of zero-frequency (electrostatic) plasma modes is minimized. With the ions rotating at a mode frequency, the presence of a static field error will excite the mode. Typically, this is done with the dipole rotating wall, as the quadrupole rotating wall seemed to produce some constant heating at particular higher frequencies - the cause of which is unknown. If the Doppler cooling laser is set to its usual detuning, fluorescence will decrease if the plasma is heated. If the cooling laser is substantially detuned, the fluorescence will instead increase. By measuring this fluorescence on a PMT while tilting the trap, the excitation of the mode can be nulled and the alignment of the trap to the magnetic field improved.
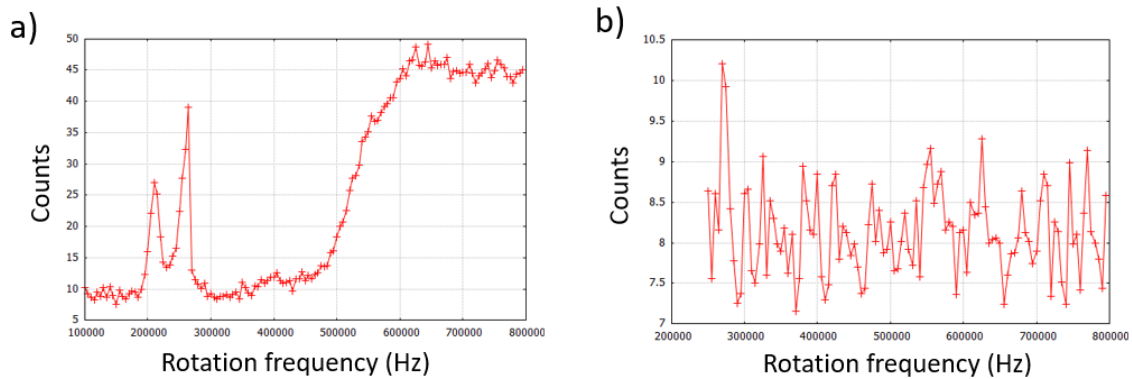
Figure 4.15: With the parallel beam detuning from resonance, the counts collected on a PMT serve as a useful proxy for heating resonances due to excitations of plasma modes. By scanning the rotation frequency and measuring the counts in the sort of experiment described in the next, zero-frequency modes can be observed and minimized. a) Initial scan of rotation frequency while collecting photons from parallel Doppler cooling beam. A pair of resonances at $\sim$200 and $\sim$270 kHz are observed as well as a broad heating resonance indicative of poor alignment of the trap axis to the magnetic field. b) After improving the alignment, no heating resonances are observed over this range of frequencies, indicating good alignment of the trap axis to the magnetic field.
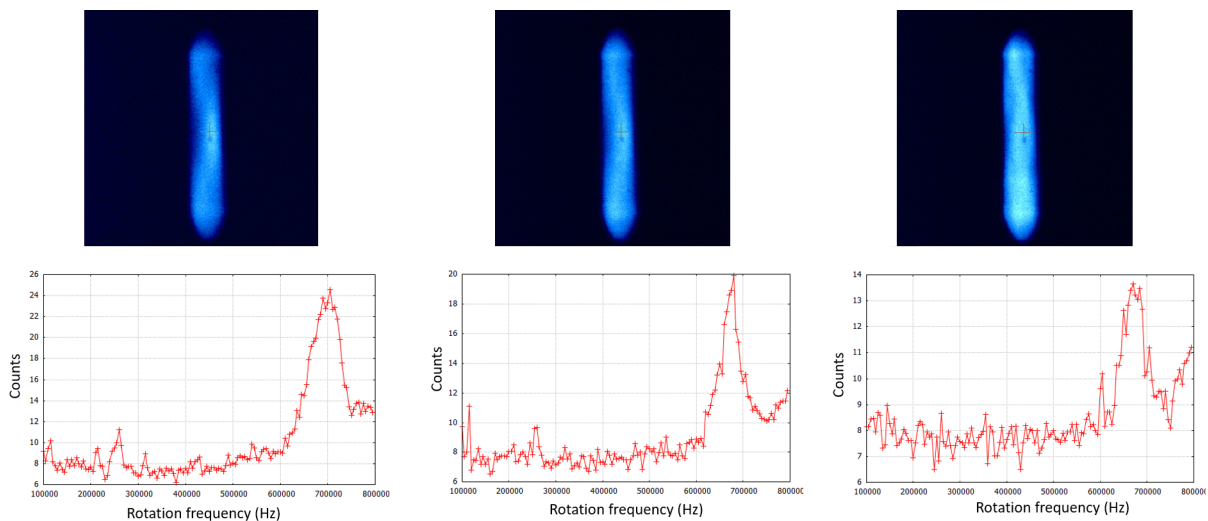
Figure 4.16: After minimizing heating resonances from lower frequency modes, a higher frequency mode (at 700 kHz) is observed and minimized. The sideview images and counts vs rotation frequency scans correspond top to bottom. By tilting the trap relative to the magnetic field axis, the excitation of this mode is reduced (from left to right).

4.10   Parallel beam alignment

Another source of unwanted torques due to asymmetries - like the alignment of the trap to the magnetic field - is the (mis)alignment of the parallel cooling beam to the ion crystal (magnetic field axis). If the parallel beam is perpendicular to the plane of the ion crystal, then it will exert no torque and couple only to the axial degree of freedom. However, if there is some misalignment, then the parallel beam will in fact torque the ion crystal. This may be another mechanism for coupling between axial and planar modes - an unwanted effect. To rectify misalignment, torque due to the parallel beam may be observed (without the presence of the perpendicular beam) and empirically minimized by adjusting alignment. However, a more rigorous approach involves minimizing Doppler shift fluorescence asymmetry from the parallel beam.

A component of the parallel beam in the plane of the ions can be observed by way of asymmetric illumination due to the Doppler shift from rotation of ions - a fast rotation means this is a more pronounced effect. To do this, the ions are spun up to a rapidly rotation state with the perpendicular cooling beam. With the perpendicular beam far blue-detuned the ion crystal will become very spread out - beyond the Brillouin limit [40]. With the ions in this rapidly rotating state, the perpendicular beam is switched off and just the parallel is brought in (very slowly) from far red-detuned to close to resonance. As the ions begin to fluoresce from the parallel beam, the symmetry of the illumination will become apparent. By walking the parallel beam around, any asymmetry can be corrected and the alignment improved.

4.11   Trapping potential anharmonicity

The ideal potential for a Penning trap is purely harmonic along the $\hat{z}$-axis: terms in the multipole expansion (Sec. 2.1.4) C_4 and above should be zero. Based on modeling of the trap electrode geometry (Sec. 3.2.1), it is possible to set the voltages on the appropriate electrodes such that the C_4 contribution is nulled. In practice, this is an imperfect approach and there may remain some anharmonicity to the potential. To better null this potential anharmonicity, an empirical
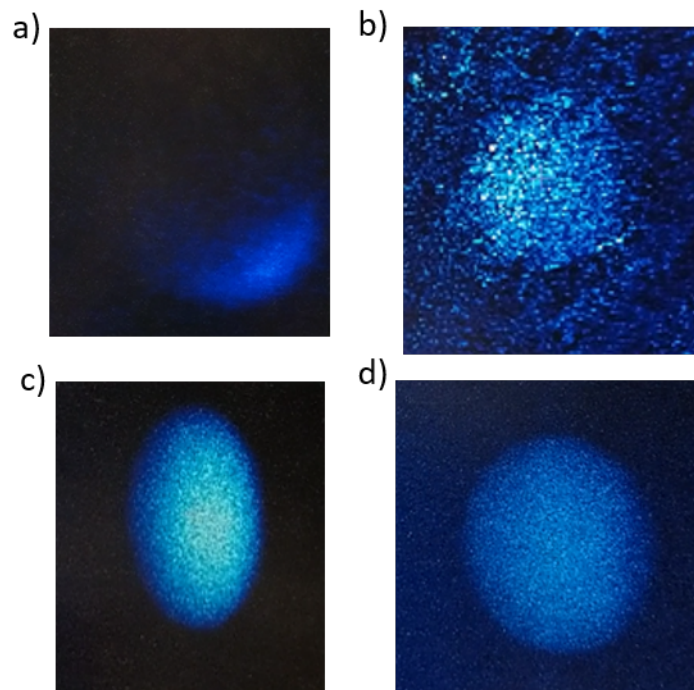
Figure 4.17: For a rapidly rotating ion crystal, a component of the parallel Doppler cooling beam in the plane of the crystal will result in an asymmetry of the observed fluorescence. a) Bottom view image of an ion crystal with poorly aligned parallel cooling beam. There is a visible asymmetry in the observed fluorescence. b) After realigning the parallel beam, the asymmetry is reduced. The apparent increased fluorescence on the upper left section of the crystal is due to background light scatter (the overall fluorescence is much reduced here, necessitating higher gain and thus higher background). c) A sideview image taken in parallel with a). An asymmetry is also visible from the side. d) Another sideview image, now taken simultaneously with b). The ion crystal is uniformly illuminated, indicating good parallel beam alignment.

approach would be useful.

One way of doing this is to look for a shift in the COM mode frequency as a function of rotation frequency. For a cloud of pure beryllium ions in a harmonic potential, the COM mode frequency is independent of the rotation frequency. However, if there is an anharmonic C_4 contribution to the potential, the COM mode frequency will depend on the rotation frequency [41] (or, equivalently, the radial extent of the crystal).

From [41], the shifted COM mode frequency is given by

$$\omega^2 = \omega_z^2 \left(1 + \frac{6}{5}\beta_4 \frac{b^2 - a^2}{r_w^2} \right), \tag{4.30}$$

where ω_z is the trap frequency (the unshifted COM mode frequency), a and b are the radius and half-length of the ion cloud, respectively, $r_w = 1$ cm is the electrode radius, and $\beta_4 = r_w^2 C_4/C_2$ is a unitless parameter describing the first anharmonic correction. With $\alpha = b/a$ and assuming this is a small correction:

$$\frac{\delta\omega}{\omega_z} \approx \frac{6}{10}\beta_4 \frac{a}{r_w}^2 (\alpha^2 - 1). \tag{4.31}$$

Equation 4.31 gives the fractional shift in the COM mode frequency due to an anharmonic correction to the trapping potential. By empirically measuring the COM mode frequency as a function of the rotation frequency or radial extent of the cloud, it is possible to minimize this shift and thus minimize the anharmonic component of the potential. Figure 4.18 illustrates Eq. 4.31 for a few values of C_4 as a function of the rotation frequency while holding all other parameters fixed. Note that this analysis assumes a pure $^9\text{Be}^+$ ion cloud. When impurities are added, additional frequency shifts will be present that are dependent on the rotation frequency of the crystal.

4.12   Magnetic field gradient

Axial gradients in the magnetic field may exist. If the bore of the superconducting magnet is clear, then the magnetic field may be measured and shimmed such that the gradient is minimized.
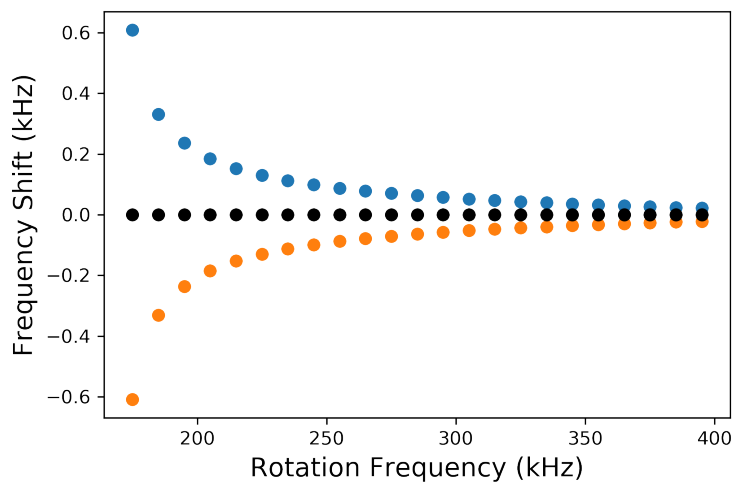
Figure 4.18: In the presence of an anharmonic trapping potential, the COM mode frequency has a dependence on the rotation frequency (radial extent of the ion crystal). The y-axis is the shift away from the bare COM mode frequency, plotted as a function of the rotation frequency on the x-axis. The blue, black, and orange points are for $r_w^4 C_4 = -100, 0$, and 100 V, respectively.

However, the introduction of the trap and other equipment into the bore may result in gradients in the field appearing. The magnetic field gradient can be measured, however, by displacing an ion crystal along the trap axis and measuring the qubit transition frequency (spin flip frequency). Since this frequency depends on the magnetic field, if the magnetic field is varying along the $\hat{z}$-axis this will be reflected in the spin flip frequency. Figure 4.19 illustrates an example of such a measurement. Each point is a measurement of the spin flip frequency performed in a Ramsey sequence, for different axial displacements of the ions. Ideally, this can be used to null out any gradient present, but this can be challenging as there is generally some risk of a magnet quench associated with inserting the lead into the magnet to adjust the superconducting shim coils.
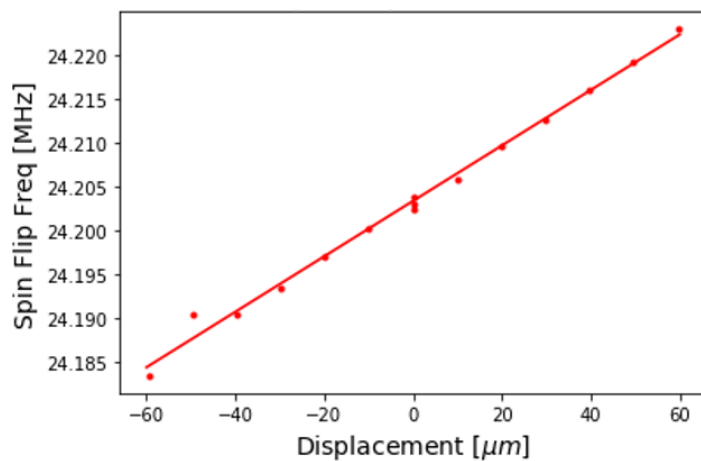
Figure 4.19: Measurement of magnetic field gradient. The ions are displaced a known distance along the axis of the trap by a static, calibrated voltage. Then, the spin flip frequency is measure in a Ramsey sequence. By plotting the measured frequency of the spin flip (which depends on the magnetic field) vs the displacement, any gradient in the magnetic field may be measured. In this case, the gradient is 3.15e-4 MHz/μm (44586.046 gauss / 124013.46 MHz) = 1.13e-4 gauss/μm.

Chapter 5

Electromagnetically-induced transparency cooling

This chapter will focus on the experimental demonstration of electromagnetically-induced transparency (EIT) cooling in the NIST Penning trap. Following an explanation of motivation and a survey of prior work, the general concept of EIT cooling will be described. Subsequently, a brief theoretical description will be provided. More theoretical details relevant for this experiment have been working out by collaborators [42, 43]. The experimental results have been summarized and published [17]. However, more detail of the experimental setup and results will be provided in this chapter.

5.1   Overview, interest, and prior work

Generally speaking, achieving colder temperatures of atomic (and many physical systems) enhances performance. For trapped ions, higher fidelity operations and greater sensitivities are possible by reducing the thermal occupation of relevant modes to below the Doppler limit, or even to the motional ground state. Of course, there are schemes that do not require such measures. Ground state cooling offers practical advantages to Doppler cooling - at the expense of some overhead - and also is a fundamentally interesting regime to work in, particularly so for large ensembles.

Though there are several methods for doing this, resolved sideband cooling is the traditional sub-Doppler cooling technique used in trapped ion systems. This method is well understood and, for small numbers of ions, it is straightforward to cool all motional modes to their ground state [44, 45]. The downside of resolved sideband cooling is that each mode must be individually addressed and

cooled. For a 100-ion crystal in a Penning trap, this means sequentially cooling 100 modes - if only one set of modes (say, the axial modes) are to be cooled. Clearly this is a hassle to implement. So, alternative sub-Doppler cooling methods are preferred.

Enter electromagnetically-induced transparency (EIT) cooling. Before getting into the details of what this technique is or how it works or is implemented, let's first consider its promise. The claim is that EIT cooling is a fast, broadband cooling method that can get an ion's motional mode(s) to its ground state. The hope, then, is that one could make use of EIT cooling to quickly and simultaneously cool all the axial modes of an ion crystal with hundreds of ions.

Originally proposed at the turn of the millennium [46, 47], EIT cooling was quickly demonstrated [48] and continued to prove useful for small systems [49, 50]. More recent work showcased the ability to simultaneously cool many modes to their groundstate in both 1D [51] and 2D (this work) [17] configurations. EIT cooling in 2D has recently been extended to RF trap systems with the use of a double-EIT scheme [52].

Electromagnetically-induced transparency, an effect also known by the name coherent population trapping [53], refers to a quantum interference phenomenon wherein destructive interference gives rise to optical transparency. That is, a dark state in which the system scatters no photons is produced. To achieve this effect, a 3-level atomic system and two lasers are required. Figure 6.1 (a) depicts a 3-level system with two ground states $|g_1\rangle$ and $|g_2\rangle$ and an excited state $|e\rangle$, as well as the two fields ω_1 and ω_2 that couple the lower states to the excited one.

Ignoring ion motion, the effect of the two laser fields is to cause the system to evolve into a dark state. The strong radiation field dresses the atomic states, and these dressed states experience a light shift $\delta = (\sqrt{\Omega^2 + \Delta^2} - \Delta)/2$, where $\Omega = \sqrt{\Omega_1^2 + \Omega_2^2}$ (Fig. 5.1 (a,b)). This effect will be considered more carefully in the following section, but the result is that the excitation amplitudes due to the two atom-photon couplings destructively interfere. With the addition of a weak probe laser, the absorption profile of the dressed atomic system can be visualized (Fig. 5.2). A broad resonance is centered on the dressed excited state $|-\rangle$, while a narrow Fano-shaped profile [53] is centered on the dressed virtual state $|+\rangle$ (which is at a frequency $\Delta + \delta$ higher relative to the
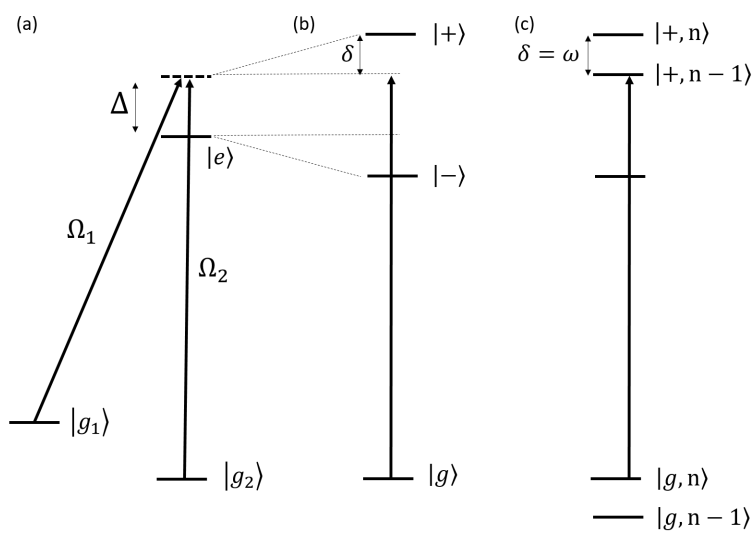
Figure 5.1: (a) Atomic 3-level scheme for EIT. Two ground states are coupled to an excited state via two lasers with shared detuning Δ from the excited state. (b) Dressed states experience a light shift δ. (c) With ion motion at frequency ω, sideband transitions may be driven.

undressed excited state). Meanwhile, at the detuning Δ there is a null in the absorption intensity: the atom will not absorb photons at this frequency.

Ion motion means absorption becomes possible at sidebands of the motional frequency: the ion can give up (receive) a motional quantum in exchange for receiving (giving up) a photon. Thus, if the light shift is set equal to the motional frequency $\delta = \omega_{\mathrm{com}}$ the motion-removing sideband will lie at the center of the Fano-shaped absorption peak. The motion-adding sideband, however, will see dramatically reduced absorption - and this asymmetry between the motion-removing and motion-adding sidebands is what gives rise to cooling. Figure 5.1 (c) illustrates this concept. The three relevant dressed states now are $|g, n\rangle$, $|+, n-1\rangle$, and $|g, n-1\rangle$. For the case where $\delta = \omega_{\mathrm{com}}$, the transition from $|g, n\rangle \rightarrow |+, n-1\rangle$, which results in the loss of a motional quanta n, is resonantly driven and subsequently spontaneously decays to $|g, n-1\rangle$. Note that the motion-removing sideband will lie on the absorption peak only for $\Delta > 0$, that is the lasers must be blue-detuned with respect to the excited state. Should $\Delta < 0$, heating rather than cooling will instead occur. To cool motional modes, the δk of the two lasers must be aligned along the same axis as the modes to be cooled.

5.2   Theoretical description

The theory for EIT cooling has been described in great detail in numerous places - here I will give just a brief overview of the relevant theory, following [47]. For a general and complete description see [46, 47], for an experimentalist's overview [49] and [51] cover this in different ways, and finally [43] gives a thorough treatment of the problem from the master equation, as well as relevant theoretical discussion for the experiment described here.

Given the three-level system already described and illustrated in Fig. 5.1, as well as the two laser fields with Rabi frequencies Ω_1 and Ω_2 (with $\Omega = \sqrt{\Omega_1^2 + \Omega_2^2}$) and shared detuning Δ (with $\Delta > 0$), the Hamiltonian for this system in the rotating frame is $H = H_0 + V_0$ where $H_0 = -\hbar \Delta(|g_1\rangle \langle g_1| + |g_2\rangle \langle g_2|)$ and $V_0 = \frac{\hbar}{2}\Delta(\Omega_1 |e\rangle \langle g_1| + \Omega_2 |e\rangle \langle g_2| + H.C.)$, which is due to interactions with the lasers. The system will evolve to a dark state - the superposition of the
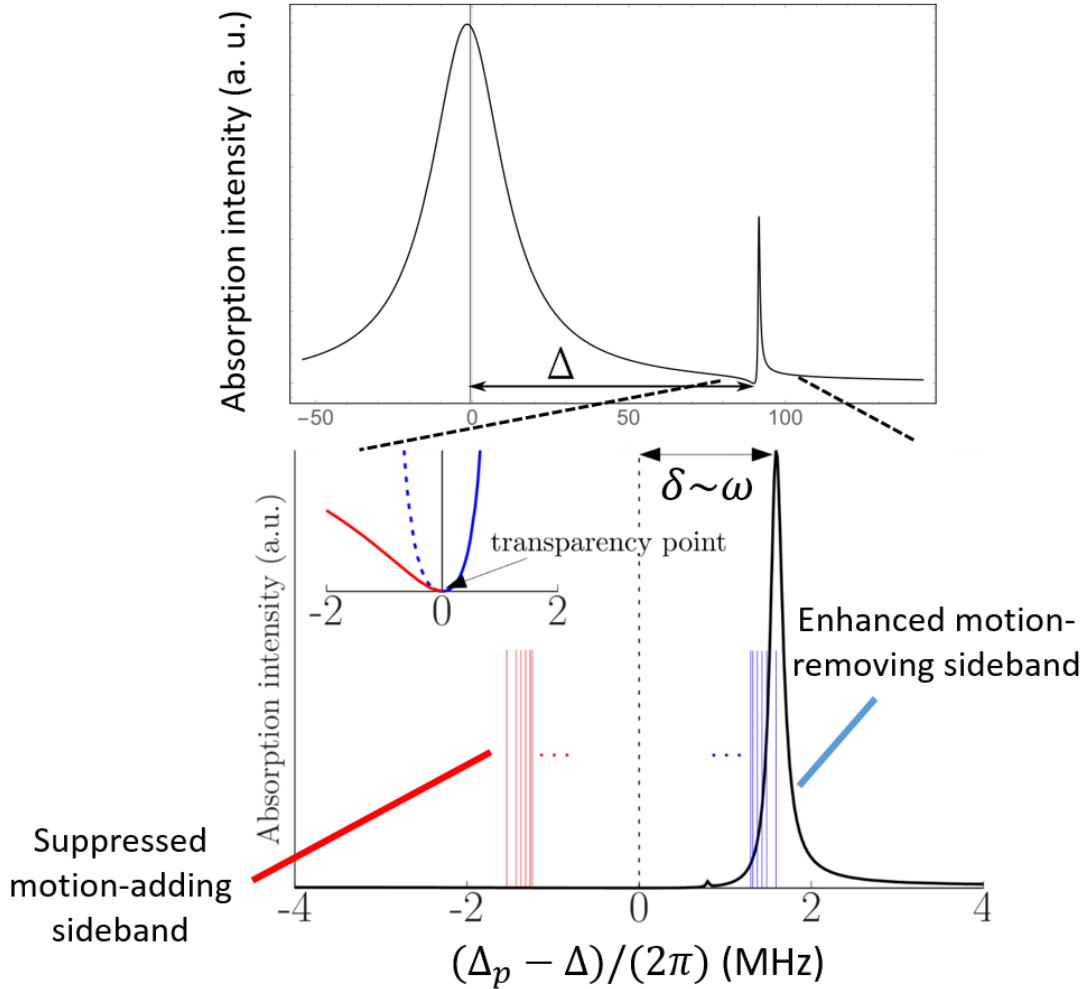
Figure 5.2: (a) Absorption intensity (in arbitrary units) for a weak laser probing the 3-level system in Fig. 5.1 [42]. The broad resonance is centered on the dressed excited state $|-\rangle$, while the dark state (where the absorption goes to zero) occurs at a frequency Δ above the excited state $|e\rangle$ (i.e. $\Delta + \delta$ above $|-\rangle$). The narrow Fano-profile is centered on the light-shifted dressed excited state $|+\rangle$. (b) Zooming in on the Fano-profile and the dark resonance illustrates the large asymmetry between the motion-removing and motion-adding sidebands [28]. Δ_p is the probe detuning from the excited state $|e\rangle$. Because the Fano-profile is broad compared to the bandwidth of modes to be cooled, setting $\delta = \omega_{\text{com}}$ is sufficient to cool all the axial modes.

two ground states decoupled from the excited state: $|\Psi_D\rangle = \frac{1}{\Omega}(\Omega_2 |g_1\rangle - \Omega_1 |g_2\rangle)$. This state is an eigenstate of H and, since it has no component of the excited state $|e\rangle$, is 'dark'. The two dressed states can be written as $|\Psi_+\rangle = \cos\theta |e\rangle + \sin\theta |\Psi_C\rangle$ and $|\Psi_-\rangle = \sin\theta |e\rangle + \cos\theta |\Psi_C\rangle$, where $\tan\theta = \frac{\sqrt{\Delta^2+\Omega^2}-\Delta}{\Omega}$ and $|\Psi_C\rangle = \frac{1}{\Omega}(\Omega_1 |g_1\rangle + \Omega_2 |g_2\rangle)$. The state $|\Psi_C\rangle$ is orthogonal to both $|\Psi_D\rangle$ and $|e\rangle$.

Thus, if $\delta = \omega$ where ω is the mode frequency to be cooled, the transition $|\Psi_D\rangle |n\rangle \to |\Psi_+\rangle |n-1\rangle$ will be driven. Since $|\Psi_+\rangle$ can decay back to the ground state and again back to $|\Psi_D\rangle |n-1\rangle$, this provides a cycling transition for cooling. The limit of the final phonon occupation is set by heating due to driving the (blue-sideband) transition $|\Psi_D\rangle |n\rangle \to |\Psi_-\rangle |n+1\rangle$, since the carrier transition is canceled (the ions remain in the dark state). The result is a cooling limit given by the mean final phonon occupation of the mode(s) satisfying the EIT cooling condition $\langle \bar{n}\rangle = \left(\frac{\gamma}{4\Delta}\right)^2$, where $\gamma = \gamma_1 + \gamma_2$ is the sum of the rates of decay from the excited state into the ground states $|g_1\rangle, |g_2\rangle$. Thus, larger detunings Δ result in lower mode occupation. The cooling rate has the same scaling with Δ, and is given by $W \sim \eta^2 \Omega^2/\gamma = \eta^2 4\omega(\omega + \Delta)/\gamma$ (where η is the Lamb-Dicke parameter) for the EIT cooling condition $\Omega^2 = 4\omega(\omega + \Delta)$ (from $\delta = \omega = (\sqrt{\Omega^2 + \Delta^2} - \Delta)/2$) [47].

5.3   Experimental challenges and setup

EIT cooling has been successfully demonstrated in several experiments, as described earlier. However, this work involved several challenges and novel solutions. In particular, theoretical modeling was performed to verify that EIT cooling would be effective for large ($N > 100$) 2D arrays of ions and to account for the rotation of the ion crystal [42]. Recall that the ions in the NIST Penning trap rotate at $w_r \approx 180$ kHz, which produces large Doppler shifts (hundreds of MHz) for ions at the edge of the crystal. The Doppler shift depends on the rotation speed, but also the ion number. Increasing the ion number and holding the rotation frequency fixed results in a crystal with larger radial extent and therefore increased Doppler shifts at the perimeter. As a result, the detuning Δ chosen must be sufficiently large to compensate for these Doppler shifts and prevent a substantial

number of ions from seeing $\Delta > 0$, which would cause heating. With this effect accounted for, theory predicted and experiment confirmed that EIT cooling will work in a Penning trap. The large number of ions actually turns out to be an advantage, as the EIT cooling rate scales favorably with the ion number due to quantum many-body effects [42, 17]. The scaling of the cooling rate with ion number was not investigated experimentally because controlling small numbers of ions (< 20) is challenging, and this is the regime where most of the change in the cooling rate is expected. This effect was not experimentally observed in recent work with large numbers of ions in an RF trap [52], however this may be due to an elevated heating rate caused by noisy electric fields that scales unfavorably with ion number.

To implement EIT cooling required several key experimental advances, to be detailed in this section. A challenge for EIT cooling in a Penning trap is the large Zeeman splitting of the ground state hyperfine levels that must be coupled to the excited state in the 3-level setup. Since Penning traps use strong magnetic fields, this splitting can be very large: in our system the 4.5 T magnetic field results in a 124 GHz splitting. This means that the two lasers that provide the EIT cooling must coherently span the 124 GHz frequency splitting. To span the 124 GHz frequency splitting between the two hyperfine ground state levels (Fig. 5.3), a phase lock between two diode lasers with an adjustable frequency offset was implemented. Setting the detunings and Rabi frequencies of the lasers accurately is crucial for getting cooling, and so control over the frequency and intensity of the light is required. The frequencies of these lasers was also stabilized absolutely by way of saturated absorption spectroscopy with Iodine. Additionally, two new beam paths were needed in order to deliver the laser light to the ions. The alignment of the EIT δk vector normal to the ion crystal array is critical and requires careful alignment of optics. To cool the axial modes of the ion crystal, we aligned the δk vector to $< 0.2°$.

To achieve the 124 GHz frequency offset lock, we use two Toptica systems (described in more detail in Sec. 3.3) based on an external-cavity diode laser with an infrared output that is subsequently doubled to 626 nm in a resonant second harmonic generation stage. This light will ultimately be doubled again to 313 nm via another cavity-enhanced SHG stage. By picking off
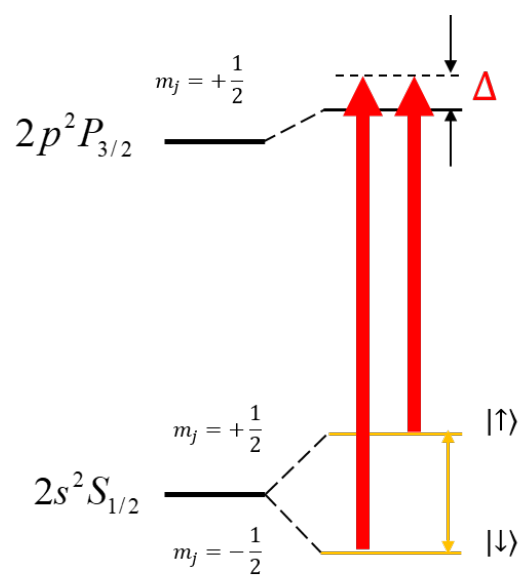
Figure 5.3: Level diagram of Be$^+$ in the 4.46 T magnetic field. The two EIT beams couple the two hyperfine levels of the ground state - which are separated by 124 GHz - to the excited state and are blue-detuned from this excited state by Δ.
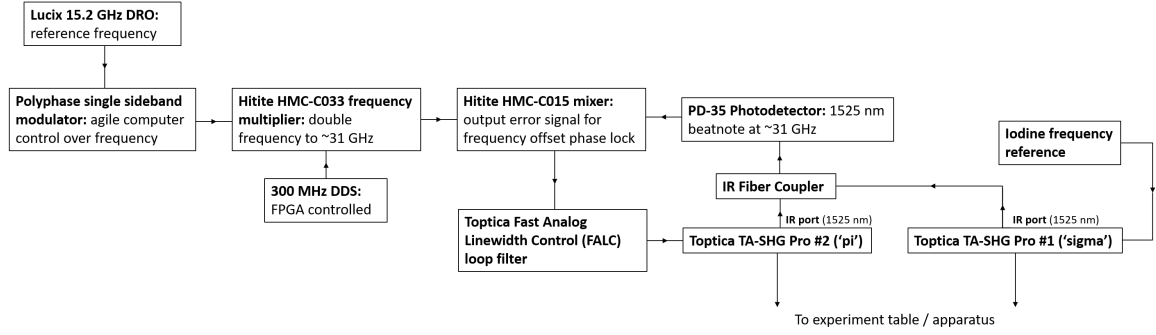
Figure 5.4: Schematic of microwave electronics for the 31 GHz frequency offset phase lock. A 31 GHz reference signal is mixed with an agile 300 MHz FPGA controlled DDS to allow for computer control of the frequency offset. This signal is mixed with the 31 GHz beatnote formed on a photodetector from the IR ports of the two Toptica lasers. The mixed down output is a phased error signal which is sent to the FALC loop filter unit, which sends feedback to the laser diode.

some of the infrared light of the two lasers, we can set up a phase lock with a frequency offset of 31 GHz (Fig. off-lock-schematic). The infrared light is coupled into a fiber coupler and fed into a 30 GHz photodiode. The output of the photodiode is mixed with a reference signal. The 31 GHz reference is produced by a frequency-doubled 15.2 GHz Dielectric Resonator Oscillator (DRO) which is mixed with 300 MHz from a computer-controlled DDS, which lets us control the precise offset frequency. The mixed down signal is sent to a Toptica Fast Analog Linewidth Control (FALC) PID. The PID output is connected to the DC coupled current modulation on the 'pi' Toptical laser's DL100 (i.e. directly to the diode). Additionally, we lock the frequency of one laser to an Iodine line via saturated absorption spectroscopy, the choice of which sets the detuning Δ from the excited state.

To align the EIT beams to the ions, we counterpropagate the two beams with respect to the ODF beams. Since we have established a very precise method for aligning the ODF beams such that their δk is along the axis of the trap (perpendicular to the plane of the ion crystal), we can simply overlap the EIT beams with the ODF beams. We do this over several meters of path length on either side of the trap and estimate that our alignment error with respect to the axis of the trap is $< 0.2°$. After performing this alignment we measure the ACSS and make very small adjustments to the beam alignment to maximize the ACSS, ensuring the beams are well centered on the ions.
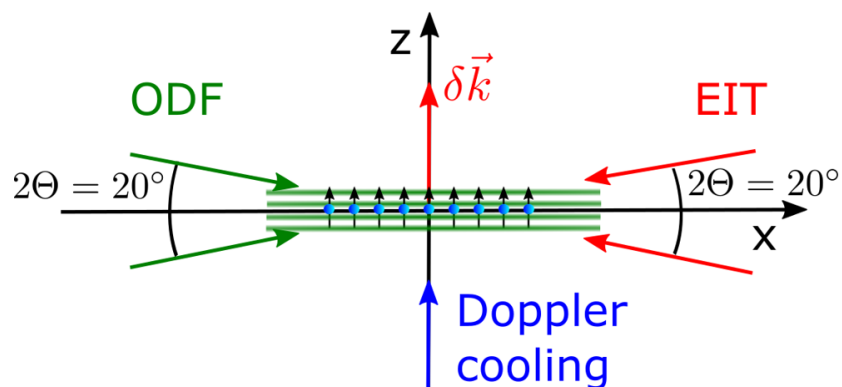
Figure 5.5: Schematic of laser setup for EIT cooling. The blue spheres represent the ions with their spins (arrows). The beams generating the spin-dependent optical-dipole force (ODF) (green) intersect in the plane of the ions with the EIT cooling beams (red) counter-propagating relative to the ODF beams. The ODF beams interfere at the position of the ions and form a traveling wave potential (green fringes).

Small changes to the angle seem to play an important role in getting the EIT cooling to work.

The lab procedure for setting the parameters will be outlined here. The offset lock frequency is controlled via DDS and can be precisely set by measuring the spin flip frequency in a Ramsey experiment and adjusting the frequency offset of the lock to match this. Based on the ion number and rotation frequency of the crystal, a detuning is selected that ensures that no ion sees a Doppler shift large enough to cause $\Delta < 0$. The detuning itself has not seemed terribly important, as long as the Rabi frequencies for the lasers and the chosen detuning satisfy the EIT cooling condition $\delta = \omega_{\mathrm{com}}$. The heating rate of the ions is negligible on the timescale of the EIT cooling, and so cooling faster doesn't provide an advantage. To set the Rabi frequencies, we measure the ACSS's for each beam and adjust the power individually to match the desired ACSS. In practice, in order to do this we had to substantially detune the lasers away - Δ of only 400 MHz with 50 MHz Rabi frequency meant it was impossible to measure ACSS. We then note the power for the correct ACSS while detuned, bring the laser back to the chosen detuning, and reset the power to the now known value. With Δ chosen and the laser powers set, we lock one laser to the appropriate Iodine line, then turn on the frequency offset phase lock to stabilize the second laser to the first.

5.4   Results

To quantify the efficacy of the EIT cooling, we perform sequential measurements of the COM mode occupation - as was outlined in Chapter 5 - with solely Doppler and then both Doppler and EIT cooling. For the sake of clarity, this mode occupation measurement will be briefly described here. The axial motion of the ions is coupled to their internal spin state via a spin-dependent optical-dipole force (ODF) produced by a traveling wave potential gradient from two interfering off-resonant lasers. This coupling is described by a Hamiltonian of the form $\hat{H} = F\cos(\mu_r t)\sum_{j=1}^{N}\hat{z}_j\hat{\sigma}_j^z$, where F is the ODF amplitude, and $\hat{z}_j$ and $\hat{\sigma}_j^z$ are the position operator and the Pauli spin matrix for ion j, respectively. The frequency of this spin-dependent force μ_r is tunable, and (with the collective spin vector on the equator of the Bloch sphere) when it matches the frequency of motion of the ion crystal spin precession occurs. This spin precession is mapped into spin population in a
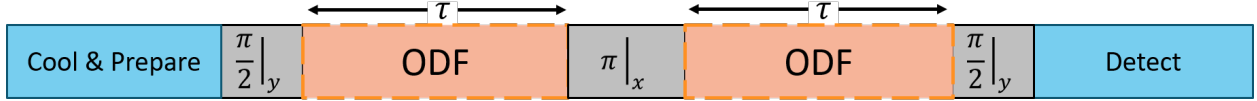
Figure 5.6: Experimental sequence used to make a measurement of the COM mode occupation with just Doppler cooling. The ions are Doppler cooling and then prepared in the $|\uparrow\rangle$ state. A microwave pi/2 pulse rotates the spins to the equator of the Bloch sphere. Application of the ODF allows for motion of the ion crystal at the ODF difference frequency μ_r to be mapped onto the spins. The ODF is applied for a variable time τ, depending on experimental parameters and the temperature of the mode. A microwave pi pulse in the middle of the sequence is used for dynamical decoupling. A final pi/2 pulse rotates the spins into the measurement basis, and the Doppler cooling laser is used for a projective measurement of the spin state.

Ramsey experiment. Figure 5.6 illustrates this procedure. The ions are prepared in the $|\uparrow\rangle$ state, a resonant microwave $\pi/2$ pulse rotates the spins around the y axis to align with the x axis, and the ODF produces spin precession for an interaction time of 2τ. Midway through the ODF interaction, the spin precession is interrupted by a π pulse, implementing a spin-echo. A final $\pi/2$ pulse is applied that brings the ions to the $|\downarrow\rangle$ state, if no dephasing occurred. Spin dephasing leads to a finite $|\uparrow\rangle$ state probability (which we refer to as the bright fraction), which we measure through state-dependent resonance fluorescence on the Doppler cooling transition. The method is described in detail in Ref. [37]. A subsequent experiment is then preformed, with exactly the same sequence as was just described - except now EIT cooling will be applying following the Doppler cooling (see Figure 5.7). By fitting to the data, we can extract the mode occupation for the COM mode for both cases and verify that EIT cooling surpasses the Doppler cooling limit.

Figure 5.8 shows measurements of the bright fraction as the ODF difference frequency μ_r is stepped across the COM mode frequency ω_{COM}. The decrease in the bright fraction observed when

Figure 5.7: This is the same sequence as Fig. 5.6, but now with a variable amount of EIT cooling following the Doppler cooling but prior to state preparation.

Doppler cooling is followed by EIT cooling indicates a decrease in dephasing due to the lower COM mode occupation. To extract the mean COM mode occupation $\bar{n}$, we fit to an analytical expression for the $|\uparrow\rangle$ state probability

$$P(|\uparrow\rangle) = \frac{1}{2}\left[1 - \exp\left(-2\Gamma\tau\right)C_{\text{ss}}C_{\text{sm}}\right], \tag{5.1}$$

where the coefficients $C_{\text{ss}} = (\cos 4J)^{N-1}$ and $C_{\text{sm}} = \exp\left(-2|\alpha|^2(2\bar{n}+1)\right)$ describe the phonon-mediated spin-spin interaction, and the dephasing that arises from spin-motion coupling, respectively. Here, N is the number of Be^+ ions and 2τ is the total ODF interaction time. The spin-dependent displacement amplitude α and spin-spin coupling J are functions of τ, the spin-echo π-pulse duration t_π, the optical dipole force amplitude F and the frequencies μ_r and ω_{COM}.

Figure 5.8 also shows least-squares fits of Eq. (5.1) to the experimental measurements where ω_{COM} and $\bar{n}$ are free parameters. All other parameters are empirically measured. As was described in Chapter 5, the magnitude of the spin-dependent optical dipole force F is measured experimentally via a mean-field spin precession experiment[13]. Likewise, the decoherence rate Γ is independently calibrated and compared to theory. This spin decoherence is primarily due to photon scattering, but contributions due to the finite Lamb-Dicke parameter are also present.

From Eq. (5.1) and Fig. 5.6, the observed signal will include both a temperature-dependent spin-motion component (C_{sm}) and a spin-spin component (C_{ss}) that does not depend on the temperature. Thus, measurements after only Doppler cooling are dominated by motion-induced dephasing, while for the EIT cooling measurements the spin-spin component dominates. Note that the contributions from both the spin-spin and zero-point motion are never zero, and thus the lineshape for the COM mode cooled to its motional ground state $\bar{n} = 0$ is not identically zero.

After EIT cooling we obtain consistent measurements of $\bar{n} = 0.11 \pm 0.18$, demonstrating near ground state cooling for the COM mode with greater than 100 ions. For Doppler cooling only, occupancies of $\bar{n} = 4.6 \pm 0.2$ are obtained, consistent with the Doppler cooling limit.

To determine a cooling rate for the COM mode, we measured the COM mode occupation $\bar{n}$ for increasing durations of EIT cooling (Fig. 5.9). The measured cooling rate is well described by
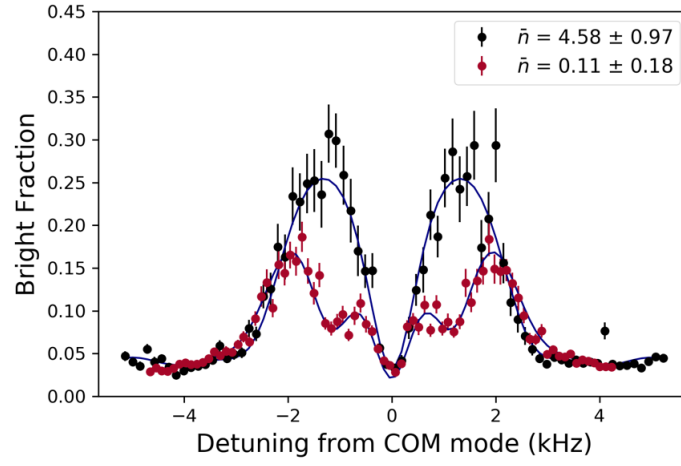
Figure 5.8: Temperature measurement of the COM mode at frequency $\omega_{\mathrm{COM}} = 2\pi \times 1.59$ MHz for a crystal with 158±10 ions. The black dots are the measured fraction of ions in the $|\uparrow\rangle$ state after Doppler cooling only, and the red dots after Doppler cooling followed by 200 µs of EIT cooling. The solid lines are least squares fits of Eq. (5.1) to the data. The ODF interaction time was $2\tau = 500$ µs. The fitted mean COM mode occupations are $\bar{n}_{\mathrm{Dop}} = 4.6 \pm 1.1$ after Doppler cooling only and $\bar{n}_{\mathrm{EIT}} = 0.11 \pm 0.18$ after EIT cooling.

an exponential with $1/e$ time of $\tau_{\text{cool}} = 27.6 \pm 1.7$ μs. The measured heating of the COM mode is negligible on this time scale (see Chapter 5).

This measured cooling rate is faster than the average rate expected from N independently cooled ions (blue curve in Fig. 5.9). This observation is consistent with detailed numerical simulations of EIT cooling with smaller crystals, where the cooling rate of the COM mode is found to increase with N [42]. The simulations also reproduce the experimentally observed initial heating during the first few microseconds, which is caused by transient internal transitions until the ions reach the approximate dark state.

5.5   Summary and outlook

As was discussed previously, a main appeal of EIT cooling is the broad frequency bandwidth over which it can effectively cool modes simultaneously. This is particularly useful for large systems with many modes, or for systems with unresolved modes. In the case of the Penning trap experiment, there are many drumhead modes ($\sim$N, where $N > 100$ is the number of ions in the crystal) most of which are not resolvable. Thus, EIT cooling is an appealing choice for sub-Doppler cooling.

We verified experimentally that the bandwidth of the cooling - given our choice of parameters - was sufficient to effectively cool all the axial drumhead modes. Figure 5.10 shows spin-dephasing measurements for after only Doppler cooling and after both Doppler and EIT cooling. This experiment is performed in the same manner as described earlier in this chapter, except now the range over which μ_r is scanned covers all the axial modes. This experiment demonstrates that all axial modes may be sub-Doppler cooled simultaneously - that is, with a single application of EIT cooling and no changing of parameters. Each data point in Fig. 5.10 represents the exact same experiment being carried out, except that μ_r is being varied. However, we are not able to extract the mode occupation for any given mode, primarily because the modes are not resolvable but also because theory comparisons have been challenging. As a result, we can qualitatively state that a single application of EIT cooling cools all axial modes below the Doppler limit.
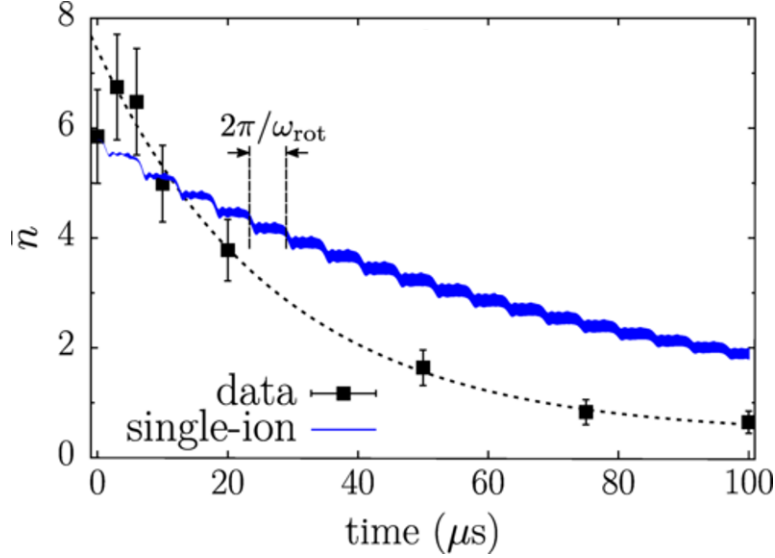
Figure 5.9: EIT cooling transient for the COM mode of a crystal with $N = 190 \pm 10$ ions. The mean occupation of the COM mode $\bar{n}$ is plotted versus the EIT cooling time. The black dotted line is an exponential fit to the data. The blue curve shows the average cooling transient computed for single ions. To approximately incorporate the radial crystal structure, we compute single-ion transients for each distance in the crystal from the trap center, and then average by weighting each transient by the number of ions at that radius. The thickness of the curve accounts for a 10% uncertainty in the powers of the EIT lasers.
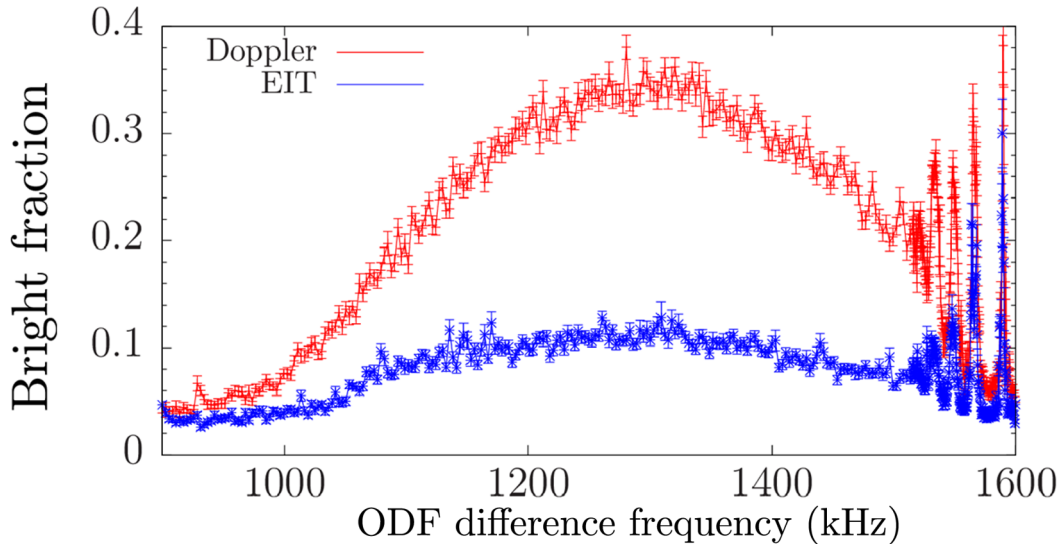
Figure 5.10: Scan over all the axial drumhead modes. The red points are data taken with Doppler cooling, blue points are data after Doppler and 200 μs of EIT cooling for a crystal with 158 ± 10 ions. The significant reduction in the amplitude indicates a lower temperature for all of the modes.

Though we cannot state quantitatively the mode occupation for the (unresolvable) lower frequency modes, we observe that they are substantially cooled beyond the Doppler limit. Comparison to theory is challenging, as our theoretical understanding of the axial mode structure at the time of this study suggested that the modes should be well-resolved - obviously this is not the case. However, by assuming drumhead mode frequency fluctuations that linearly increase from 1 kHz for the highest frequency tilt mode to more than 10 kHz for the lower frequency drumhead mode, it was possible to obtain qualitative agreement with the EIT cooling signal of FIg. 5.10. With this assumption, the experimental results are consistent with near ground state cooling of all the drumhead modes. Recent theoretical work [43, 28] suggests that the apparent frequency instability of the axial modes stems from in-plane mode temperatures significantly above the Doppler cooling limit with $E \times B$ mode temperatures on the order of 10 mK sufficient. This frequency instability has the effect of blurring the axial modes, and made comparing experimental data to theory challenging. As a result, the main conclusion for the efficacy of EIT cooling over all the axial modes is that qualitatively it successfully cools all axial modes (to a similar degree) to well below the Doppler limit and to a mode occupation that is consistent with being near ground state cooled.

An outstanding challenge to implementing EIT cooling on a day-to-day basis is the sensitivity of the cooling to alignment. At times, with poor alignment apparent rapid heating of the ions was observed. Though this issue is straightforwardly mitigated by improving the overlap with the ODF beams, it is not currently known what the impact of small misalignments of the EIT δk vector on the in-plane modes might be. Since there is no direct experimental diagnostic of in-plane mode temperature and an elevated in-plane mode temperature may give rise to frequency fluctuations of the axial drumhead modes, experiments sensitive to frequency fluctuations of the COM mode must take this into account. Preliminary experimental results indicate that EIT cooling may lead to an increased instability of the COM mode frequency (see Ch. 7). Improved alignment or the use of three-dimensional crystals (see Ch. 8) may mitigate this effect.

Successful demonstration of near-groundstate cooling of the ion crystal can directly lead to future experimental improvements. As a result of the reduced axial mode occupation, the effective

wavelength of the optical lattice which produces the ODF can be reduced while remaining in the Lamb-Dicke confinement regime. By increasing the angle of incidence of the ODF relative to the plane of the ions (i.e. increasing δk), the amplitude of the resulting spin-dependent force is increased. Since the ratio of the spin-dependent force relative to the photon scattering rate is a fundamental limit for this apparatus, such an increase would be a significant boon to future quantum simulation and sensing projects. Additionally, the COM mode occupation $\bar{n}_{COM}$ is also a direct limitation to experiments concerned with sensing small electric fields resonant with the COM mode and their subsequent displacements of the mode (7).

Chapter 6

Off-resonant amplitude sensing

This chapter constitutes some of the primary results of the thesis: the sensing of center-of-mass displacements of a 2D crystal of ions. Here I will give an overview of the set of experiments performed and detail both the experimental and theoretical work. The work described here was published [18, 19], and builds on earlier results [37, 12, 54].

6.1   Overview

In this chapter we experimentally and theoretically analyze a technique to measure the center-of-mass (COM) motion of a two-dimensional, trapped-ion crystal of $\sim$100 ions with a sensitivity smaller than z_{ZPT}, the amplitude of the zero-point motion defined as $z_{ZPT} = \frac{1}{\sqrt{N}} \sqrt{\frac{\hbar}{2m\omega_z}} \approx 2 \, \text{nm}$. Measuring the amplitude of mechanical oscillators has engaged physicists for more than 50 years [55, 56] and has produced exciting advances both in fundamental physics and in applied work. From large scale gravitational wave detectors [57], to mesoscopic optomechanical resonators [58, 59, 60, 61, 62], to small scale single-ion sensors [63, 64, 65, 66, 67], new avenues of fundamental and applied physics have been opened as the limits of amplitude sensing have improved. Outside of the practical applications of better sensors, the limits to which a displacement smaller than the ground state wave function can be determined in a single measurement is of fundamental interest in quantum metrology. Experiments are now routinely able to measure displacements smaller than the zero-point motion [62, 59, 64, 66, 18, 19].

Ions trapped in a harmonic potential are a natural platform to explore the fundamental limits

of amplitude sensing. Crystals of laser-cooled, trapped ions behave as atomic-scale mechanical oscillators [68, 54, 37] with tunable oscillator modes and high quality factors ($\sim 10^6$). Furthermore, laser cooling enables ground-state cooling and non-thermal state generation of these oscillators. Measurements of weakly driven coherent amplitudes, both smaller and larger than the zero-point fluctuations, have been demonstrated in traps with very small numbers of ions [64, 65, 66, 69, 67], but few sensing experiments have been conducted on larger trapped-ion crystals [54, 18, 19]. Larger ion crystals have the benefit of reduced spin-projection noise, improving the sensitivity for detecting weak electric fields.

For the work described in this chapter, the COM motion is excited off-resonantly, i.e. is driven at a frequency far from the motional modes. We employ a time-varying spin-dependent force $F_0 \cos(\mu t)$ that couples the amplitude of the COM motion with the internal spin degree of freedom of the ions [11, 12]. When the frequency μ matches the frequency ω of a driven COM oscillation, $Z_c \cos(\omega t)$, spin precession proportional to Z_c occurs. This amplitude-dependent spin precession is analogous to the optomechanical frequency shift of a cavity mode [58]. In contrast to the continuous measurement typical of optomechanics experiments, we measure the spin precession only at the end of the experimental sequence, with a precision imposed by spin projection noise [70] and photon scattering [35].

In what follows, the basic protocol will be outlined, as well as general details regarding the experimental sequences used. Two main results will be described in this chapter: a set of experiments performed without control of the relative phase between the ODF and the classical drive and another set of experiments with this phase controlled. The work here is concerned with measurements of classical COM motion far from resonance with the COM mode itself. This provides a fundamental limit to the amplitude sensitivity - the measurement imprecision - in a regime free from thermal, zero-point, or frequency noise associated with the COM mode.

6.2   Basic protocol and review of spin-motion coupling

The apparatus used for these measurements was described in Ch. 3, the Hamiltonian generated with the spin-dependent ODF in Ch. 2.4, and the generic experimental sequence in Ch. 4. In short, a pair of laser beams, detuned from the nearest optical transitions by $\sim$20 GHz, interfere to form a one-dimensional (1D) traveling-wave potential that produces a spin-dependent optical-dipole force (ODF). Optical pumping prepares the initial state $|\uparrow\rangle_N \equiv |\uparrow\uparrow \cdots \uparrow\rangle$ with high fidelity. At the end of the experiment we measure the probability $P_\uparrow$ for an ion spin to be in $|\uparrow\rangle$ from a global measurement of state-dependent resonance fluorescence on the Doppler cooling transition, where spin $|\uparrow\rangle$ ($|\downarrow\rangle$) is bright (dark).

If the ions are localized axially over an extent small compared with the wavelength of the 1D traveling-wave potential (Lamb-Dicke confinement), then the ODF couples the spin and motional degrees of freedom through the interaction (see Sec. 6.3 for more details)

$$\hat{H}_{ODF} = F_0 \cos\left(\mu t\right) \sum_i \hat{z}_i \hat{\sigma}_i^z. \tag{6.1}$$

Here $F_0 = U \, \delta k \, DWF$ is the magnitude of the ODF, where U (δk) is the zero-to-peak potential (wave vector) of the 1D traveling-wave, μ is the frequency difference between the ODF beams, and $\hat{z}_i$ and $\hat{\sigma}_i^z$ are the position operator and Pauli spin matrix for ion i. The Debye-Waller factor $DWF = \exp(-\delta k^2 \left\langle \hat{z}_i^2 \right\rangle /2)$ reduces F_0 due to the departure from the Lamb-Dicke confinement regime [29]. For this work, the Debye-Waller factor depends on whether only Doppler cooling was used, as in Sec. 6.4 where $DWF \approx 0.86$, or supplemental EIT cooling was used as well, as in Sec. 6.5 where $DWF \approx 0.92$. The potential U, and therefore F_0, is determined from two independent calibrations: measurement of the AC Stark shifts on the ions and the meanfield precession of the spins (see Ch. 4 and [13]), which agree to within 5%. Typical maximum values for this work range from $(U/\hbar)/(2\pi) \simeq 10.4$ - 22.88 kHz resulting in $F_0 \simeq 40$ - 88 yN.

Equation (6.1) describes a dependence of the spin transition frequency on the axial position of the ions and the ODF frequency μ. We excite a small, classically driven COM motion of constant amplitude $\hat{z}_i \to \hat{z}_i + Z_c \cos(\omega t + \delta)$ with a weak RF drive on a trap endcap electrode (see Fig. 6.1)
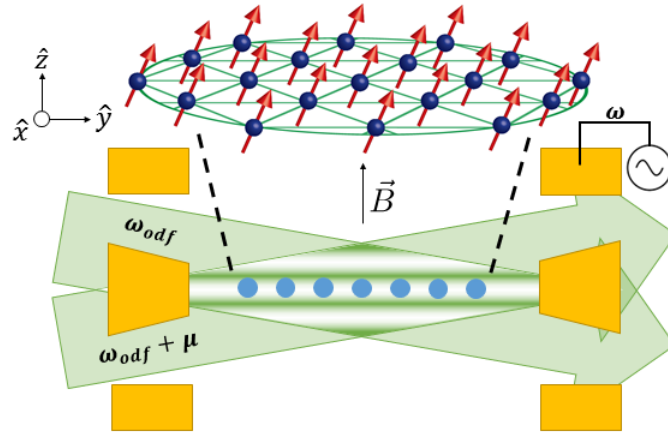
Figure 6.1: Representation of ion spins arranged in a 2D triangular lattice, along with a cross-sectional illustration of the Penning trap, characterized by an axial magnetic field $B = 4.45$ T and an axial trap frequency $\omega_z = 2\pi \times 1.57$ MHz. The blue dots represent ions. Cylindrical electrodes (yellow) generate a harmonic confining potential along the $\hat{z}$-axis. Radial confinement is provided by the Lorentz force from $\vec{E} \times \vec{B}$-induced rotation in the axial magnetic field. The beams generating the spin-dependent optical-dipole force (green arrows) cross the ion plane at $\pm 10°$, forming a 1D traveling-wave potential (green lines) with $\delta k = 2\pi/(0.9\,\mu\text{m})$. An AC voltage source is connected to the trap endcap and used to drive an axial oscillation with calibrated amplitude Z_c.
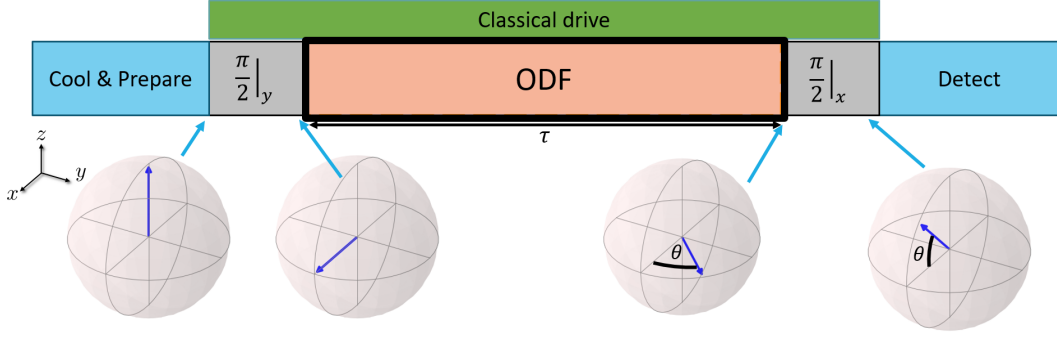
Figure 6.2: Illustration of a Ramsey sequence with a 90 degree phase shift between the initial and final $\pi/2$ pulses. This sequence is first order (linearly) sensitive to rotations θ in the x-y plane of the Bloch sphere.

at a frequency ω far from ω_z. Here, δ is the relative phase between the ODF and the classical drive. If $\omega \sim \mu$, Eq. (6.1) produces an approximately constant shift in the spin transition frequency. With $\delta k Z_c \ll 1$, this shift is given by

$$\hat{H}_{ODF} \approx F_0 \, Z_c \cos((\omega - \mu)t + \delta) \sum_i \frac{\hat{\sigma}_i^z}{2}. \tag{6.2}$$

For $\mu = \omega$, the static shift of the spin transition frequency is simply $\Delta(Z_c) = (F_0/\hbar) \, Z_c \cos(\delta)$.

We measure $\Delta(Z_c)$ from the resulting spin precession in an experiment like that shown in Figs. 6.2 and 6.3. Ideally, spin precession can be measured using a Ramsey-type experiment. First, the ions are prepared in the $|\uparrow\rangle_N$ state, followed by a microwave $\pi/2$ pulse about $\hat{y}$ that rotates the spins to the $\hat{x}$ axis. The spins precess for an interaction time τ so that the resulting spin precession on resonance ($\mu = \omega$) is $\theta = \theta_{max} \cos(\delta)$, where $\theta_{max} \equiv (F_0/\hbar) \, Z_c \, \tau$. After a final $\pi/2$ pulse about either $\hat{y}$ or $\hat{x}$, the final state readout measures the population of the spins in $|\uparrow\rangle$. Here Γ is the decay rate from photon scattering from the off-resonant ODF laser beams [35]. To detect small amplitudes with the available F_0 in our set-up, we extend the spin-precession time to $\tau \geq 20$ ms and $\tau \geq 8$ ms for the experiments in Secs. 6.4 and 6.5, respectively. To avoid decoherence due to magnetic field fluctuations and coherently accumulate spin precession, we use a quantum lock-in [71] sequence where during the interaction time τ the spin precession is interrupted by a train of π-pulses that are synchronized with phase jumps enforced on the ODF beams (see next section).

The choice of final axis for the final $\pi/2$ pulse in this Ramsey sequence depends on the type
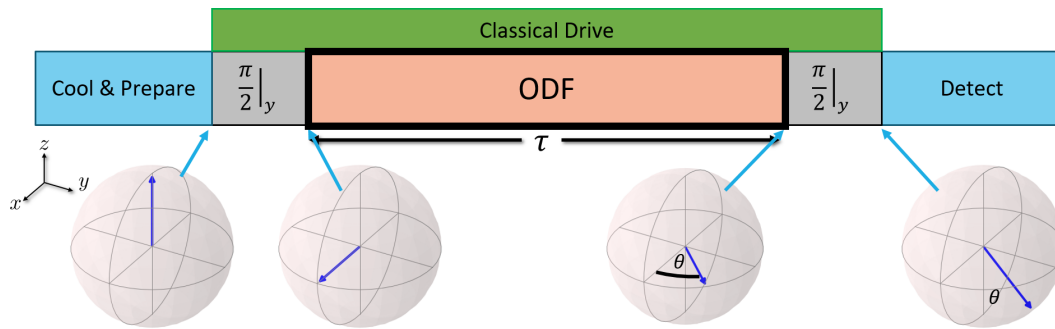
Figure 6.3: Illustration of a Ramsey sequence with the initial and final $\pi/2$ pulses having the same phase. This sequence is second order (quadratically) sensitive to rotations θ in the x-y plane of the Bloch sphere.
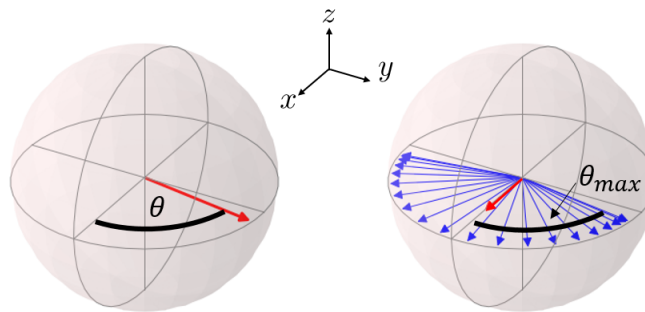
Figure 6.4: The stability of the relative phase between the ODF and the classical drive impacts the shot-to-shot angle of precession θ. On the left, a consistent coherent rotation (θ) of the collective Bloch vector (red arrow) is possible from shot-to-shot if the relative phase is well stabilized. On the right, shot-to-shot variation of the relative phase results in random amounts of spin precession with each shot of the experiment. The blue arrows represent different realizations of the experiment each with a random relative phase. Though $\theta_{\max} = \theta$, where θ represents the maximum coherent rotation, the average rotation is zero. As a result, the measurable signal is effectively a reduction in the Bloch vector (red arrow).

of signal being measured. Figure 6.2, which uses a $\pi/2$ about $\hat{x}$ for its final spin rotation, is linearly sensitive to θ and thus also displacements of the ion crystal. The rotation θ is directly mapped to populations. However, if the angle of rotation varies randomly from shot-to-shot (see Figs. 6.4 and 6.3) this sequence is not ideal. In this case, the average value of the rotation is zero, and the average collective Bloch vector would remain on the equator of the Bloch sphere. Though the noise in the measurement would increase and could be measured, instead the collective Bloch vector is rotated down after the accumulated spin precession with a $\pi/2$ about $\hat{y}$. In this case, the signal is effectively a reduction in the length of the (averaged) Bloch vector due to the spin dephasing from shot-to-shot. Though this approach suffers compared to the first method in that the signal is now second-order sensitive to θ, it is useful in the case where the phase of the driving field to be measured is unknown or uncontrolled. An advantage, however, of this quadratic protocol is that - for small angles of precession - the projection noise in the measurement is greatly reduced relative to the linear protocol, which (ending with the Bloch vector near the equator of the Bloch sphere) has near maximal projection noise.

6.3   Quantum lock-in and Hamiltonian with classical excitation

In the prior section, Eqs. 6.1 and 6.2 were given as the relevant Hamiltonians. However, some key assumptions must be made to arrive at these equations, and in fact these assumptions break down in the regime studied in this chapter. Importantly, another term in the Hamiltonian should be included when $\mu \leq U/\hbar$ and for this work becomes relevant when $\mu \approx 400$ kHz or less. This section will outline the basic protocol for canceling this unwanted term in the ODF Hamiltonian, which is achieved by periodically advancing the phase of the ODF in what has been elsewhere termed a quantum lock-in sequence [71]. An additional benefit of performing this periodic phase advance of the ODF is that it allows for straightforwardly implementing dynamical decoupling. To achieve the maximum sensitivity, the total interaction time τ should be extended as long as possible. However, magnetic field fluctuations limit the coherence of the qubit. To mitigate this, shorter free evolution periods of time T separated by qubit rotations can be used, where noise at
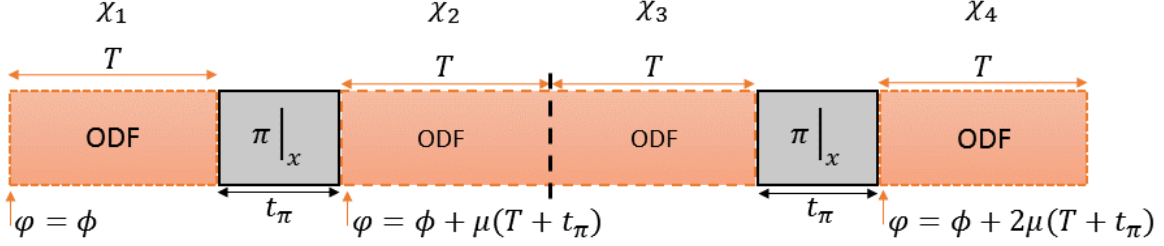
Figure 6.5: $m = 2$ CPMG sequence with total ODF interaction time $4T$. φ is the phase of the ODF beatnote. The χ_i labels represent the periods over which the accumulated phase is considered in the text.

frequencies below T^{-1} is suppressed.

In what follows, we consider the relevant ODF Hamiltonian for the case that $\mu \leq U/\hbar$. The interaction of the spin degree of freedom with the 1D traveling-wave potential is

$$\hat{H}_{ODF} = U \sum_i \sin(\delta k \cdot \hat{z}_i - \mu t - \phi)\hat{\sigma}_i^z$$

$$= U \sum_i \sin(\delta k \cdot \hat{z}_i) \cos(\mu t + \phi)\hat{\sigma}_i^z - U \sum_i \cos(\delta k \cdot \hat{z}_i) \sin(\mu t + \phi)\hat{\sigma}_i^z. \tag{6.3}$$

Here we explicitly include a phase ϕ for the traveling-wave potential. If $\delta k \langle \hat{z}_i \rangle \ll 1$, then $\langle \cos(\delta k \cdot \hat{z}_i) \rangle \sim 1$, and the spin precession due to the second term will be bounded by $(U/\hbar)/\mu$.

Typically, $(U/\hbar)/\mu \ll 1$ and thus this term is ignored in most treatments. However, at low frequencies $\mu \leq U/\hbar$ this term becomes important, but it can be canceled by advancing the phase of the ODF by $\Delta\phi = \mu(T + t_\pi)$ at each microwave $\pi-$pulse of the sequence (see Fig. 6.5, also Fig. 6.6). For the first iteration of this experiment (described in Sec. 6.4), an extended version of the Carr-Purcell-Meiboom-Gill (CPMG) sequence depicted in Fig. 6.5 was used. However, in subsequent experiments (Sec. 6.5), a short delay between setting the ODF phase and start of the sequence t_d was discovered. With the phase-incoherent protocol, this delay led to a negligible contribution to the background, and was therefore neglected. As a result, a CPMG sequence was appropriate to use. However, the phase-coherent protocol discussed in Sec. 6.5 is more sensitive, and so t_d cannot be ignored. As a result, it was found that a Periodic Dynamical Decoupling (PDD) sequence was superior in that it allowed for better cancellation of the unwanted background term.
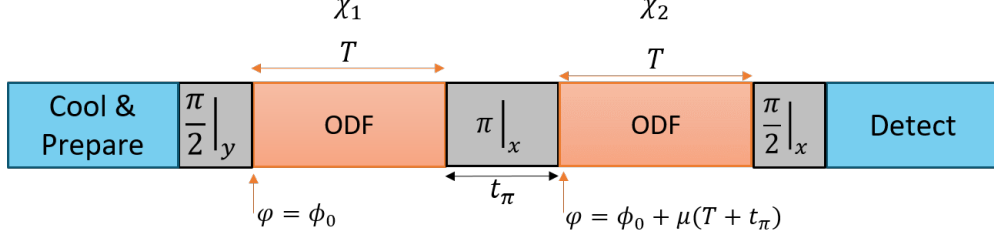
Figure 6.6: Illustration of spin echo sequence - the simplest version of the PDD scheme, with only a single π pulse. The final $\pi/2$ pulse is about the x-axis.

For simplicity, we derive this cancellation for the simple spin-echo sequence shown in Fig. 6.6, but this derivation holds for sequences with an odd number of π-pulses. The total spin-precession accumulated from this background interaction is

$$
\begin{aligned}
\theta_{\text{bck}} = &-\frac{U}{\hbar} \int_{t_0}^{t_1} \sin(\mu t + \phi_0) dt \\
&+ \frac{U}{\hbar} \int_{t_2}^{t_3} \sin(\mu t + \phi_0 - \Delta\phi) dt,
\end{aligned}
\tag{6.4}
$$

where $t_0 = t_d$, $t_1 = T$, $t_2 = T + t_\pi + t_d$, and $t_3 = 2T + t_\pi$ are the times at which the ODF lasers are turned off/on, and t_d is a delay between setting the ODF phase and the start of the sequence. The resulting spin-precession is then

$$
\begin{aligned}
\theta_{\text{bck}} = \frac{U}{\mu\hbar} \{ &\cos[\mu T + \phi_0] - \cos[\mu t_d + \phi_0] \\
&+ \cos[\mu(T + t_\pi + t_d) + \phi_0 - \Delta\phi] \\
&- \cos[\mu(2T + t_\pi) + \phi_0 - \Delta\phi] \}.
\end{aligned}
\tag{6.5}
$$

By applying a phase advance $\Delta\phi = \mu(T + t_\pi)$, all of the terms in Eq. (6.5) cancel, and therefore, this background interaction is removed for arbitrary μ. This analysis holds for sequences with an odd number of π-pulses, and with a phase advance $\Delta\phi = \mu(T + t_\pi)$ after each π-pulse.

To maintain the spin-motion interaction of Eq. 6.3 under this phase advance, the classical drive must be applied at a particular frequency or the duration of the experiment must be tuned. Specifically, we set

$$
\frac{\omega}{2\pi} = \frac{2n + 1}{2(T + t_\pi)}
\tag{6.6}
$$

for some integer n, which for the work discussed here is approximately $400\,\mathrm{kHz}$. Then when $\mu = \omega$, $\Delta\phi = \pi$ and the quantum lock-in phase advance of Ref. [71] is recovered, accumulating spin-precession from the first term of Eq. 6.3. The term that survives our modulation scheme is

$$\hat{H}_{ODF} \simeq U \sum_i \sin(\delta k \cdot \hat{z}_i) \cos(\mu t + \phi) \hat{\sigma}_i^z. \tag{6.7}$$

We now impose a weak, classically driven COM motion of constant amplitude and phase $\hat{z}_i \to \hat{z}_i + Z_c \cos(\omega t + \delta)$. This can be thought of as the center of the Penning trap being moved by $\pm Z_c$ at a frequency ω far from the trap axial frequency ω_z. With $\delta k\, Z_c \ll 1$, we obtain

$$\hat{H}_{ODF} \simeq U \sum_i \left(\delta k\, Z_c \cos(\delta k \cdot \hat{z}_i) \cos(\omega t + \delta) \cos(\mu t + \phi) + \sin(\delta k \cdot \hat{z}_i) \cos(\mu t + \phi) \right) \hat{\sigma}_i^z. \tag{6.8}$$

The second term of Eq. (6.8) is the usual term that gives rise to spin-motion entanglement with the drumhead modes and to effective spin-spin interactions [13, 14]. We assume we can neglect this term because we tune μ far from any drumhead modes.

Deep in the Lamb-Dicke confinement regime, the $\cos(\delta k \cdot \hat{z}_i)$ factor in the first term of Eq. (6.8) equals one. Here we account for the possibility of not being deep in the Lamb-Dicke confinement regime. In this case, and assuming a thermal distribution of modes, $\langle \cos(\delta k \cdot \hat{z}_i) \rangle = \exp(-\delta k^2 \langle \hat{z}_i^2 \rangle /2)$. This factor is known as the Debye-Waller factor DWF. For our conditions all ions have approximately the same Debye-Waller factor, $DWF \approx 0.86$ [14].

With $\mu \sim \omega$, Eq. (6.8) can be written as

$$\hat{H}_{ODF} = (U \cdot \delta k \cdot DWF)\, Z_c \cos((\omega - \mu)t + \delta - \phi) \sum_i \frac{\hat{\sigma}_i^z}{2}, \tag{6.9}$$

which is Eq. (6.2) with $F_0 = U \cdot \delta k \cdot DWF$.

6.4   Off-resonance, phase-incoherent sensing

To begin the process of characterizing the limits of sensing small displacement amplitudes with the 2D crystal of ions, we perform measurements where ω is far from resonance with the trap axial frequency ω_z. This allows us to determine the read-out imprecision in a regime free from

thermal noise associated with any of the motional modes. Thus, we can calibrate what the smallest detectable displacement is.

Additionally, we implement a protocol where the phase of the measured quadrature randomly varies from one iteration of the experiment to the next. This random phase arises as a result of an experimental limitation: we could not control the optical phase of the ODF relative to the phase of the classical driving field. However, this technique is appropriate for sensing a force whose phase is unknown or not stable. For $N = 85$ ions and $z_{ZPT} \equiv \frac{1}{\sqrt{N}} \sqrt{\frac{\hbar}{2m\omega_z}} \approx 2$ nm, we detect amplitudes $Z_c = 500$ pm in a single implementation of the experimental sequence, and as small as 50 pm after averaging over 3,000 iterations of the sequence.

We allow the phase δ to randomly vary from one iteration of the sequence to the next, effectively measuring a random quadrature of the motion for each experimental trial. Different experimental trials therefore result in a different precession θ, as indicated in Fig. 6.4. We measure the collective dephasing (or decoherence) averaged over many experimental trials $\langle P_\uparrow \rangle = \frac{1}{2}[1 - e^{-\Gamma\tau} \langle \cos(\theta) \rangle]$. Here the brackets $\langle \cdot \rangle$ denote an average over many iterations of the sequence. Averaging over the random phase δ yields

$$\langle P_\uparrow \rangle = \frac{1}{2} \left[1 - e^{-\Gamma\tau} J_0(\theta_{\max}) \right], \tag{6.10}$$

with J_0 the zeroth-order Bessel function of the first kind.

For this work, we use a Carr-Purcell-Meiboom-Gill (CPMG) sequence with $m = 8$ ODF-π-ODF segments ($\tau = 2\,m\,T$) as shown in Fig. 6.7. As the number of segments in the CPMG sequence (m) is increased while the total time τ is held fixed, the ODF arm time T decreases resulting in suppression of noise from magnetic field fluctuations. The choice of $m = 8$ was made by balancing the reduction in background noise with increased number of π pulses versus error accumulated by over- or under-rotation over the course of many π pulses. Figure 6.8 illustrates this effect.

To create the steady-state COM axial oscillation $Z_c \cos(\omega t + \delta)$, we applied a continuous AC voltage to an endcap of the Penning trap at a frequency $\omega/(2\pi)$ near 400 kHz. This frequency was chosen because it was far from any motional mode frequencies of the ion crystal, and there
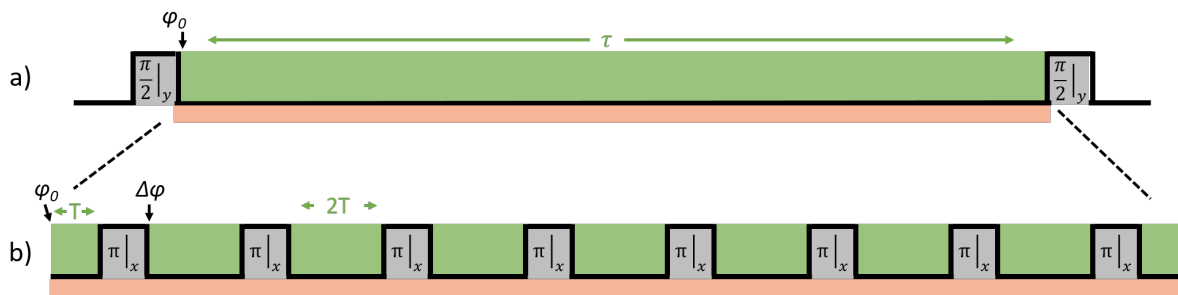
Figure 6.7: Illustration of $m = 8$ CPMG sequence. a) Ramsey sequence with final $\pi/2$ rotation about $\hat{y}$. The classical drive (orange) is on through the whole sequence, and the ODF (green) is turned on between the two $\pi/2$ rotations for a total time τ. b) Dynamical decoupling sequence used to mitigate presence of noise (in particular from magnetic field fluctuations) to allow for increase the total time τ. The total ODF interaction time $\tau = 16T$ for this CPMG sequence. The phase is advanced after each π pulse (see Fig. 6.5).
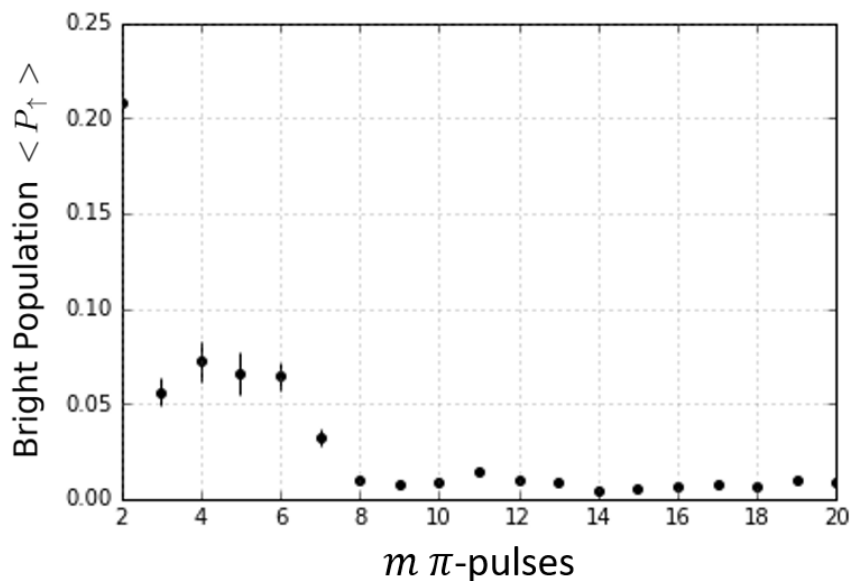
Figure 6.8: Characterization of background signal for various CPMG sequences. Here, the total time τ is held fixed at 24 ms, but the number of π pulses (i.e. the value m) and thus the arm time T is varied. The result is that noise (from magnetic field fluctuations) is suppressed at frequencies below T^{-1}. With additional π-pulses, error from over- or under-rotation may accumulate.

were no observed noise sources. Thus, the background, i.e. the signal without the driven COM axial motion such that $Z_c = 0$, was fully characterized by decoherence due to photon scattering and is given by $\langle P_\uparrow \rangle_{\text{bck}} = \frac{1}{2} \left[1 - e^{-\Gamma \tau} \right]$. Figure 6.9 demonstrates the fact that the background is characterized by photon scattering. By performing the $m = 8$ CPMG sequence with neither ODF beam on, followed by each individually, and finally both together and comparing the experimental results with theory assuming decoherence due to photon scattering with a decay rate Γ calibrated independently (see Ch. 4).

We calibrated the displacement of the ions due to a static voltage applied to the endcap by measuring the resulting movement of the ion crystal in the side-view imaging system. From this calibration, we determined that a 1 V offset results in a 0.97(5) μm displacement of the ions (Fig. 6.10). We estimate that the corrections for using this DC calibration to estimate Z_c for an $\omega/(2\pi) \approx 400$ kHz drive is less than 10 %.

6.4.1 Lineshape

To model the lineshape of the signal, it is necessary to account for the accumulated phase due to the spin-dependent ODF potential without making the simplification that $\omega = \mu$. This results in a characteristic response function for each sequence. The lineshape of this sequence is derived (see Appendix A.1) using the modulation discussed in the first section and assuming a delta function source at a frequency ω. This lineshape is used to generate the theory curves of Figs. 6.11 and 6.12. In general, for a CPMG sequence it is necessary to calculate the phase evolution during $2m$ terms of length T, for a total interaction time of $2m$T.

As shown in the Appendix A.1, the expression for population in $|\uparrow\rangle$ - now with a dependence on the ODF difference frequency μ - is

$$\langle P_\uparrow \rangle = \frac{1}{2} \left[1 - e^{-\Gamma \tau} J_0(\theta_{\text{max}}(\mu)) \right], \tag{6.11}$$

where $\theta_{\text{max}}(\mu)$ is defined in Eq. A.14. Equations 6.11 and A.14 are used to obtain the theoretical line shapes in Figs. 6.11 and 6.12.
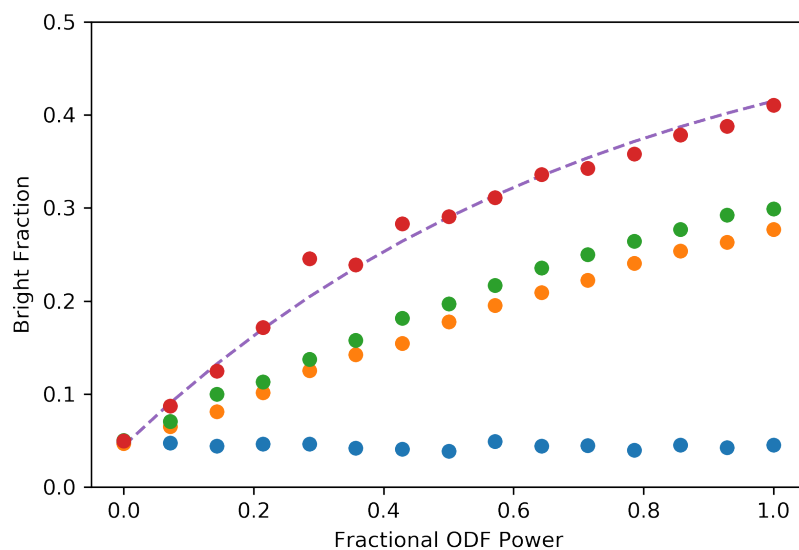
Figure 6.9: Characterization of the background signal for the $\tau = 24$ ms $m = 8$ CPMG sequence as a function of the strength of the ODF. The blue points are without the ODF, where the signal is dominated by magnetic field fluctuations. The green and orange points are with only the lower and upper ODF beams on, respectively. For the red points, both ODF beams are on. The purple dashed line is theory that includes the independently measured photon scattering rate and magnetic field fluctuations.
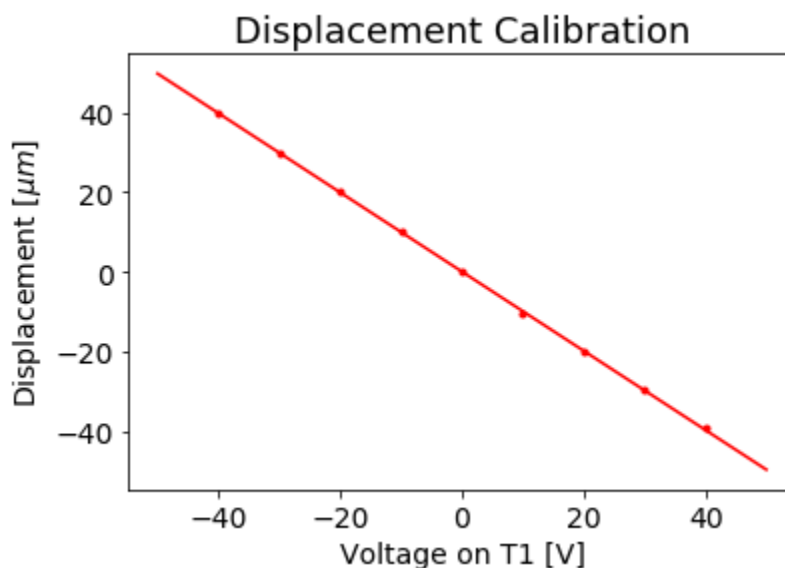
Figure 6.10: Calibration of applied voltage to displacement. A DC voltage was applied to the trap electrode and the displacement of the ion crystal was measured with the sideview imaging EMCCD camera. By varying the DC voltage and measuring the displacement, a calibration of the voltage to displacement can be extracted from a linear fit: $0.97(5)$ μm/V

Figure 6.11 shows the emergence of the measured spin precession signal out of the background as the amplitude Z_c is increased from 500 pm to 5 nm. Figure 6.12 shows the effect of varying the strength of the ODF coupling F_0 while holding the amplitude Z_c fixed at 500 pm. In this case, for the maximum value of F_0 the signal has begun to saturate. As F_0 is increased, the background also increases due to the elevated rate of photon scattering. The measured lineshapes agree well with the theory prediction just described, involving no free parameters.

6.4.2   Assessing the signal-to-noise

Figure 6.13 shows the background and the measured resonant ($\mu = \omega$) response to a $Z_c = 485$ pm oscillation for a range of ODF strengths F_0/F_{0M}, where F_{0M} is the maximum F_0 possible with the set-up from the time ($\sim$40 yN). Agreement with Eq. (6.10) involving no free parameters is excellent. For both Figs. 6.11 and 6.13 the background is within 6% of that determined by independent measurements of the photon scattering decay rates of each ODF beam [13]. The amplitude $Z_c = \theta_{\max}/(\tau F_0/\hbar)$ can be determined from the difference $\langle P_\uparrow \rangle - \langle P_\uparrow \rangle_{\mathrm{bck}}$. We note that $\langle P_\uparrow \rangle - \langle P_\uparrow \rangle_{\mathrm{bck}}$ depends on $\theta_{\max}^2$. Therefore, the sensing protocol described here directly measures Z_c^2. The inset of Fig. 6.13 shows a determination of Z_c^2 for a range of ODF strengths. The uncertainties were calculated from the measured noise of the $\langle P_\uparrow \rangle - \langle P_\uparrow \rangle_{\mathrm{bck}}$ measurements using standard error propagation. These uncertainties go through a minimum, indicating an optimum F_0/F_{0M} value for determining Z_c^2.

To explore the ultimate amplitude sensing limits of our protocol, we performed repeated pairs of $P_\uparrow$ measurements, first with $Z_c = 0$ to get the background, and then with $Z_c \neq 0$. For a given Z_c, 3,000 pairs of measurements were used to determine the average difference $\langle P_\uparrow \rangle - \langle P_\uparrow \rangle_{\mathrm{bck}}$ and the standard deviation $\sigma \left(P_\uparrow - P_{\uparrow,\max} \right)$ of the difference for a single pair of measurements. For each Z_c, F_0/F_{0M} was set close to the value that maximizes the signal-to-noise ratio for determining Z_c^2. This occurs for relatively small $\theta_{\max}$ such that $\frac{1}{2} \left(1 - J_0 \left(\theta_{\max} \right) \right) \approx \theta_{\max}^2/8$. Then, the signal-to-noise
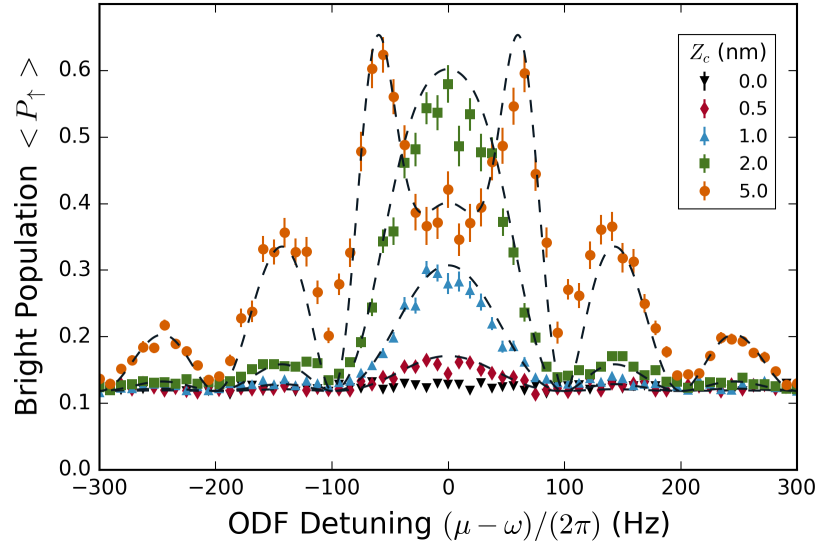
Figure 6.11: Lineshape of the spin precession signal for amplitudes Z_c of 500 pm (red diamonds), 1 nm (blue triangles), 2 nm (green squares), and 5 nm (orange circles) for $\tau = 20$ ms. Black triangles are the background, with the drive turned off. Dashed lines are predictions with no free parameters. Error bars represent standard error. Here $N = 90$ ions and $F_0 = 7.9$ yN.
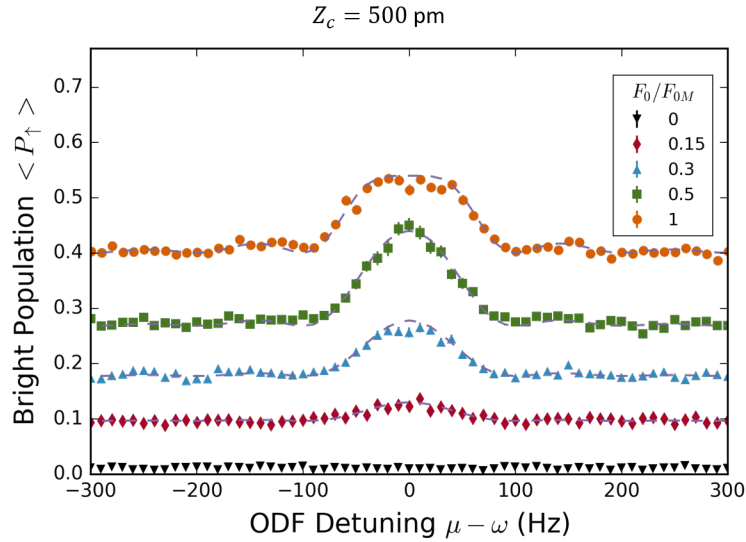
Figure 6.12: Lineshape of the spin precession signal for various values of F_0 with $\tau = 20$ ms. Dashed lines are predictions with no free parameters. Error bars represent standard error. Here $N = 90$ ions and $Z_c = 500$ pm.
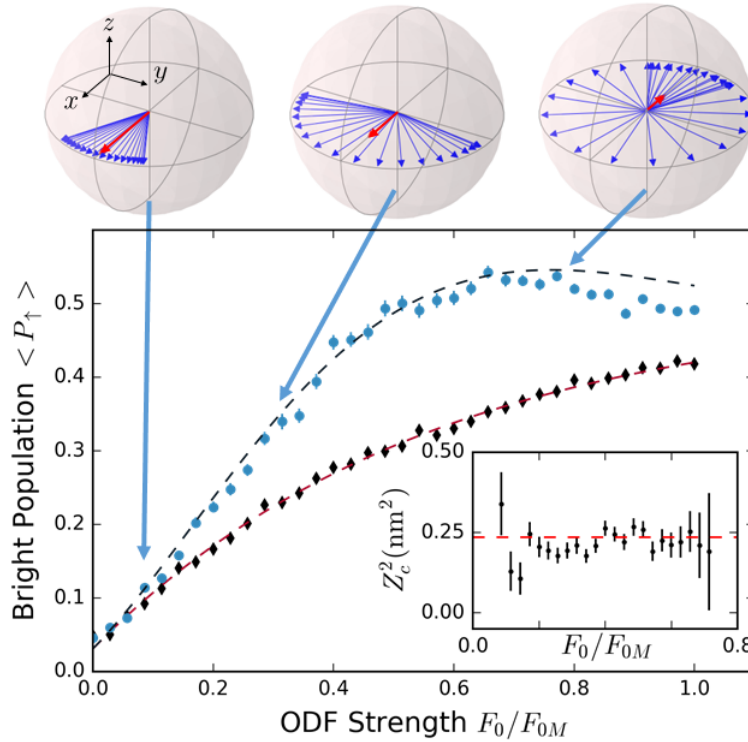
Figure 6.13: **Top:** Bloch sphere representation [72] of spin dephasing for $Z_c = 485$ pm. Each blue vector represents an experimental trial with a different phase δ (see text). From left to right, the spread in the blue vectors corresponds to $\theta_{\max} = 0.470, 1.41, 3.62$ radians and $F_0/F_{0M} = 0.1, 0.3, 0.77$, where F_{0M} is the maximum optical-dipole force. Our experiment measures the length of the Bloch vector averaged over many trials, denoted by the thick red vector. **Main plot:** As a function of ODF strength, the background (black diamonds) with no applied drive and signal (blue points) for a 485 pm amplitude and total ODF interaction time $\tau = 24$ ms is shown. The red dashed line is a fit to the background. The black dashed line is the prediction with no free parameters, given the background fit. Here $N = 75$ ions and $F_{0M} = 41.3$ yN. **Inset:** Black points are experimentally determined values for Z_c^2. Red dashed line is the calibrated value of Z_c^2. Error bars represent standard error.
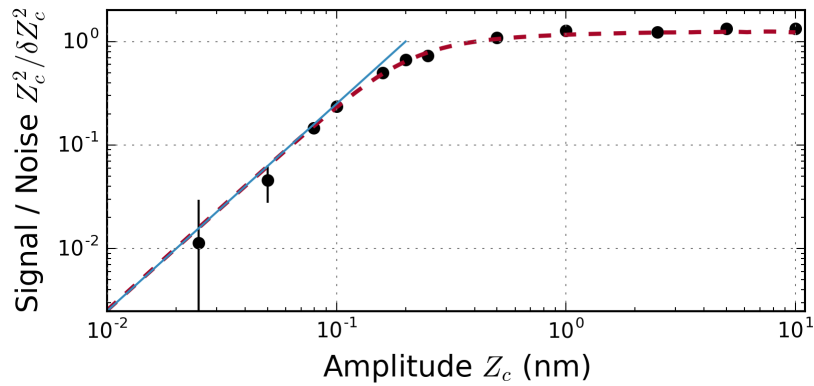
Figure 6.14: Amplitude sensing limits for $N = 85$. Black points are the experimentally measured signal-to-noise for determinations of Z_c^2 from single pairs of $P_\uparrow$, $P_{\uparrow,\mathrm{max}}$ measurements as a function of the experimentally imposed Z_c. Our measurement for $Z_c = 25$ pm is consistent with zero. Red dashed line is the prediction for the signal-to-noise including projection noise and the random COM mode quadrature measured each trial. Blue solid line is the predicted limiting signal-to-noise for small amplitudes (Eq. (6.13)), assuming only projection noise and parameters relevant for our set-up. Error bars represent standard error.

ratio for determining Z_c^2 from a single pair of $P_\uparrow$, $P_{\uparrow,\mathrm{max}}$ measurements is approximately

$$\frac{Z_c^2}{\delta Z_c^2} \approx \frac{\langle P_\uparrow \rangle - \langle P_\uparrow \rangle_{\mathrm{bck}}}{\sigma\left(P_\uparrow - P_{\uparrow,\mathrm{max}}\right)} \ . \tag{6.12}$$

Figure 6.14 displays Eq. (6.12) from measurements acquired with Z_c ranging from 10 nm to as small as 0.025 nm. Excellent agreement is observed with a model (dashed red line) that assumes the only noise sources are projection noise in the spin-state detection and fluctuations in $P_\uparrow$ produced by random variation in the phase δ from one experimental trial to the next.

For amplitudes $Z_c \gtrsim 500\,\mathrm{pm}$, fluctuations in $P_\uparrow$ due to the random variation of the phase δ for different experimental trials dominates. This situation is depicted by the middle Bloch sphere of Fig. 6.13. Here the fluctuations in $P_\uparrow$ are comparable to the difference $\langle P_\uparrow \rangle - \langle P_\uparrow \rangle_{\mathrm{bck}}$, limiting the signal-to-noise of a single determination of Z_c^2 to ~ 1. As Z_c decreases, this noise and the signal decrease while projection noise stays approximately the same, resulting in a decreasing $Z_c^2/\delta Z_c^2$. For small Z_c, the sensitivity is determined (see A.2) by N, δk, and the ratio of the spontaneous decay rate to the optical potential $\xi \equiv \Gamma/(U/\hbar)$, according to

$$\left.\frac{Z_c^2}{\delta Z_c^2}\right|_{\mathrm{limiting}} \approx 0.097 \frac{\sqrt{N}(DWF)^2(\delta\mathrm{k})^2}{\xi^2} Z_c^2 \ . \tag{6.13}$$

For $N = 85$ and values of DWF, δk, and $\xi = 1.156 \times 10^{-3}$ relevant for our set-up, Eq. (6.13) predicts $Z_c^2/\delta Z_c^2 \approx [Z_c/0.2\,\mathrm{nm}]^2$, displayed as the blue line in Fig. 6.14. On the log-log plot the slope of 2 is the result of a signal proportional to Z_c^2 along with a constant readout noise of the spins (here projection noise). We perform 16 pairs of measurements in 1 s, so the signal-to-noise $Z_c^2/\delta Z_c^2 \approx [Z_c/0.2\,\mathrm{nm}]^2$ for a single pair of measurements corresponds to a long averaging time sensitivity of $(100\,\mathrm{pm})^2/\sqrt{\mathrm{Hz}}$ (recall that our protocol measures Z_c^2).

6.5   Off-resonance, phase-coherent sensing

The prior section (6.4) of this chapter described a protocol for sensing displacements of the ion crystal in the case where the phase between the classical driving field and the ODF used to make the measurement is not controlled and is random from shot-to-shot of the experiment. In this

section, the focus is a protocol that exploits a stabilized relative phase and thus allows for coherently sensing the displacement of the ions. To stabilize this relative phase required improvements to the experimental apparatus, which will be described in detail in Section 6.5.1.

As was described in Section 6.2, for the phase incoherent case an experimental sequence using a rotation of the spins about the y-axis was employed. Such a sequence is second-order sensitive to displacements of the crystal, and thus the ultimate sensitivity was reduced (given the presence of spin-dephasing due to photon scattering) compared to a sequence with a final rotation about the x-axis, which is first-order sensitive to displacements.

For this work, EIT cooling was also used to produce a long-term stable $\bar{n}_z \sim 1.6$ COM mode temperature. The addition of EIT cooling improves our sensitivity to small displacements by improving the Lamb-Dicke confinement, which increases the effective spin-dependent force - here, $F_0 = 88$ yN.

Following discussion of the improvements made to the apparatus, this section will outline and document the observed order-of-magnitude improvement in sensitivity to displacements. In addition, details of the sequence and calibrations used, as well as documentation of the characteristic lineshapes observed, will be provided. The phase stabilization of the ODF achieved through this work [19] opens new avenues of research including parametric amplification of the spin-motion interaction [66, 73], which will be explored in the near future.

6.5.1 Experimental improvements

To implement the phase coherent protocol outlined in Section 6.2, the relative phase between the ODF and the classical drive must be controlled. Since the classical drive phase is set by a computer-controlled DDS, it is the phase of the ODF at the ions that must be stabilized. The phase stability of the ODF at the ions requires stabilizing both the optical phase of the ODF beatnote and the axial position of the ions. The wavelength of the ODF optical lattice is $900\,\text{nm}$, so to achieve a phase stability better than $10°$ the equilibrium position of the ions must be maintained to within $25\,\text{nm}$. For our trap, this requires limiting drifts in the approximately $2\,\text{kV}$ confining potentials to

less than $5\,\mathrm{mV}$. In addition, vibrational noise on the apparatus will give rise to phase instability of the ODF relative to the ions - this effect was mitigated by floating the optical table on which the apparatus rests. To stabilize the ODF phase, the beam paths are enclosed to reduce interfermetric drifts between the two ODF beams, and the ODF beatnote is sensed and feedback stabilized before the beams enter the room temperature bore of the superconducting magnet ($\sim 1\,\mathrm{m}$ from the ions, see Fig. 6.15).

The first step in controlling the ODF optical phase at the ions was to interferometrically measure the beatnote and stabilize it. Figures 6.15 and 6.16 illustrate the scheme used to feedback stabilize the ODF beatnote. Just before the two beams are sent into the bore of the magnet and up to the ions, a pair of pickoff mirrors direct light from each beam into an interferometer. This is done approximately 1 meter from the ions, which is about as close to the ions as is possible to pick off light from the beams. The two beams combine on a photodetector and a beatnote is formed. This beatnote (for this work $\mu \approx 400$ kHz, but this can be increased up to $\mu = \omega_z$, see Ch. 7) is mixed with the output of a DDS whose frequency and phase is computer-controlled. The output of the mixer, then, is the phase error of the beatnote relative to the reference signal at ~ 400 kHz. The error signal is amplified and filtered before being sent to a NIST Digital Servo, which serves as the PI-loop feeding back on the error signal. The output of the servo is a voltage intended to stabilize the beatnote, however to feedback on one of the ODF beams we use the RF input to the AOM which controls the frequency and phase of the beam. Thus, the feedback output from the PI-loop must be mixed with the RF drive signal at 210 MHz, as illustrated in Fig. 6.16. We use the frequency modulation input port of a signal generator, which subsequently outputs a 29 MHz frequency-modulated sine wave. This output is doubled in frequency and filtered before being mixed with the 152 MHz output of a DDS. The signal is passed through a final tuneable bandpass filter centered at 210 MHz before the frequency-modulated RF drive centered at 210 MHz is sent on to the AOM controlling one of the two ODF beams.

To quantify, assess, and improve the phase stability of the ODF at the ions, we use the spin-echo sequence shown in Fig. 6.17. These experiments are performed with $\Delta\mu = \omega - \mu = 0$, i.e. with
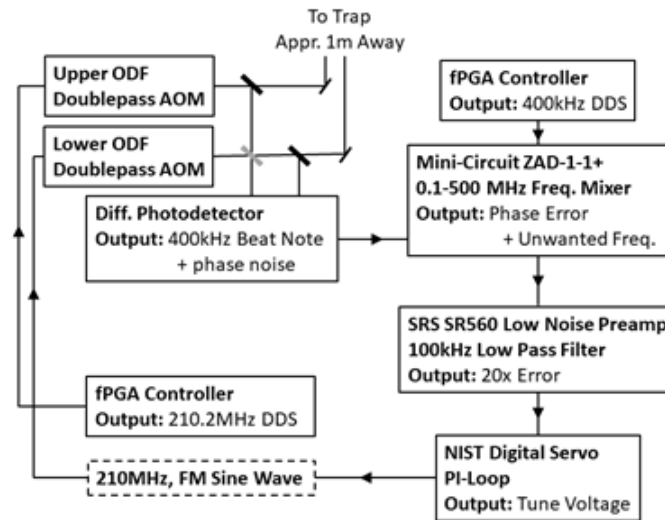
Figure 6.15: Schematic of feedback stabilization of ODF beatnote. To produce the ODF, laser light at 626 is sent via fiber to the experiment table and subsequently frequency doubled to 313 nm. A 50/50 beamsplitter routes the light into two double-pass AOM setups, for fast switching and frequency control (not shown, see Fig. 4.6). To counteract phase noise accumulated over the few meter path lengths of the two beams, feedback is applied to one of the AOMs. Two pickoffs about 1 meter from the trap are used to route light into an interferometer and a beatnote is formed at 400 kHz. This signal is mixed down with a 400 kHz signal from an FPGA controlled DDS (such that the exact frequency can be controlled in the course of running the experiment) to produce an error signal, amplified, and sent to a NIST digital servo PID. The signal output from the digital servo must be mixed-up to 210 MHz (see next figure).
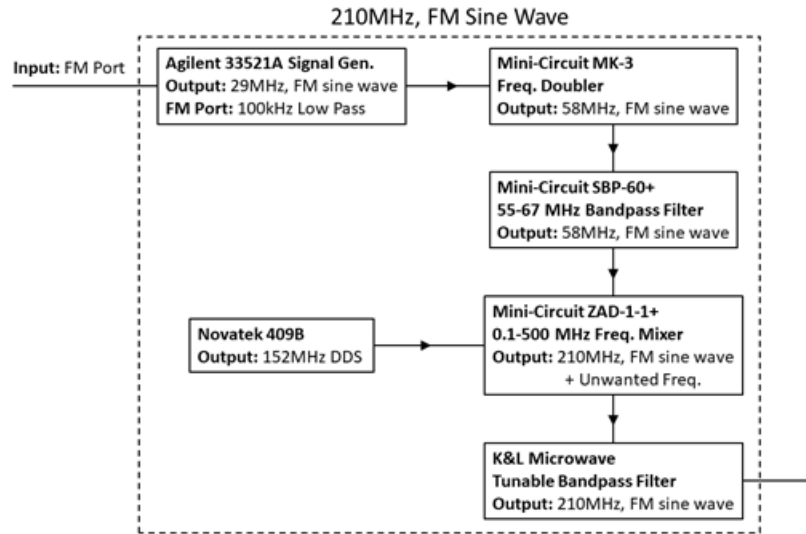
Figure 6.16: Since the AOM being used has a center RF driving frequency of 210 MHz, the output from the PID loop must be mixed-up to 210 MHz. The output voltage is sent to the frequency modulation port of an Agilent 33421A signal generator set to an output of 29 MHz with an amplitude appropriate for driving the AOM. This signal is doubled in frequency, filtered, and mixed with a 152 MHz DDS signal. With another stage of filtering, the frequency modulated 210 MHz RF signal is sent on to the AOM to stabilize the 400 kHz beatnote.
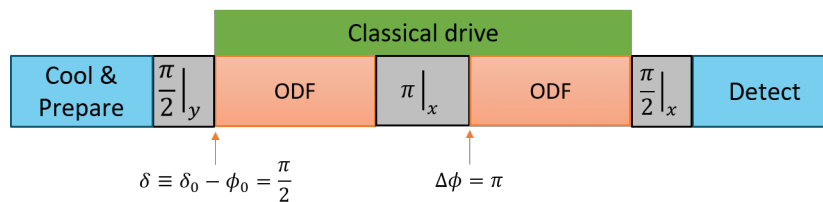
Figure 6.17: Illustration of sequence used to measure the stability of the relative phase between the ODF and the classical drive. δ is the relative phase and is initialized at $\pi/2$ such that the two fields oscillate out of phase and no spin precession should be accumulated. After the π pulse, the ODF phase is advanced by $\phi = \pi$ such that any spin precession accumulated is added coherently over the two arms of the sequence. If the relative phase remains $\delta = \pi/2$ over the course of the sequence and from shot-to-shot, then after the final rotation $\pi/2$ about $\hat{x}$ the Bloch vector will remain along the $\hat{x}$-axis (see Fig. 6.19).

the frequency of the ODF equal to that of the drive, and with an ODF phase advance $\Delta\phi = \pi$, so that the spin-precession is accumulated in each arm. To be first-order sensitive to the phase noise of the ODF, the initial relative phase is set to $\delta = \pi/2$. Also, a large classical displacement amplitude ($Z_c \sim 5.5\,\mathrm{nm}$) is used with $\theta_{\mathrm{max}} \sim 0.7\pi$ to improve the phase noise sensitivity.

If from one realization of the experiment to the next the phase $\delta = \pi/2$ remains constant, then no spin-precession occurs in either of the ODF arms, and the Bloch vector remains along the x-axis for each trial as shown in Fig. 6.19 (a). Then, following the final $\pi/2$-pulse about the x-axis, the noise in the detected bright fraction is limited to spin projection noise. However, if the phase of the ODF varies from one experimental trial to the next, then the resulting spin-precession causes dephasing of the Bloch vector for different iterations of the experiment as shown in Fig. 6.19 (b), which results in increased noise in the bright fraction after the final $\pi/2$-pulse.

With this experimental protocol we can now assess the stability of the relative phase and investigate potential noise sources that may be limiting the stability. Figure 6.18 illustrates the initial phase stability and subsequent improvement using the same experimental sequence described previously. Initially, the bright fraction wandered from full bright to full dark (Fig. 6.18 (a)) over the course of a few seconds. After improving the laser phase stability and motional stability of the ions, the phase is significantly more stable (Fig. 6.18 (b)-(e)), though there is some residual noise above projection noise (illustrated in Fig. 6.18 (f), which is without the classical drive and near projection noise limited). Several steps were taken to improve the relative phase. First, electrical noise was reduced by disconnecting the high voltage power supplies used for the trap electrodes from the DAC used to remotely control them, and further mitigated by connecting the T2 and T3 electrodes (the electrodes on either side of the central, segmented electrode, see Ch. 3) to the same power supply so that residual noise on those electrodes is common mode for the ion crystal between them (Fig. 6.18 (c)). Then, optical phase instabilities driven by air currents over the ODF beam pathlength were mitigated by sealing the bore of the magnet (which acts like a chimney) and covering the ODF beam path on the optical table (Fig. 6.18 (d)). Finally, vibrational noise from the ground which causes the trap to move relative to the ODF laser beams is mitigated by floating
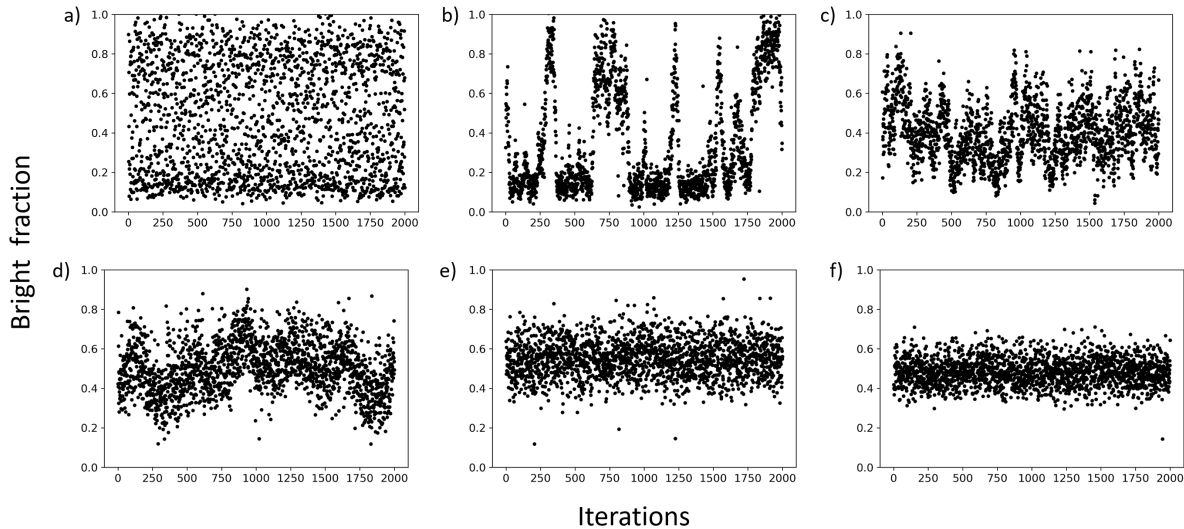
Figure 6.18: Improving the stability of the relative phase between the classical drive and ODF. The following plots use the sequence outlined in the text and in Figs. 6.17 and 6.19. a) Here the relative phase was left uncontrolled and varies randomly from shot-to-shot. b) Triggering the experimental sequence such that the DDS phases for the classical drive and ODF are synchronized. The relative phase at the ions wanders over $180°$ in a few seconds. c) Electrical noise - from the DAC used to set the trap voltages remotely, ground loops, and other unknown sources - affects the phase. Here the high voltage power supplies are set to 'local' mode and are disconnected from the DAC. Additionally, the electrodes T2 and T3 (the electrodes on either side of the central, segmented electrode, see Ch. 3) are connected together. d) Boxing up the ODF beam path on the optical table as well as sealing the bore of the magnet mitigates the effects of air currents on the relative phase stability at the ions. e) Floating the table removes some low frequency vibrations that jostle the trap relative to the ODF laser beams. f) Comparison to the same experiment, but with the classical drive switched off.

the optical table (Fig. 6.18 (e)).

Figure 6.19 (c) shows the resulting bright fraction of a 210 ± 20 ion cloud over 2000 iterations of this phase stability experiment and represents the ultimate phase stability so far achieved. Each experiment lasts 9 ms, so this set of experiments analyzes the stability over a 18 second interval. The red dashed lines represent the standard deviation of spin projection noise. The phase remains relatively constant over the 18 second interval as shown by the data in Fig. 6.19 (c) with some fast shot-to-shot noise that increases the standard deviation of the bright fraction by about a factor of two over projection noise.

From this increased noise in the bright fraction, we calculate the corresponding phase noise of the ODF. The population of spins in the $|\uparrow\rangle$ state at the end of this experimental sequence is

$$P_\uparrow = \frac{1}{2} \left[1 - e^{-\Gamma\tau} \sin(\theta) \right], \tag{6.14}$$

where $\theta = \theta_{\max} \cos(\delta)$ when $\Delta\mu = 0$ and Γ is the rate of spin-decoherence, which is predominantly due to off-resonant light scatter from the ODF beams. We assume $\delta = \pi/2 + \Delta\theta$, where the shot-to-shot phase noise $\Delta\theta$ is small. Solving Eq. (6.14) for $\Delta\theta$, we find

$$\Delta\theta \approx \frac{e^{\Gamma\tau} \left(1 - 2P_\uparrow\right)}{\theta_{\max}}. \tag{6.15}$$

Figure 6.19 (d) is a histogram of the phase noise for the data shown in Fig. 6.19 (c). The dashed vertical red lines correspond to the 2° standard deviation from converting projection noise to phase noise, and the blue dashed curve is a Gaussian fit to the measured phase noise with a standard deviation of about 5 degrees. This measurement includes projection noise, and is therefore a conservative estimate of the phase stability. With this phase stability, other sources of noise and background offsets should be the limiting factors for the phase-coherent sensing experiments.

Slow drift of the ODF phase on the ions - most likely due to evolving air currents - means that though the shot-to-shot phase stability is good, over the course of many 10s of seconds to minutes the relative phase evolves. Thus, prior to any experiment the relative phase is scanned. From a fit to the scan we set the relative phase of the two fields (classical drive and ODF) so they
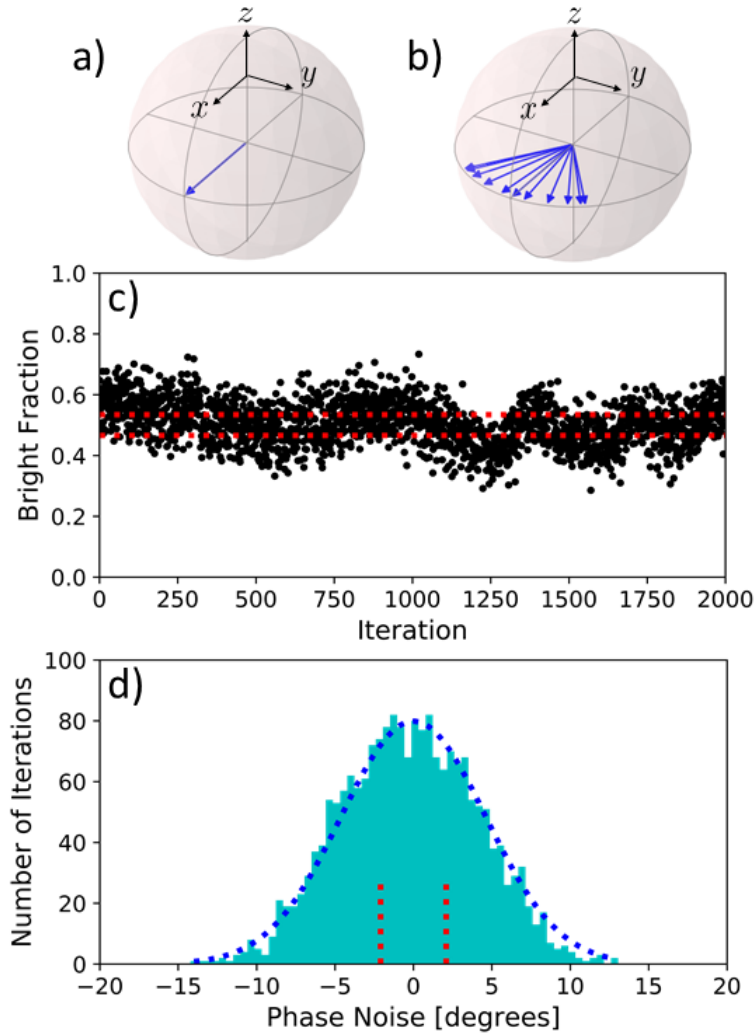
Figure 6.19: To measure the phase stability of the ODF at the ions, a spin-echo sequence is used in which the relative phase between the driven displacement and ODF is initially set to $\delta = \pi/2$. With the ODF and driven displacement out-of-phase, no spin-precession occurs in either application of the ODF. Therefore, in the absence of phase noise (a), the Bloch vector remains pointing along the x-axis. However, in the presence of phase noise (b), spin-precession is accumulated, and the Bloch vector undergoes different amounts of spin precession from one trial of the experiment to the next. (c) After the final $\pi/2$-pulse about the x-axis, the shot-to-shot variations in the spin-precession are rotated into noise in the measured bright fraction (black data) over that expected from spin projection noise (red dashed lines). (d) Using a theory model, this increase in the noise in the bright fraction is interpreted as 5° Gaussian phase noise between the driven motion and oscillating spin-dependent force (dashed blue curve).

are in-phase. For data-taking over longer periods of time, this phase scan is checked periodically (typically every 20 seconds) to ensure it doesn't drift off. Figure 6.20 shows an example of a scan over this relative phase with a sinusoidal fit. The phase offset is extracted and used to set the ODF phase such that it matches the classical drive phase.

6.5.2   Phase-coherent lineshapes

Having improved the relative phase stability from 'random' to 'controlled' and characterized the phase noise to have a standard deviation of about 5 degrees, we proceed with extending the phase-coherent protocol to sense small displacements of the ion crystal. This section will describe in detail the sequence used to perform this measurement and the theoretical and experimental characterization of the lineshape (or response function) of the signal.

This section mirrors Secs. 6.3 and 6.4.1 in its general formalism, though the exact sequence used for this work differs from that described in Sec. 6.4. For reference, the relevant full Hamiltonian is repeated here:

$$\hat{H}_{ODF} = U \sum_i \sin(\delta k \cdot \hat{z}_i) \cos(\mu t + \phi) \hat{\sigma}_i^z - U \sum_i \cos(\delta k \cdot \hat{z}_i) \sin(\mu t + \phi) \hat{\sigma}_i^z. \tag{6.16}$$

With a classical COM motion characterized by a displacement amplitude Z_c and frequency ω, the Hamiltonian becomes:

$$\hat{H}_{ODF} \approx F_0 \, Z_c \cos((\omega - \mu)t + \delta) \sum_i \frac{\hat{\sigma}_i^z}{2}. \tag{6.17}$$

As before, we consider how to extend the sequence to longer times to enhance the sensitivity. The optimum sensitivity to small displacements requires a Ramsey sequence with a long free-precession duration (on the order of several milliseconds) as shown in Fig. 6.21 (a), which makes this protocol susceptible to spin decoherence from magnetic field fluctuations. To mitigate this effect, we employ multiple equally spaced π-pulses about the x-axis in a Periodic Dynamical Decoupling sequence (PDD) as shown in Fig. 6.21 (b). By shortening the free-precession interval T we suppress
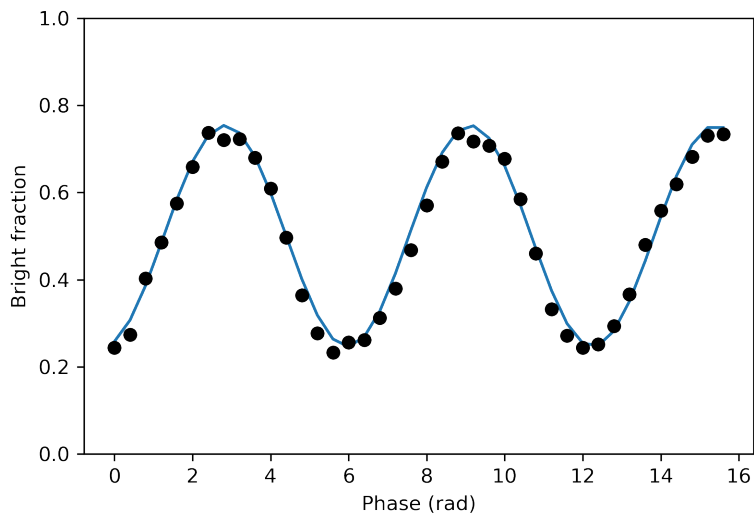
Figure 6.20: Calibration for relative phase between ODF and classical drive. Fitting to this oscillation allows for extracting the relative phase offset between the ODF and the classical drive and ensures that the two fields are in phase for the following experiment. The calibration sequence used matches the experimental sequence to follow.
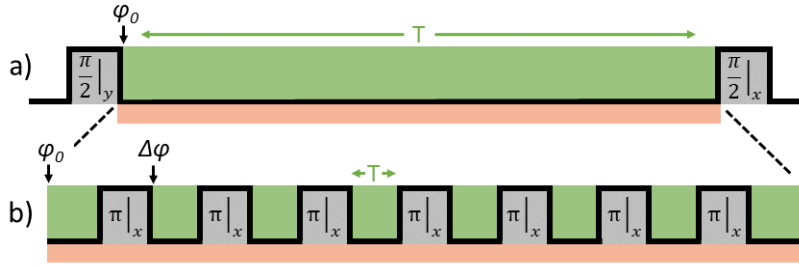
Figure 6.21: a) A sketch of the equivalent Ramsey sequence of this experimental protocol consisting of microwave pulses (grey boxes), and application of the ODF (green boxes) while the ion crystal is being driven by a classical drive (orange box). For the given ODF strength, a long free-evolution duration is required to obtain the optimum sensitivity to small displacements ($\tau = T$). b) To suppress magnetic field fluctuations, the free-precession period is divided into smaller sections by π-pulses about the x-axis with appropriate phase advances of the ODF ($\tau = 8T$). The duration of these pulses are not drawn to scale.

magnetic field noise for frequencies below T^{-1}. With no phase advance of the ODF $\Delta\phi$ after these microwave π-pulses, this spin-echo protocol would also cancel the precession from the spin-motion coupling. However, with the proper $\Delta\phi$ (Sec. 6.3), the desired spin-precession signal is accumulated in each arm.

When $\Delta\mu = \omega - \mu \neq 0$, spin-precession from the spin-motion interaction of Eq. (6.17) still occurs, but the phase evolution throughout the sequence must be taken into account as well. This results in a characteristic line shape for the given experimental sequence. In this section, we theoretically and experimentally analyze the line shape from a constant amplitude driven displacement. For simplicity, the derivation assumes the spin-echo sequence shown in Fig. 6.1 (b), but using trigonometric identities the phase factors reduce to the same analytical expression for spin-echo sequences with $m = 2^n - 1$ (for n any nonzero integer) π-pulses. We also neglect t_d (where, again, t_d is a delay between setting the ODF phase and the start of the sequence) here, since $T \gg t_d$, so the effect on the signal is negligible. This brief derivation mirrors that described in Appendix A.1.

The spin-precession accumulated in a general sequence is

$$\begin{aligned}
\theta(\mu) &= \frac{F_0 Z_c}{\hbar} \int \cos\left(\Delta\mu t + \delta\right) dt \\
&= \frac{F_0 Z_c}{\hbar} \frac{2\sin\left(\frac{\Delta\mu}{2}T\right)}{\Delta\mu} \chi(\mu, \omega),
\end{aligned} \tag{6.18}$$

where the phase evolution of each ODF arm is included in $\chi(\mu, \omega) = \sum_j \chi_j(\mu, \omega)$ and is determined by the particular sequence that is used. For an application of the spin-motion coupling starting at t_i and ending at t_f

$$\chi_j = \cos\left[\frac{\Delta\mu}{2}(t_i + t_f) + \delta\right], \tag{6.19}$$

so for the two arms of the spin-echo sequence with the timings and phase advance discussed in Sec. 6.5.2

$$\chi_1 = \cos\left[\frac{\Delta\mu}{2}T + \delta\right], \tag{6.20}$$

and

$$\chi_2 = \cos\left[\frac{\Delta\mu}{2}(3T + 2t_\pi) + \mu(T + t_\pi) + \delta\right]. \tag{6.21}$$

Summing these terms and using the drive frequency of Eq. (6.6), we find

$$\theta(\mu) = \frac{F_0 Z_c \tau}{\hbar}\text{sinc}\left(\frac{\Delta\mu}{2}T\right)\cos\left(\frac{\Delta\mu}{2}T + \delta\right), \tag{6.22}$$

where $\tau = (m+1)T$ is the total time the ODF is applied. Again, this expression is dependent on the particular sequence used, but is valid for the spin-echo sequences with $m = 2^n - 1$ π-pulses discussed here.

Shown in Fig. 6.22 are the measured line shapes for a spin-echo sequence with $m = 7$ π-pulses. When no drive is applied ($Z_c = 0$), the bright fraction remains near 0.5 independent of the ODF frequency. As the displacement amplitude is increased, a signal emerges from the background. On-resonance with $\delta = 0$, the bright fraction is decreased for small displacement amplitudes. In contrast, for the largest displacement amplitude ($Z_c = 1.11\,\text{nm}$), the bright fraction is increased on-resonance since the induced spin-precession exceeds π. Figure 6.23 demonstrates control over the relative phase between the classical drive and ODF. The same sequence is used as in Fig. 6.22 with a displacement amplitude of 300 pm (blue data in Fig. 6.22).

The curves shown in Figs. 6.22 and 6.23 are theory with no adjustable parameters. Equation 6.14 is used to convert the calculated spin-precession accumulated for the spin-echo sequence (Eq. (6.22)) to a bright fraction. The theory agrees well with the experiments for a range of displacement amplitudes and ODF frequencies.
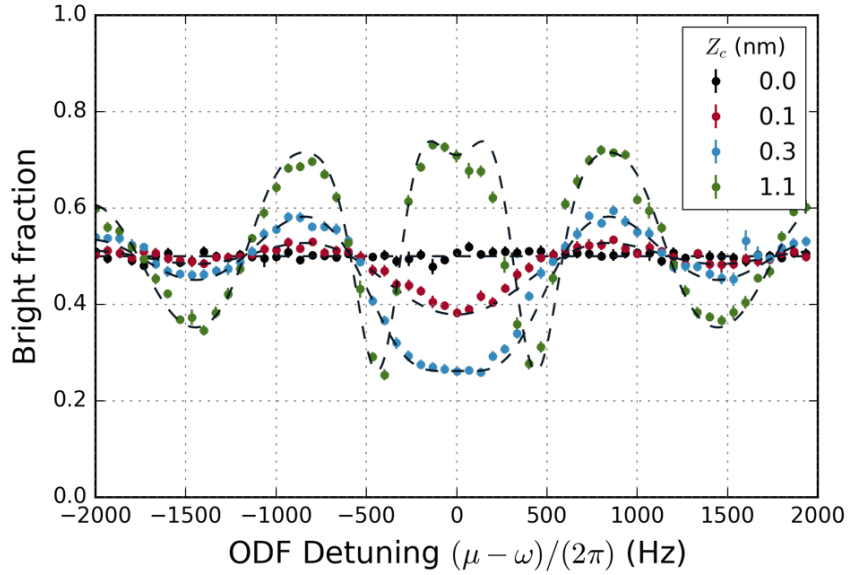
Figure 6.22: Measured bright fraction versus ODF detuning for various displacement amplitudes (symbols). The error bars represent one standard deviation of uncertainty. These line shapes are for a $m = 7$ spin-echo sequence with an arm time $T = 850\,\mu s$ and the 2D crystal array consists of $N \sim 69$ ions. They are well described by theory (curves) given by Eqs. 6.14 and 6.22 with no adjustable parameters.
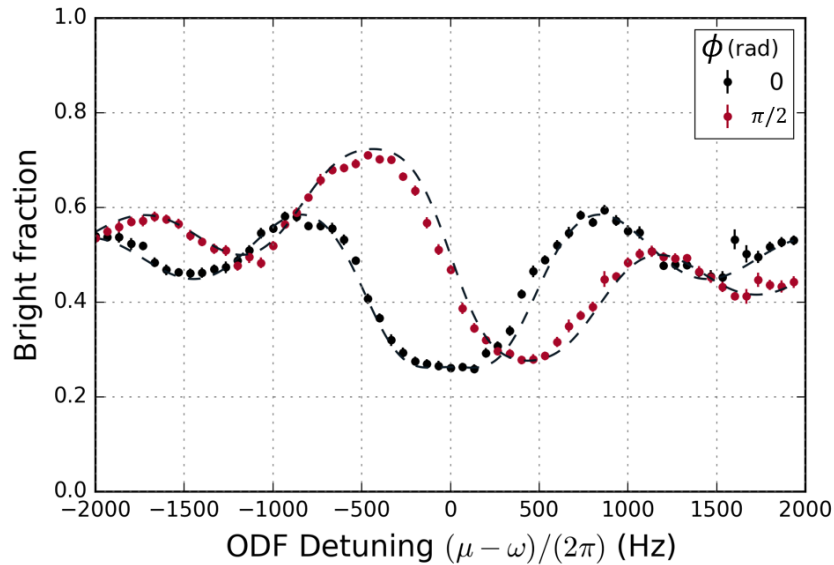
Figure 6.23: Measured bright fraction versus ODF detuning for $\phi = 0, \pi/2$. The error bars represent one standard deviation of uncertainty. These line shapes are for a $m = 7$ spin-echo sequence with an arm time $T = 850\,\mu s$ and the 2D crystal array consists of $N \sim 69$ ions. They are well described by theory (curves) given by Eqs. 6.14 and 6.22 with no adjustable parameters.

6.5.3   Assessing the phase-coherent signal-to-noise

Following a similar procedure as in Ref. [18] and Sec. 6.4.2, we determine the ultimate amplitude sensing limit of this protocol by performing repeated pairs of $P_\uparrow$ measurements with the spin-dependent force applied at the same frequency as the classical drive. Instead of using one of the two measurements to measure the background ($Z_c = 0$) as was done in Ref. [18], the ability to control the relative phase between the classical drive and ODF allows us to advance the phase by π between the first $P_\uparrow^1$ ($\delta = 0$) and second $P_\uparrow^2$ ($\delta = \pi$) experiments. This reverses the relative sign of the signal, and by taking the difference

$$\langle P_\uparrow^2 \rangle - \langle P_\uparrow^1 \rangle = e^{-\Gamma \tau} \sin(\theta_{\max}), \tag{6.23}$$

we remove common offsets in the background and increase the size of the signal for this pair of experiments by a factor of two. Equation 6.23 can be used to estimate $\theta_{\max}$ and the displacement amplitude Z_c through $\theta_{\max} = F_0 Z_c \tau / \hbar$.

To assess the stability of the measurement, the Allan deviation can be calculated as a function of the number of experiments performed. Figure 6.24 is a plot of the Allan deviation of the measured bright fraction $P_\uparrow^2 - P_\uparrow^1$ for 3000 iterations of this measurement. The noise in these measurements averages down as the square root of the number of iterations M indicating good long-term stability of the experimental set-up.

The standard deviation $\delta\theta_{\max}$ in estimating $\theta_{\max}$ is determined by the standard deviation (ideally spin projection noise) $\sigma(P_\uparrow^2 - P_\uparrow^1)$ in the difference signal measurements through

$$\sigma(P_\uparrow^2 - P_\uparrow^1) = e^{-\Gamma \tau} \cos(\theta_{\max}) \delta\theta_{\max}. \tag{6.24}$$

Since

$$\frac{Z_c}{\delta Z_c} = \frac{\theta_{\max}}{\delta\theta_{\max}} \tag{6.25}$$

the maximum sensitivity to small displacements occurs when $\theta_{\max}/\delta\theta_{\max}$ is maximized. Using Eq. 6.25 and solving for $\theta_{\max}$ and $\delta\theta_{\max}$ from Eq. (6.23) and Eq. (6.24), respectively, we can calculate the angle at which the optimal sensitivity is achieved. Figure 6.25 is a plot of the amplitude
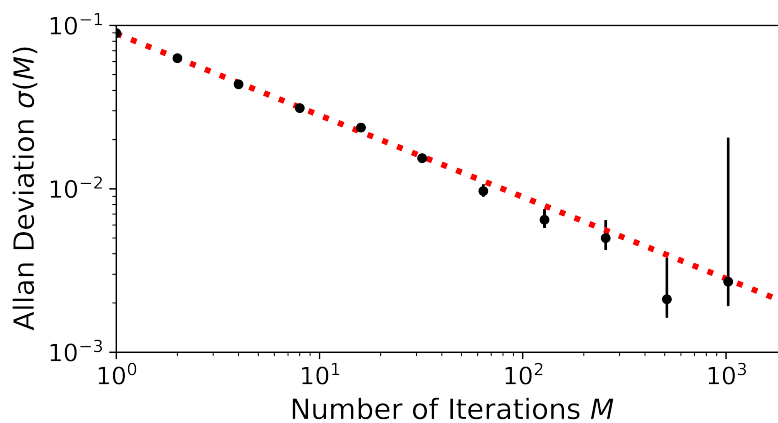
Figure 6.24: Allan deviation of the bright fraction measured over $\sim$3000 iterations of the experiment for the $Z_c = 49$ pm data set. The fit (red dashed line) shows that the noise in the bright fraction is uncorrelated over this experimental interval, and therefore averages down as the square-root of the number of experiments. Each iteration of the experiment (two $m = 7$ spin-echo sequences) lasts about 30 ms.

sensitivity versus the angle of spin-precession for a range of displacement amplitudes Z_c, where $\theta_{\max}$ is controlled by varying F_0. Note that increasing the strength of the ODF also increases the rate of photon scattering, which needs to be included when finding the angle. Measurements and theory show that the optimum sensitivity to displacements occurs for $\theta_{\max} \sim 0.2\pi$ for the largest displacement amplitudes $Z_c \sim 200\,\mathrm{pm}$ reported here. For these large displacements, we lower the ODF strength to remain at this optimum sensitivity.

The optimal sensitivity for small displacements requires higher ODF strength. Higher ODF strength increases the impact of photon scattering, and $\theta_{\max}/\delta\theta_{\max}$ is maximized at small $\theta_{\max}$ as shown in Fig. 6.25 where small angle approximations to Eqs. 6.23 and 6.24 are valid. For small $\theta_{\max}$,

$$\frac{\theta_{\max}}{\delta\theta_{\max}} \approx \frac{\langle P_\uparrow^2 \rangle - \langle P_\uparrow^1 \rangle}{\sigma(P_\uparrow^2 - P_\uparrow^1)}. \tag{6.26}$$

We define the experimentally determined signal-to-noise ratio SNR of a single pair of measurements as

$$\mathrm{SNR} \equiv \frac{\langle P_\uparrow^2 \rangle - \langle P_\uparrow^1 \rangle}{\sigma(P_\uparrow^2 - P_\uparrow^1)}. \tag{6.27}$$

Therefore, for small amplitudes Z_c, the SNR provides a measure of the signal-to-noise ratio $Z_c/\delta Z_c$ for determining Z_c in a single pair of measurements.

Assuming the noise is limited by spin projection noise such that $\delta\theta_{\max} = e^{\Gamma\tau}/\sqrt{2N}$, limiting amplitude sensitivity of this protocol is (see A.3)

$$\left.\frac{Z_c}{\delta Z_c}\right|_{limiting} \approx \mathrm{DWF}(\Delta k Z_c)\sqrt{2N}\frac{U\tau}{\hbar}e^{-\xi U\tau/\hbar}, \tag{6.28}$$

where $\xi = \Gamma/(U/\hbar) \sim 1.14 \times 10^{-3}$ is the ratio of the spin-decoherence to the strength of the optical potential. For a given number of ions, the amplitude sensitivity increases for longer applications of the ODF potential until spin-decoherence diminishes the contrast. Equation 6.28 is maximized when $\Gamma\tau = 1$, which for a typical $\Gamma \sim 147\,\mathrm{s}^{-1}$ sets $\tau \sim 6.8\,\mathrm{ms}$. This motivates the duration of the protocol we implemented and corresponds to an ultimate amplitude sensitivity of

$$\left.\frac{Z_c}{\delta Z_c}\right|_{ultimate} \approx \frac{F_0\tau}{\hbar e}\sqrt{2N}Z_c = \frac{Z_c}{36\,\mathrm{pm}}, \tag{6.29}$$
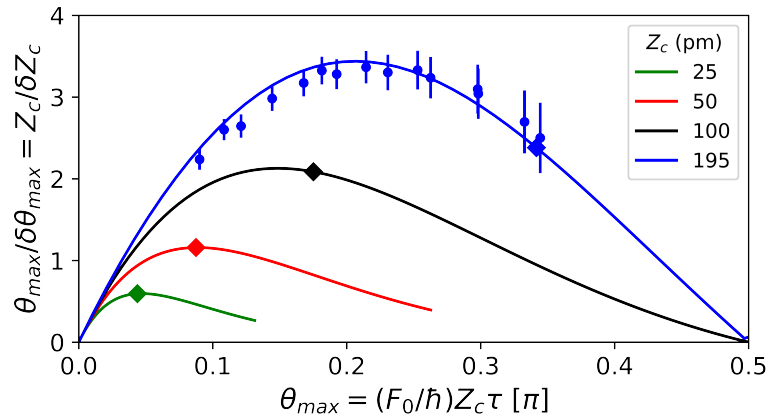
Figure 6.25: Amplitude sensitivity versus the angle of spin-precession for a range of displacement amplitudes Z_c. Here $\tau = 6.8$ ms is fixed, and the $\theta_{\max}$ is controlled by varying the strength of the ODF from 0 to $3F_{0M}$, where F_{0M} is the maximum ODF achievable at the time. The circles correspond to measurements with $Z_c = 195$ pm (error bars represent one standard deviation of uncertainty from repeated trials of the experiment), and the diamonds identify the location of maximum ODF strength. For $Z_c = 195$ pm, the optimum amplitude sensitivity under these conditions occurs for $\theta_{\max} \sim 0.2\pi$, which requires ODF strengths below the maximum. As the displacement amplitude is decreased, the maximum amplitude sensitivity occurs at smaller spin-precession angles where the full ODF strength is required. The theory curves assume the experimentally observed 25% increase in the observed noise over spin projection noise.

for the $N = 88$ ions and $F_0 = 88\,\mathrm{yN}$ of these experiments.

Figure 6.26 shows the measured SNR for determining Z_c from a single pair of measurements. Each SNR measurement was calculated from about 3000 pairs of experiments where the relative phase of the classical drive and the ODF was changed by π between the measurements. The symbols and curve in black correspond to the previous phase-incoherent measurements and projection noise limited theory, respectively. In those experiments, a $500\,\mathrm{pm}$ displacement amplitude was detected with a single measurement SNR of 1, and an amplitude of $50\,\mathrm{pm}$ was detected after averaging over the 3000 pairs of experiments. Due to the shot-to-shot phase noise inherent in this scheme, the SNR was limited to approximately 1 for amplitudes $Z_c \gtrsim 500\,\mathrm{pm}$.

With the phase-coherent protocol (blue data in Fig. 6.26), a displacement amplitude of $49\,\mathrm{pm}$ is detected with a SNR of 1 with a single pair of measurements, which corresponds to an order-of-magnitude improvement in the amplitude sensitivity. This amplitude is larger than that predicted by Eq. (6.29) mainly due to additional noise in the bright fraction. This excess noise most likely results from magnetic field fluctuations at frequencies above T^{-1}, and ideally a sequence with additional π-pulses (smaller T) would reduce this noise. However, errors in the microwave pulses currently limits this protocol to $1.25\times$ spin-projection noise with a $m = 7$ spin-echo sequence.

The solid blue curve of Fig. 6.26 is a full calculation of the SNR defined in Eq. (6.27) for the conditions of the experimental measurements and taking into account a 25% increase in the experimental noise over spin projection noise. The agreement is good for large amplitudes ($Z_c \gtrsim 50\,\mathrm{pm}$). The solid blue curve approaches the approximate result given by Eq. (6.29) modified by the excess experimental noise for small angles ($Z_c \lesssim 100\,\mathrm{pm}$). At these smaller displacement amplitudes, the theory deviates from the experimental results. This is due to an apparent $\sim 2\%$ offset in the background between the first $P_\uparrow^1$ and second $P_\uparrow^2$ measurements. This offset was determined by extrapolating a linear fit of the signal $\langle P_\uparrow^2 \rangle - \langle P_\uparrow^1 \rangle$ to zero displacement amplitude (see Fig. 6.27). We believe this offset is due to a small amount of cross talk between experimental control signals and the rf potential applied to the end cap electrode. When the theory signal is reduced by this experimental offset, we have good agreement between theory and experiments for
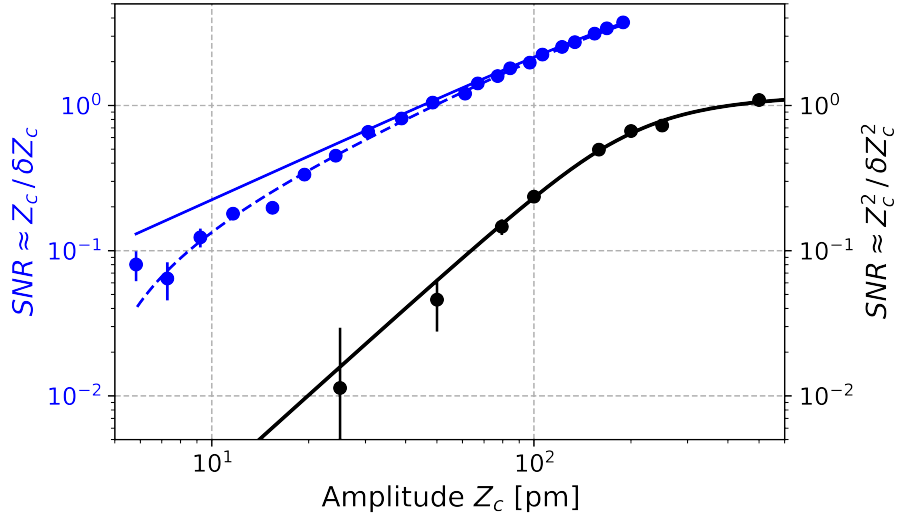
Figure 6.26: Amplitude sensing limits for a crystal of $N \sim 88$ ions. The black symbols and curve show the previous phase-incoherent measurements and projection noise limited theory of Ref. [18], respectively. With the phase-coherent scheme (blue symbols), a displacement amplitude of $49\,\mathrm{pm}$ is detected with a single measurement SNR of 1, which corresponds to an order-of-magnitude improvement in the sensitivity to small displacements. At the smallest amplitudes, the SNR for the phase-incoherent scheme scales as $(Z_c/\delta Z_c)^2$. For the phase-coherent scheme, theory predicts first-order sensitivity to the displacement amplitude (solid blue curve). However, at small amplitudes, the SNR measurements fall off faster than this prediction due to an offset in the background between the two $m = 7$ spin-echo measurements (see text and Fig. 6.27). We find good agreement between theory and experiment when this offset is included in the theory (blue dashed curve). Both of these phase-coherent theory curves assume the measured 25% increase in the background noise over projection noise. The smallest detected amplitude with the ~ 3000 experiments used here is $5.8\,\mathrm{pm}$. The error bars represent one standard deviation of uncertainty from repeated trails of the experiment.

all displacement amplitudes (dashed blue curve). Measurements for amplitudes $Z_c < 5.8$ pm will require either a careful calibration of this offset or determining the source of the offset and getting rid of it entirely.

The offset in the background levels between the first $P_\uparrow^1$ ($\delta = 0$) and second $P_\uparrow^2$ ($\delta = \pi$) signal measurements impacts the current sensitivity of this protocol for determining small amplitudes. Figure 6.27 (a) shows the measured bright fraction at small amplitudes for these two experiments. The predicted linear dependence with Z_c is observed. However, linear fits (dashed curves) show an offset from expected background (bright fraction of 0.5 at zero displacement amplitude).

In Fig. 6.27 (b), we plot the difference between these two experiments, which is used as the experimental signal in Eq. 6.27. By taking the difference, we remove common drifts in the background as seen by the reduction in the scatter of the data away from the linear fit. However, an approximate 2% offset remains. We believe this offset is due to a small amount of cross talk between experimental control signals and the rf potential applied to the end cap electrode. This offset is rather robust since the data shown in Fig. 6.27 was taken over several hours on two different days. Further investigation will be required to calibrate or reduce this offset.

The slope of the SNR in Fig. 6.26 shows the benefit of the first-order amplitude scaling of this phase-coherent protocol over the second-order amplitude scaling of the prior phase-incoherent work [18]. If Z_c is reduced by some factor n, the phase coherent scheme requires n^2 measurements to average down the noise. In contrast, the phase incoherent scheme requires n^4 measurements.

Each iteration of this phase-coherent experiment consists of two $m = 7$ spin-echo sequences, and lasts a total duration of about 30 ms. Therefore, the displacement sensitivity of this technique is approximately 8.4 pm$/\sqrt{\text{Hz}}$. This implies force and electric field sensitivities of $(12 \, \text{yN/ion})/\sqrt{\text{Hz}}$ and $(77 \, \mu\text{V/m})/\sqrt{\text{Hz}}$, respectively.

6.6   Summary and outlook

This chapter gave a detailed overview of a pair of experiments [18, 19] concerned with measuring off-resonantly drive displacements of a 2D crystal of ions. Both sets of experiments made
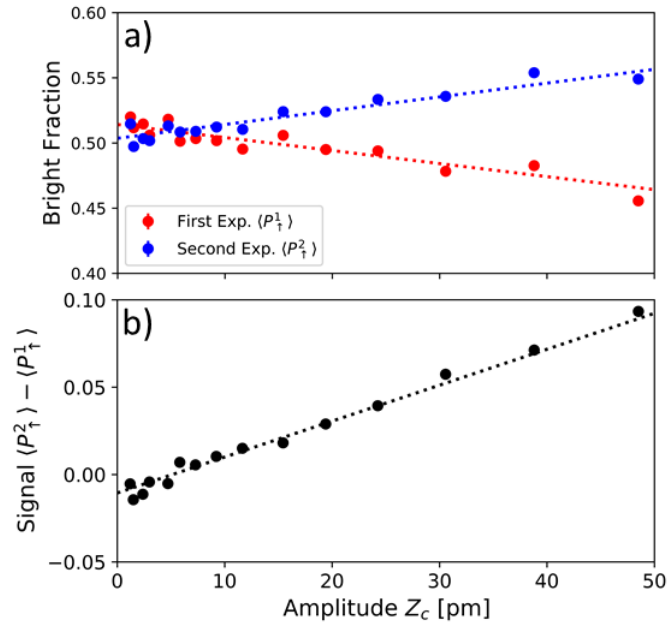
Figure 6.27: a) Symbols show the measured bright fraction for the first $P_\uparrow^1$ ($\delta = 0$) and second $P_\uparrow^2$ ($\delta = \pi$) sensing experiments. The scatter of these points around a linear fit (dashed lines) reflects the change in the background offset between successive experimental trials. b) This scatter is reduced by using the difference in the two experiments as the experimental signal. However, an offset in the background of approximately 2% remains. The error bars represent one standard deviation of uncertainty and are comparable to the symbol size.

use of a spin-dependent force, produced by an optical dipole force, to couple the spin and motional degrees of freedom of the ions. With such an interaction, it is possible to map the motion of the ions on to their spins, which can be read out with a precision set by projection noise and photon scattering. In addition to providing reasonably good force and electric field sensitivity, these experiments are useful in that they set a lower bound on the displacement amplitudes that can be measured with a particular protocol, even when the protocol is applied on resonance with the COM mode. Thus, this chapter serves as documentation of the calibration of the measurement imprecision of our protocol in the absence of thermal noise and back action.

The first experiment [18] was performed without control of the relative phase between the ODF and the classical drive. The result was the detection of a displacement of 500 pm with a single measurement signal-to-noise of 1. The 50 pm amplitude detected in Fig. 6.14 at a frequency ω far from resonance corresponds to an electric field detection of 0.46 mV/m or 73 yN/ion. By stabilizing this relative phase, an enhancement in sensitivity was achieved [19] by using a phase coherent protocol that allows for repeatedly measuring the same quadrature of motion. This resulted in an order of magnitude smaller displacement measured with SNR = 1. Further improvements can be made by increasing the ratio $\xi = \Gamma/(U/\hbar)$, either by reducing spontaneous decay (not possible in this current setup) or increasing U relative to Γ by way of, for example, parametric amplification (8.2).

This improvement has also opened the door for additional experiments - now performed resonantly with the COM mode. Probing on resonance with a measurement imprecision below z_{ZPT} (where z_{ZPT} is the amplitude of the zero point motion) will be sensitive to thermal fluctuations and back action due to spin-motion entanglement [12]. This motivates the investigation of potential back-action-evading protocols with trapped ion set-ups. For the phase coherent measurement of a single quadrature, back action due to spin-motion entanglement can be evaded through the introduction of the appropriate correlations between spin and motion [64]. The advantage of probing on resonance with the COM mode is that a significantly weaker electric field may ring up over time the same minimal displacement detectable here. Thus, a large improvement in the sensitivity to

electric fields is expected. The following chapter details experiments documenting this enhanced sensitivity to electric fields and further exploration of the quantum limits of amplitude and electric field sensing.

Chapter 7

Amplitude and electric field sensing resonant with the center-of-mass mode

In this chapter, recent experimental results for sensing displacement amplitudes excited by electric fields resonant with the COM mode will be discussed. These results build on the work described in Ch. 6 as well as references [18, 19].

7.1 Overview

In this chapter we experimentally and theoretically analyze a protocol for sensing small displacements of a single bosonic mode of a two-dimensional, trapped-ion crystal of ∼100 ions. We demonstrate a sensitivity beyond the standard quantum limit (SQL), defined as the precision with which a displacement could be measured with a coherent state.

This result builds upon previous work performed far detuned from the COM mode [18] and relies upon recent stabilization of the optical phase [19]. In the far-detuned limit [19], we measure displacement amplitudes limited by projection noise and photon scattering due to the off-resonant lasers used to produce $\hat{H}_{\mathrm{ODF}}$. In this off-resonance regime, our experimentally measured sensitivity of 29 dB smaller than the ground-state wavefunction extent represents the maximal achievable displacement amplitude sensitivity for the current experimental parameters. To reach the ultimate limits of electric field sensing, it is necessary to perform this measurement resonantly with the COM mode. The sensitivity to electric fields can in principle be increased by order the quality factor of the mode ($\sim 10^6$), although on-resonance with the COM mode thermal noise and back-action will limit the sensitivity to displacements. We demonstrate a sensitivity to displacements

resonant with the COM mode that is 7 dB below the SQL for displacement sensing, resulting in a displacement sensitivity of 60 pm/$\sqrt{\text{Hz}}$. For sensing amplitudes resulting from a field resonantly driving the COM mode, the SQL is just the ground state wave function extent, which is the minimum amplitude detectable with a coherent state. In addition, we assess the sensitivity of our protocol to electric fields and compare this to a classical benchmark. The quantum enhanced protocol is experimentally bench-marked at 3 dB below the SQL for a time-dependent amplitude, with an electric field sensitivity of 250 $\frac{\text{nV}}{\text{m}}$/$\sqrt{\text{Hz}}$. Since an electric field produces a signal (an amplitude of motion) that increases with driving duration T, the SQL depends on T. Some of the best RF electric field sensors are Rydberg atoms [74]. With these systems, it is possible to generate entangled states to beat the SQL [75] and reach sensitivities approaching 100 $\frac{\mu\text{V}}{\text{m}}$/$\sqrt{\text{Hz}}$ [76]. Such sensors demonstrate a broad bandwidth of sensitivity [74] and can be useful as an accurate standard [77].

7.2   On-resonance amplitude sensing

To measure a displacement of the ion crystal, we couple the spin and bosonic degrees of freedom of the ion crystal via the Hamiltonian:

$$\hat{H}_{ODF} = \frac{g_0}{\sqrt{N}} \left(\hat{a} + \hat{a}^\dagger \right) \hat{S}_z + \delta \hat{a}^\dagger \hat{a}, \tag{7.1}$$

where g_0 is the coupling strength and δ is the detuning of the spin-dependent force from the center-of-mass (COM) mode. With $\delta = 0$, this interaction drives spin-dependent displacements (see Fig. 7.1). To decouple from the thermal noise, zero-point motion, and back-action associated with resonantly driving the COM mode with a spin-dependent force, this interaction can be reversed by setting $g_0 = -g_0$ (more accurately, performing a spin rotation such that $|\uparrow\rangle \rightarrow |\downarrow\rangle$). With the application of a spin-independent drive between the two applications of $\hat{H}_{ODF}$, a measurement of the displacement of the COM mode limited only by projection noise and spin dephasing effects can - in principle - be made. Effectively, this protocol [78, 64] traces out an area in the phase-
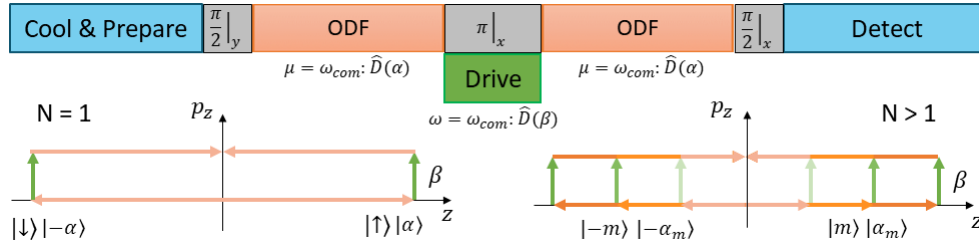
Figure 7.1: Illustration of protocol used for sensing displacement β. The ions are first Doppler cooled and optically pumped into the $|\uparrow\rangle$ state. A microwave $\pi/2$ pulse aligns the spins along the $\hat{x}$-axis. Application of the ODF for a duration τ with frequency $\mu = \omega_{com}$ drives a spin-dependent displacement. The π-pulse in the middle of the sequence flips up to down, allowing for cancellation of spin precession accumulated during the first ODF arm. Simultaneously, a weak drive is applied to an endcap electrode at frequency $\omega = \omega_{com}$ driving a spin-independent displacement. A second application of the ODF at the same frequency μ cancels the signal accumulated in the first arm and maps the spin-independent displacement onto the spins. A second $\pi/2$ pulse maps the spin precession accumulated either into spin population with a rotation about $\hat{x}$ (as shown) or into contrast with a rotation about $\hat{y}$ (not shown). Finally, the spin state is read out via a projective measurement.

space of the COM mode, as illustrated (along with the sequence) in Fig. 7.1. In the absence of a spin-independent force (the quantity to be measured), the return of the motional wavepacket to the phase-space origin indicates a disentangling of the spin and motional degrees of freedom. As a result of the decoupling of the spin and motion, the spins are ideally insensitive to the thermal noise and zero-point motion. The generation of spin-phonon entanglement is what gives this protocol its sensitivity, but making measurements of this entangled state is challenging, as it would involve measuring both the spin and phonon degrees of freedom. Reversing the spin-dependent force allows for a simpler measurement of just the spins. An alternative physical picture is that application of $\hat{H}_{\mathrm{ODF}}$ resonant with some motion induces a shift in the qubit frequency and results in precession of the collective Bloch vector, analogous to the optomechanical frequency shift of a cavity mode. Changing the sign of the spin-dependent force flips the direction of the spin precession, and so in this protocol the second application of the ODF cancels the spin precession due to thermal noise and zero-point motion of the mode. Frequency fluctuations of the COM mode will also impact the achievable sensitivity. For the current experiment, the frequency stability of the COM mode is the dominant - though not fundamental - limitation.

We use a Penning trap to confine and control single-plane Coulomb crystals of $N{\sim}100$ Be$^+$ ions, as described in [11, 12, 14], as well as Chs. 2 and 3. The motion of the ion crystal can be treated as $2N$ in-plane modes and N axial modes characterized by the center-of-mass mode frequency at $\omega_z/(2\pi) = 1.59$ MHz. The $^2S_{1/2}$ ground-state valence electron spin $|\uparrow\rangle\,(|\downarrow\rangle) \equiv |m_J = +1/2\rangle\,(|m_J = -1/2\rangle)$ is the spin-1/2 degree of freedom with a frequency splitting of 124 GHz. A resonant microwave source is used to perform global rotations of the spin ensemble. To couple the spin and motional degrees of freedom, a spin-dependent force is produced by interfering a pair of off-resonant (detuned from the nearest optical transitions by $\sim$20 GHz) laser beams to form a one-dimensional (1D) traveling-wave potential. The resulting light shifts produce a spin-dependent optical-dipole force (ODF) with a frequency μ. With this frequency tuned to near the COM mode, i.e. $\delta = \mu - \omega_z \approx 0$, the spin-dependent force drives spin-dependent displacements. We initialize the system with Doppler cooling and optical pumping to prepare the state state $|\uparrow\rangle_N \equiv |\uparrow\uparrow\cdots\uparrow\rangle$. Readout is performed with a projective global measurement of state-dependent fluorescence on the Doppler cooling transition, where spin $|\uparrow\rangle\,(|\downarrow\rangle)$ is bright (dark).

Figure 7.1 illustrates the experimental sequence. After preparing the ions in the state $|\uparrow\rangle_N$, a microwave $\pi/2$ pulse rotates the spins to align along $\hat{x}$ such that $|\psi(0)\rangle = |0\rangle_{ph} \otimes |(N/2)_x\rangle$. For simplicity we assume the ions begin in the motional ground state such that the COM mode phonon occupation $\bar{n} = 0$. Next, $\hat{H}_{\rm ODF}$ is applied for duration τ such that $|\psi(\tau)\rangle \equiv \hat{D}_{SD}(\alpha_0)|\psi(0)\rangle$, creating the state

$$|\psi(\tau)\rangle = \sum_{m=-N/2}^{N/2} c_m |\alpha_m\rangle_{ph} \otimes |m\rangle, \tag{7.2}$$

where $\hat{D}_{SD}(\alpha_0) = e^{(\alpha_0\hat{a}^\dagger - \alpha_0^\star\hat{a})\hat{S}_z}$ with $\alpha_0 = g_0\tau/\sqrt{N}$, c_m are the coefficients of the initial coherent spin state in the z-basis, $\alpha_m = m\alpha_0$, and $\hat{S}_z|m\rangle = m|m\rangle$. Note, Eq. 7.2 is derived within the Lamb-Dicke limit, i.e. it assumes the ions have an axial extent that is small compared to the wavelength of the traveling wave optical potential that produces $\hat{H}_{\rm ODF}$. A small coherent displacement β is achieved by applying a calibrated AC voltage to an endcap electrode (see Sec. 6.4 and Fig. 6.10),

producing an oscillating electric field with a frequency matched to the COM mode. With the proper choice of phase, this spin-independent displacement is orthogonal to the initial separation of the bosonic state with $\hat{U}_\beta = e^{i\beta(\hat{a}+\hat{a}^\dagger)}$. To undo the spin-dependent displacement, we rotate the spins about the $\hat{x}$-axis by π such that $|\uparrow\rangle \to |\downarrow\rangle$ and vice versa, and then reapply $\hat{H}_{\mathrm{ODF}}$ with $\delta = 0$. With $|\psi(2\tau)\rangle \equiv \hat{D}_{SD}(\alpha_0)\hat{R}_x(\pi)\hat{U}_\beta |\psi(\tau)\rangle$, the resulting state is

$$|\psi(2\tau)\rangle = \sum_{m=-N/2}^{N/2} c_m e^{2i\beta\alpha_m} |\beta\rangle_{ph} \otimes |-m\rangle. \tag{7.3}$$

The displacement β can be estimated by measuring the observable $\hat{S}_y$, which is accomplished by rotating the spins about the $\hat{x}$-axis by $\pi/2$ and making a projective measurement in the z-basis. The measured signal is $< S_y >= (N/2)e^{-2\Gamma\tau}\sin(\theta_m)$ where $\theta_m = 2\alpha_0\beta$.

We perform this experiment with a relative phase shift of π in the applied spin-independent force between pairs of measurements and take the difference of these results to subtract background offsets or common mode noise from shot-to-shot. The optical phase must be stabilized [19] (Sec. 6.5.1) and drifts compensated for by regular calibrations to maintain the orthogonality between $\hat{U}_\beta$ and $\hat{D}_{SD}(\alpha_0)$. We estimate the relative phase is maintained within 5 degrees over the course of a single application of the experimental sequence (see Sec. 6.5.1). The experiments are performed only with Doppler cooling such that the ions are prepared in a thermal state with $\bar{n} \approx 5$. EIT cooling, which can allow for near ground state cooling of the axial modes (see Sec. 5), was not used because it was experimentally observed to worsen the frequency fluctuations of the COM mode. This is thought to be caused by heating of the in-plane modes of the ion crystal due to imperfect alignment of the EIT cooling beams, which can give rise to axial mode frequency instabilities [28]. The protocol described in this section and illustrated in Fig. 7.1 remains valid regardless of whether the ions are initialized in their motional ground state or a thermal state. However, the case $\bar{n} \neq 0$ does result in some modification of the theoretical expressions used to compare with experiment outcomes, and will be discussed later in this chapter.

Prior to performing measurements, a pair of calibration experiments are used to ascertain

both the COM mode frequency as well as the phase of the ODF at the ions. Due to slow conversion of Be^+ to BeH^+ (from residual background hydrogen gas) and possibly rearrangements of the ion crystal, the COM mode frequency can vary and it is necessary to periodically and precisely measure its frequency. Figure 7.2 is an example of a typical calibrating scan of a moderately large amplitude RF drive applied for several ms (a 'tickle') to an endcap electrode with a frequency that is varied across the COM mode. When the COM mode is excited, the increased motional amplitude due to the driven motion causes a reduction in the number of photons collected during detection with the Doppler cooling laser. Fitting to this feature gives a value of the COM mode frequency with resolution of 10s of Hz. To calibrate the relative phase between the ODF and the classical drive, the initial phase of the ODF is varied and the resulting oscillation is fit to in order to extract the phase offset that results in both fields being in-phase. Figure 7.3 is an example of such a scan over the phase.

7.3   Understanding contributions to experimental noise

Prior to extracting the limiting sensitivity of the experimental measurement, the background noise must be fully understood and explained. The sources can be broken down into effects independent of the COM mode and those that arise due to the presence of the mode. We have characterized the measurement imprecision of our technique in a regime free from thermal effects and back-action [19] and have found our sensitivity to be limited by spin dephasing due to photon scattering, projection noise, and some residual technical noise. Performing this measurement resonantly with the COM mode means motional thermal noise, zero point motion, and back-action effects will be present.

Figure 7.4 represents a study of the COM mode lineshape (Fig. 7.4 (a) & (b) for the case of no spin-independent displacement. We characterize the contributions in Fig. 7.4 for both the case in which the noise processes add (Fig. 7.4 (a), with no reversal of the spin-dependent displacement) and in which they are canceled (Fig. 7.4 (b)). In Fig 7.4 (a), the frequency of the spin-dependent force is swept across the COM mode resulting in a characteristic lineshape. Here the final $\pi/2$
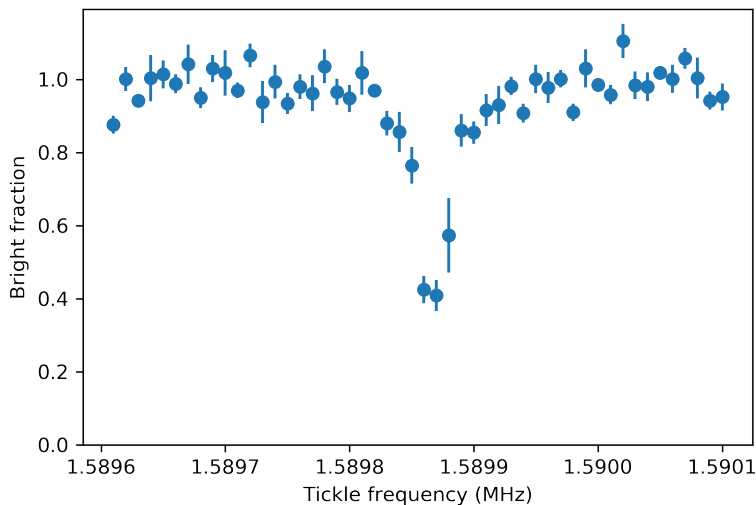
Figure 7.2: Calibration of COM mode frequency via RF tickle. An RF drive excites the COM mode and the resulting increase in the amplitude of motion causes a decrease in fluorescence from the Doppler cooling laser used for detection.
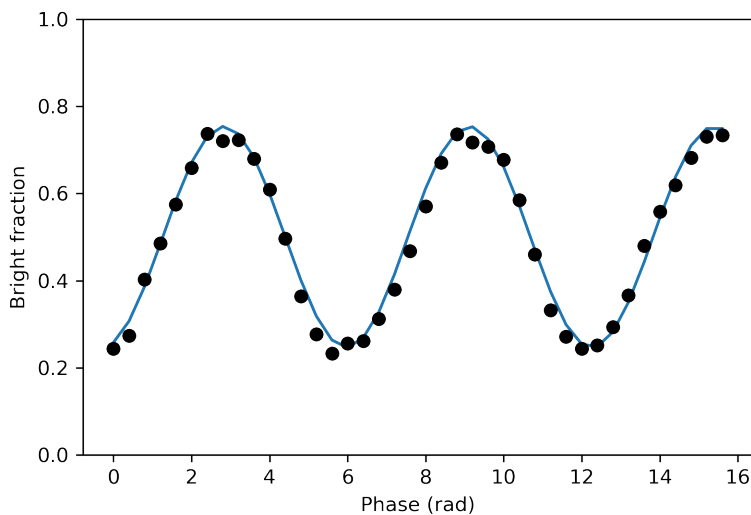
Figure 7.3: Experimental signal used to set the phase of the ODF relative to the phase of the spin-independent rf tickle. Here the same sequence is employed as that used for measuring a displacement amplitude of the ion crystal (Fig. 7.1), but with a moderately large spin-independent drive applied while the phase of the ODF is varied. This enables extracting the phase offset necessary for the ODF to be in-phase with the classical drive.
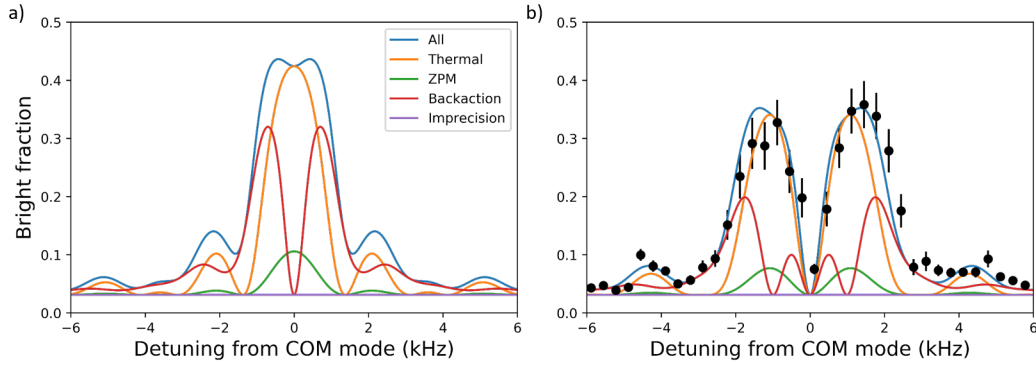
Figure 7.4: (a) Theory showing the lineshape of the center of mass mode *without* the π-pulse in the middle of the sequence and with the final π/2 pulse about y (no signal would result in a bright fraction of 0). The purple curve is the measurement imprecision / background set by photon scattering, green is the zero-point motion, red is the induced spin-spin interaction (back-action), orange is the thermal motion, and blue is all effects together. (b) Theory showing the lineshape of the COM mode *with* the π-pulse. Colors are the same as in (a). Black points are experimental data. Theory parameters in both (a) and (b) are taken from independent measurements. Note the lack of signal in (b) exactly at the COM mode frequency.
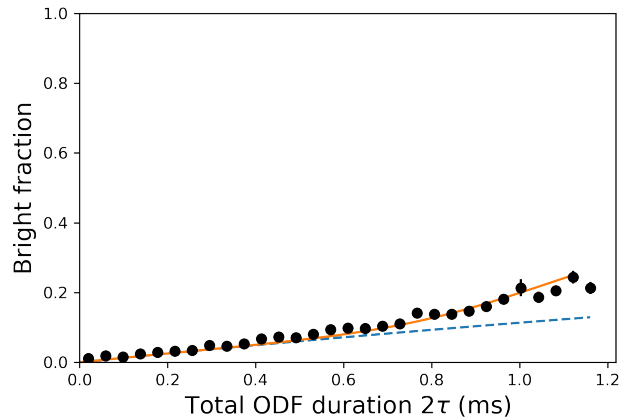
Figure 7.5: Measurement of COM frequency fluctuations by nominally setting $\delta = 0$ and measuring the increase of $< P_\uparrow >$ above the expectation from spin dephasing as a function of the protocol duration. The orange line is a fit to the data (black points), yielding rms frequency fluctuations of $\sigma/(2\pi) = 30$ Hz. The blue dashed line is theory including only spin dephasing due to photon scattering.

pulse is about $\hat{y}$ such that the spins lie in the $y - z$ plane and a projective measurement of the Bloch vector length $|< \vec{S} >|$ is performed, plotted in Fig. 7.4 in terms of the bright fraction $< P_\uparrow > = \frac{1}{2}(1 - |< \vec{S} >|)$. The background signal away from the mode is set by spin dephasing due to photon scattering from the off-resonant ODF lasers (Sec. 4.4.2). The zero-point motion contributes at a similar level, and both this and the thermal motion produce a signal due to spin dephasing resulting from an effective shift in the qubit frequency when $\hat{H}_{\mathrm{ODF}}$ is applied and μ is equal to a motional frequency of the ions [12, 18]. Finally, there is the contribution due to spin-spin interactions. These spin-spin interactions generate spin squeezing when $\delta \neq 0$, which is a form of back-action as it leads to a shortening of the Bloch vector. As the mode occupation is reduced to zero, only the thermal noise is reduced - the other sources of noise remain the same. By reversing the spin-dependent displacement with the application of a π pulse in the middle of the sequence, spin noise due to thermal and zero-point motion as well as back-action effects can be canceled on resonance (Fig. 7.4 (b), $\delta = 0$).

However, if the COM mode frequency changes from one experimental trial to the next, this cancellation will be imperfect. We characterize this effect by measuring $< P_\uparrow >$ with $\delta = 0$ while varying the duration of the ODF (Fig. 7.5). Frequency fluctuations of the COM mode will result in the bright fraction $< P_\uparrow >$ increasing above the expected background due to photon scattering. By fitting to the increase in background, the amplitude of frequency fluctuations can be estimated. Typically, the rms amplitude of frequency fluctuations is $\sigma/(2\pi) \approx 40 \pm 20$ Hz.

Another potential source of noise is damping of the COM mode. This might occur by energy transfer out of the COM mode and to the other axial or in-plane modes. To assess whether this is an issue for this experiment, we perform a ring down experiment wherein a large coherent motion is excited by a drive applied to an endcap electrode and the excited COM mode amplitude is subsequently measured following a variable wait duration. The amplitude of the motion is calibrated to be $Z_c \approx 50$ nm, about an order of magnitude larger than the thermal axial extent of the COM mode $z_{\mathrm{cm}} = \sqrt{\frac{\hbar}{2Nm_{\mathrm{Be}}\omega_z}(2\bar{n} + 1)} = 5.5$ nm, with $N = 120$, $\omega_z/(2\pi) = 1.59$ MHz, and $\bar{n} = 4.6$. The motion is read out by mapping it onto the spin state with a spin-dependent ODF and
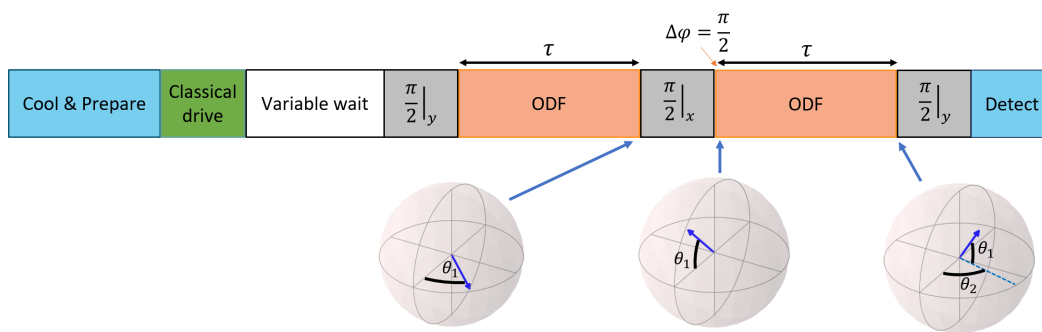
Figure 7.6: Experimental ring down sequence for quantifying the damping of the COM mode. After cooling and preparing the spins in the $|\uparrow\rangle$ state, a large coherent motional displacement is driven up with an RF drive applied to a trap electrode. Following a variable wait duration, the motion of the COM mode is read out. Here, the rms sum of both quadratures of the motion is measured by performing a $\pi/2$ spin rotation in the middle of the sequence, followed by a $\pi/2$ shift in the ODF phase.
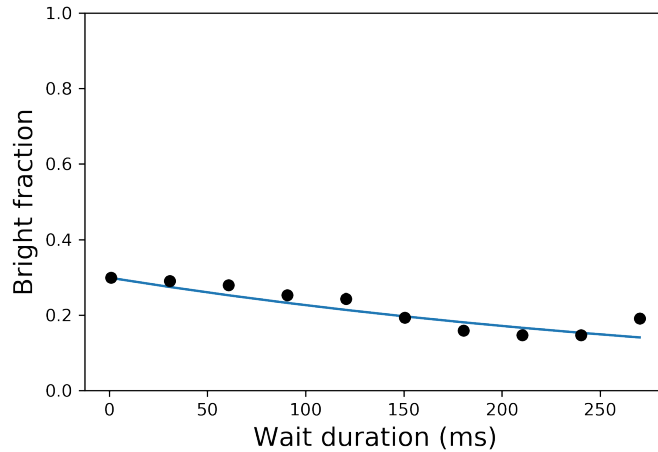
Figure 7.7: Experimental data for the ring down sequence described in the text and in Fig 7.6. An exponential decay is fit to the data and yields a decay rate of $\kappa = 1/(300\,\mathrm{ms})$.

performing a projective measurement of the spins. The relative phase of the driven motion relative to the ODF is left uncontrolled and varies randomly from shot-to-shot of the experiment (see [18] and Sec. 6.4). The protocol used in [18] and Sec. 6.4 measures a single quadrature of the motion, but for this case we would like to measure both quadratures so that the sensitivity to the relative phase ϕ is removed and the signal-to-noise ratio is not limited by fluctuations in ϕ (Fig. 6.14). Note that the signal is sensitive to the rms sum of the spin precession in each arm of the sequence. Figure 7.6 illustrates the sequence used. By applying a $\pi/2$ rotation about the x-axis in the middle of the sequence followed by a $\pi/2$ phase shift of the ODF, both quadratures are mapped into rotations of the spins: $\theta_1 = \theta_{\max} \cos(\phi)$ and $\theta_2 = \theta_{\max} \sin(\phi)$, where $\theta_{\max} = F_0 Z_c \tau \hbar$ with τ the duration of each ODF arm. The signal, then, is $\langle P_\uparrow \rangle = \frac{1}{2}\left[1 - e^{-\Gamma 2\tau} \langle \cos(\theta_1)\cos(\theta_2)\rangle\right] \approx \frac{1}{2}\left[1 - e^{-\Gamma 2\tau} \cos(\theta_{\max})\right]$, where this approximation is valid for small angles. Figure 7.7 shows the results of an experiment where the previously described sequence is applied and the wait duration following excitation of the COM mode is varied. Typically, no reduction in the signal is observed for over 100 ms. By fitting to this data with an exponential decay, a value of $1/\kappa = 300$ ms is extracted, where κ is the exponential decay rate.

Theoretical modeling suggests that upon including the dominant contribution from COM fre-

quency fluctuations, we can neglect both spin dephasing and damping of the COM mode. Though both dephasing due to photon scattering and damping of the COM mode are experimental limitations, they contribute roughly equally and are dwarfed by the frequency fluctuations of the COM mode.

7.4   Sensing small amplitudes of motion

Having characterized background noise and performed necessary calibrations, we move forward with measuring small displacement amplitudes of the ion crystal and analyzing the sensitivity of our protocol. We begin by assessing the the sensitivity to small amplitudes of motion. To do this, we apply a weak drive resonant with the COM mode for a short duration $t_{\text{drive}} = t_\pi = 44.4\ \mu\text{s}$, as illustrated in Fig. 7.1.

To assess the measured signal-to-noise ratio and compare to theory (see Fig. 7.8), we vary the amplitude of the spin-independent displacement β. We relate the unitless parameter β to a displacement Z_c through $\beta = Z_c\sqrt{N}/(2z_0)$, where $z_0 = \sqrt{\hbar/(2mw_z)}$ is the ground state wavefunction size for a single ion and $Z_c = F_D t_{\text{drive}}/(2m_{Be}w_z)$ is the zero-to-peak amplitude of the COM motion after a drive interval t_{drive} with a force per ion F_D. We determine the displacement amplitude Z_c through an independent calibration of the electric field generated through the application of a static voltage offset applied to a trap electrode [18, 19]. The force applied to an ion, then, is $F_D = (\Delta z)m_{Be}w_z^2$, where Δz is the displacement due to a static electric field. The signal-to-noise ratio for a single experiment $Z_c/\delta Z_c \equiv \theta_m/\delta\theta_m$ is extracted by repeatedly measuring S_y. We take the difference between pairs of subsequent measurements with a π phase shift in the amplitude β such that $S_y^1 = -S_y^2 = (N/2)e^{-2\Gamma\tau}\sin(\theta_m)$. For small angles, $\theta_m = (e^{2\Gamma\tau}/N)(S_y^2 - S_y^1)$ and so

$$\delta\theta_m = (1/N)\sqrt{(\Delta S_y^1)^2 + (\Delta S_y^2)^2}/\cos(\theta_m), \tag{7.4}$$

with $(\Delta S_y^1)^2 = (\Delta S_y^2)^2 = (N/4)\cos^2(\theta_m)$. Plugging in the expressions for the variances into the Eq. 7.4 and recalling the angle of spin precession to be measured is $\theta_m = 2\alpha_0\beta$ with $\alpha = g_0\tau/\sqrt{N}$, the signal-to-noise ratio for a pair of measurements is $Z_c/\delta Z_c = 2\sqrt{2}\beta g_0\tau e^{-2\Gamma\tau}$. For the

experiments described here, $g_0/(2\pi) = 3.7$ kHz parameterizes the strength of the spin-dependent force. The corresponding decay rate due to spin dephasing from off-resonant photon scattering is $\Gamma = 290$ s^{-1}. The value of g_0 is determined through independent calibration, as $g_0 = \sqrt{2\bar{J}\delta}$ where $\bar{J} = F_0^2/(4\hbar m_{Be}\omega_z\delta)$ is the homogenous all-to-all coupling between the spins (see Sec. 4.2.2) and $\delta = \mu - \omega_z$ is the detuning of the ODF from the COM mode. Including the dominant source of noise - COM mode frequency fluctuations - and neglecting damping of the COM mode, the resulting expression is [79]

$$\frac{Z_c}{\delta Z_c}\Big|_{\text{single}} = \frac{2\beta g_0\tau e^{-2\Gamma\tau}}{\sqrt{1 + (2\bar{n} + 1)g_0^2\sigma^2\tau^4 + \frac{4}{9}g_0^4\sigma^2\tau^6}}, \tag{7.5}$$

where we define the signal-to-noise ratio of a single measurement as $Z_c/\delta Z_c|_{\text{single}} = \frac{1}{\sqrt{2}}Z_c/\delta Z_c$, and σ is the amplitude of the rms frequency fluctuations. To extract the single measurement signal-to-noise, the signal is divided by 2 and the noise is divided by $\sqrt{2}$, such that the signal-to-noise is reduced by $\sqrt{2}$. In addition, Eq. 7.5 includes the contribution of the initial thermal state. Typically, $\bar{n} \approx 5$ following Doppler cooling. Note that this term (the second in the denominator) is relevant only when the COM mode frequency is unstable (i.e. $\sigma \neq 0$).

Figure 7.8 shows the experimental signal-to-noise ratio for a single measurement compared to theory. The signal-to-noise data is produced by taking the average of the difference $< S_y^1 > - < S_y^2 >$ in pairs of experiments, dividing by the standard deviation of all the data, and further dividing by $\sqrt{2}$ to produce the single measurement signal-to-noise ratio. For small angles θ_m,

$$\frac{Z_c}{\delta Z_c}\Big|_{\text{single,exp}} \approx \frac{< S_y^1 > - < S_y^2 >}{\sqrt{2}\ \sigma(S_y^1 - S_y^2)}. \tag{7.6}$$

We find good agreement between the data and theory that assumes COM mode frequency fluctuations within values determined experimentally. In addition, the signal-to-noise follows a linear trend to zero as the amplitude is reduced, demonstrating that there is no significant offset in this data due to effects other than the applied displacement amplitude.
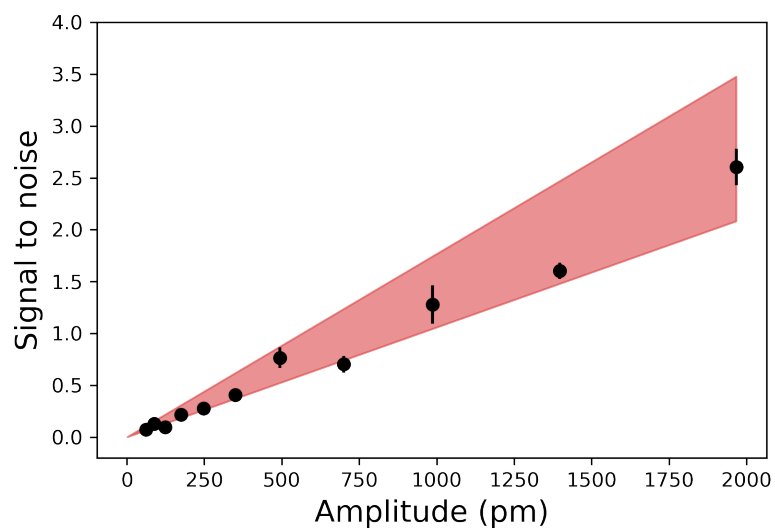
Figure 7.8: Signal-to-noise ratio versus displacement amplitude. The black points are measurements of the signal-to-noise ratio of a single measurement with statistical error bars. The arm duration is $\tau = 200\ \mu$s. The red shaded area represents theory for a range of COM mode frequency fluctuations, with an upper bound of $\sigma/(2\pi) = 80$ Hz and a lower bound of $\sigma/(2\pi) = 40$ Hz. In addition, the theory assumes a 18% increase in background noise above projection noise.
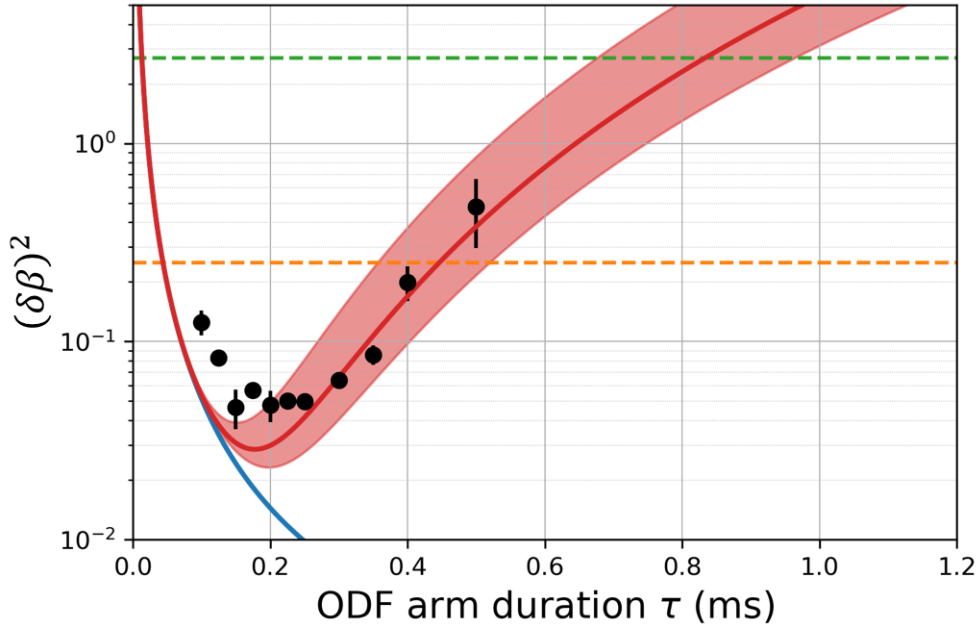
Figure 7.9: Sensitivity - in units of variance of the dimensionless displacement $(\delta\beta)^2$ - for the protocol as a function of the duration of one application of the ODF τ. Black points are experimental data with statistical error bars. The amplitude of the displacement is $Z_c = 990 \pm 100$ pm and the single measurement signal-to-noise is approximately 1. The solid blue line is the limiting sensitivity given only dephasing due to photon scattering, with $\Gamma = 290$ s^{-1}. The red shaded area represents the expected range of sensitivities for upper and lower bounds of COM mode frequency fluctuations: $\sigma/(2\pi) = 50$ Hz and a lower bound of $\sigma/(2\pi) = 30$ Hz, respectively. The red solid line is the average of the shaded area, with $\sigma/(2\pi) = 40$ Hz. The ODF coupling $g_0/(2\pi) = 3.7$ kHz is typical for the data in this chapter. In addition, all theory curves assume a 18% increase in background noise above projection noise. The dashed orange line is the SQL ($(\delta\beta)^2 = 1/4$, the ground state wavefunction extent), while the dashed green line is the size of the thermal fluctuations for the Doppler cooling limit ($(\delta\beta)^2 = (2\bar{n} + 1)/4$, $\bar{n} = 5$). The maximum experimental sensitivity to displacement is 7.2 dB below the SQL.

To compare the sensitivity of the protocol to the SQL, as well as confirm the role of frequency fluctuations, we vary the $\hat{H}_{\text{ODF}}$ interaction duration τ and plot data and theory in terms of the sensitivity $(\delta\beta)^2$, i.e. the variance of the dimensionless displacement β, in Fig. 7.9. In addition to providing a comparison to theory, this experiment allows for optimizing the duration of the ODF arms in the sequence, given the relevant parameters. The experiment is performed as previously described, but with varying arm duration. Experimentally, $(\delta\beta)^2$ is calculated from the determined signal-to-noise ratio for a single measurement of an amplitude Z_c through the expression

$$(\delta\beta)^2 = \frac{1}{4}\left(\frac{\sqrt{N}Z_c}{z_0 \frac{Z_c}{\delta Z_c}|_{\text{single}}}\right)^2 \tag{7.7}$$

where N is the number of ions and $z_0 = \sqrt{\hbar/2m_{Be}\omega_z}$. The theoretical expression for the sensitivity including dephasing due to photon scattering and noise due to frequency fluctuations of the COM mode is [79]

$$(\delta\beta)^2 = \frac{e^{-4\Gamma\tau}}{(2g_0\tau)^2} + \left(\frac{\sigma\tau}{2}\right)^2(2\bar{n}+1) + \left(\frac{g_0\sigma\tau^2}{3}\right)^2, \tag{7.8}$$

where σ is the value of the rms frequency fluctuations of the COM mode and τ is the ODF arm duration. Ideally, Eq. 7.8 would consist of only the first term, which represents projection noise plus spin dephasing from photon scattering. And, as was the case with Eq. 7.5, the nonzero occupation number for the COM mode $\bar{n}$ comes into play only because of the frequency fluctuations of the mode.

Figure 7.9 shows experimental data for the sensitivity as a function of ODF arm duration τ, as well as theory results for a range of COM mode frequency fluctuations corresponding to measured extreme values. To quantify the metrological utility of the described protocol, we compare to the SQL as defined by the quantum Fisher information: $(\delta\beta_{\text{SQL}})^2 = 0.25$ [80, 81, 82]. The Cramer-Rao bound for this protocol is $(\delta\beta)^2 \geq 1/(4 + 4g_0^2 t^2)$. Comparing our experimental results to the SQL, we determine a sensitivity to displacement amplitudes enhanced by 7.2 dB. This corresponds to a detection of a 660 pm displacement amplitude in a single shot with a signal-to-noise of 1. A

single experimental trial takes 8 ms, resulting in a sensitivity of 59 pm/$\sqrt{\text{Hz}}$. The driving field is applied for 44.4 μs, which corresponds to a measured sensitivity of 2.5 $\frac{\mu\text{V}}{\text{m}}/\sqrt{\text{Hz}}$. In addition, we compare to the case with no frequency fluctuations, including only spin dephasing due to photon scattering from the ODF beams. For the off-resonance sensing experiments in Ch. 6, this is the dominant experimental noise source. In this case, $(\delta\beta)^2 = e^{-4\Gamma\tau}/(2g_0\tau)^2$. Figure 7.10 depicts the off-resonance detection of a displacement amplitude $Z_c = 67$ pm in a single measurement with a signal-to-noise ratio of 1 as a variance of the unitless displacement β and compares this experimental result with the theoretical prediction assuming only projection noise and spin-dephasing due to photon scattering. The measured 67 pm displacement indicates that a measurement 29 dB smaller than the ground state wavefunction would be attainable if only spin dephasing due to photon scatter and projection noise were the relevant noise sources. Therefore, this amplitude detection provides a limit to the displacement sensitivity of the protocol described in this chapter for the case where $\sigma = 0$ and other noise sources are small compared to spin dephasing due to photon scattering.

7.5   Electric field sensing

Having quantified the limits of displacement amplitude sensing resonant with the COM mode, we can now investigate the limits of electric field sensing. For the ultimate electric field sensitivity, a very weak drive applied resonantly with the COM mode will ring up a minimal amplitude of motion over a long period of time. Ideally, this minimal displacement amplitude could be measured with the amplitude sensitivity previously demonstrated. Since this amplitude of motion is driven up over an extended period of time, the sensitivity of such a protocol to electric fields is greatly enhanced.

Just as the relative phase stability between the ODF and driving field and the COM mode frequency stability limit the amplitude sensitivity, these same noise sources will limit the sensitivity to electric fields. This section will address the theoretical treatment of this problem, outline the experimental protocol used, and detail the comparison between theoretical and experimental results. Of interest in this section, as was the case in the amplitude sensing section, is an analysis of the
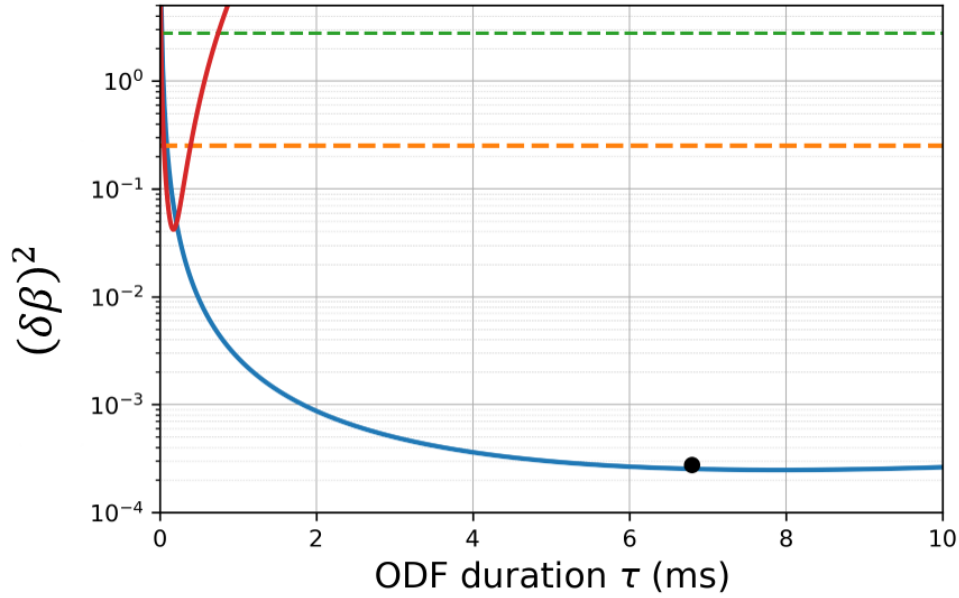
Figure 7.10: A reproduction of Fig. 7.9 including a data point from the off-resonance sensing results of Sec. 6.5. The red line is the same as in Fig. 7.9 and represents the theory prediction for the average value of COM mode frequency fluctuations $\sigma/(2\pi) = 40$ Hz. The blue line is also the same as in Fig. 7.9, though the values of $g_0/(2\pi) = 2.17$ kHz and $\Gamma = 126$ s^{-1} have been adjusted to match the experimental parameters from Sec. 6.5. The black point is an experimental detection of 67 pm with a single measurement signal-to-noise of 1 (statistical error bars are too small to see). The orange dashed line represents the extent of the ground state wavefunction, which is the SQL for measurements resonant with the COM mode. The green dashed line is the variance of the COM mode thermal fluctuations. On- and off-resonance theory curves (blue, red) assume an 18% and 25% increase in background noise above projection noise, respectively. The x-axis is the relevant duration of the ODF, τ. For the measurements in this chapter, this is one application of the ODF (see Fig. 7.1). However, for the results reproduced from Sec. 6.5, τ is the total duration the ODF is applied.
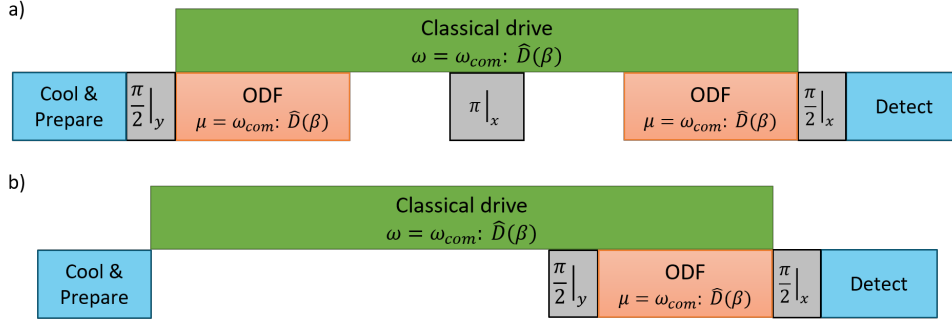
Figure 7.11: Illustration and comparison of two sequences used to assess the sensitivity to electric fields. The classical drive is applied for a duration T. Each ODF arm has a duration τ. a) Quantum protocol wherein a spin-dependent force entangles the spin and motional degrees of freedom with a spin-dependent displacement which is later reversed. The classical drive to be measured remains on through the sequence. b) Classical protocol wherein the classical drive is applied for the same duration as in the quantum protocol, but instead the ODF is turned on only at the end of the sequence to read out the excited amplitude of motion.

potential quantum enhancement. That is, we assess whether an experiment that uses quantum resources can outperform an experiment using classical resources only. In addition, we describe the relevant SQL and assess the performance of our experimental protocol relative to this limit.

A key difference in developing and assessing a protocol for measuring a parameter such as an electric field as opposed to a displacement is that applying the electric field for a longer period of time will increase the signal. As a result, both the sequence and the theoretical limits for measuring an electric field will be different. We define the parameter of interest β_0 by way of the unitless coherent displacement previously discussed $\beta = \beta_0 T$, where T is the time spent driving the amplitude up. The SQL, then, is redefined as $(\delta\beta_0)^2_{\text{SQL}} = 1/(4T^2)$ [80, 81, 82].

To maximize the duration over which the electric will ring up a displacement amplitude, we use a sequence where the classical drive is applied both during and between the two applications of the ODF arms, with each arm of duration τ. Figure 7.11 illustrates this sequence, where the ODF is on for a fraction of the driving duration with the optimal duration being determined with theoretical simulation. The limitation for the duration of application of the ODF is the frequency instability of the COM mode - as was the case in Sec. 7.2. The Hamiltonian in this case is slightly modified from 7.1, since the spin-independent drive is on simultaneously with the spin-dependent

drive:

$$\hat{H}_{ODF} = \frac{g_0}{\sqrt{N}} \left(\hat{a} + \hat{a}^\dagger \right) \hat{S}_z + \delta \hat{a}^\dagger \hat{a} + \beta_0 \left(\hat{a} + \hat{a}^\dagger \right). \tag{7.9}$$

The sequence illustrated in Fig. 7.11 a) uses quantum resources in the form of entanglement between the spin and motional degrees of freedom (by way of the applied spin-dependent force) and can be compared to the absolute SQL, $(\delta\beta_0)^2_{\text{SQL}}$. However, this SQL effectively assumes that the measurement of the displacement incurred after duration T is instantaneous. An alternative comparison would be to a 'classical' protocol that includes the non-zero measurement period. Figure 7.11 b) is such a classical protocol in which the driving field β_0 is applied for the same duration of duration T as in the 'quantum' protocol, but the ODF is only used as a readout of the amplitude after the classical drive excites motion over the course of the driving duration. For sufficiently long drive duration T, relevant for this experimental work, the theoretical expression characterizing the classical protocol approaches $(\delta\beta_0)^2_{\text{therm}} = (2\bar{n} + 1)(\delta\beta_0)^2_{\text{SQL}}$, which is the sensitivity limited by thermal fluctuations of the COM mode characterized by the occupation number $\bar{n}$. This classical protocol, then, serves as an effective SQL to compare the quantum protocol against.

Ideally, the sensitivity of the quantum protocol would be characterized by

$$(\delta\beta_0)^2_{\sigma=0} = \frac{1}{4g_0^2\tau^2(T-\tau)^2}. \tag{7.10}$$

However, frequency fluctuations of the COM mode again prove to be the dominant limitation to the experimental measurement. Including rms frequency fluctuations of the COM mode σ, the expression for the variance of the driven displacement is [79]

$$(\delta\beta_0)^2_{\text{quan}} = \frac{1}{4g_0^2\tau^2(T-\tau)^2} + \frac{g_0^2\sigma^2\tau^2(3T-4\tau)^2}{9(T-\tau)^2} + \frac{1}{4}\sigma^2(2\bar{n}+1). \tag{7.11}$$

Similarly, the previously described classical protocol will be impacted by the frequency instability of the COM mode. Again, the frequency fluctuations prove to be a dominant noise source and effects due to spin-dephasing can be neglected. However, in the classical protocol the spin precession

due to motional thermal noise is not canceled (the spin and motional degrees of freedom are not disentangled) and must be taken into account, which results in [79]

$$
\begin{aligned}
(\delta\beta_0)^2_{\text{class}} = {} & \frac{1}{g_0^2\tau^2(2T-\tau)^2} + \frac{2\bar{n}+1}{(2T-\tau)^2} + \frac{g_0^2\sigma^2\tau^4}{36(2T-\tau)^2} \\
& - \frac{\sigma^2(2\bar{n}+1)(3T^2-3T\tau+\tau^2)}{3(2T-\tau)^2} + \frac{1}{4}\sigma^2(2\bar{n}+1).
\end{aligned}
\tag{7.12}
$$

Figure 7.12 shows a comparison of theory and experiment for both the quantum and classical protocols. The optimal ODF duration τ is determined by numerically minimizing the expressions in Eqs. 7.11 and 7.12 for a given drive duration T and independently measured experimental parameters g_0, $\bar{n}$, and σ. In the currently accessible experimental regime, for intermediate driving duration T it is possible to surpass the SQL. Experimental results show that this protocol does surpass the SQL. With a drive duration $T = 0.5$ ms, the experimental result is 2.6 dB below the SQL. For a long drive duration $T = 1.1$ ms, the electric field detected with a signal-to-noise of 1 is ~ 2.6 μV/m, corresponding to a sensitivity of 250 nV/(m/$\sqrt{\text{Hz}}$) for a single measurement duration of $T_{\text{tot}} = 8.7$ ms. If we compare this protocol to the classical version, we see a ~ 14 dB improvement in sensitivity. Thus, there is a large increase in sensitivity relative to what is achievable with a comparable experiment that does not use quantum resources.

7.6 Summary and outlook

To summarize, this chapter has provided an overview of a pair of experiments intended to test the limits of sensing small displacements driven by electric fields resonant with the COM mode. In this regime, as opposed to the off-resonance regime described in Ch. 6, thermal noise and other noise sources related to the COM mode must be taken into account or mitigated. However, by applying and later reversing a spin-dependent displacement, the spin and phonon degrees of freedom are decoupled and the spin precession due to thermal noise can be canceled. Chief among the remaining sources of noise is the instability of the COM mode frequency, which is the dominant limitation to the sensitivity of the protocols described in this chapter.

The work described in this chapter involved both theory and experimental efforts to assess the
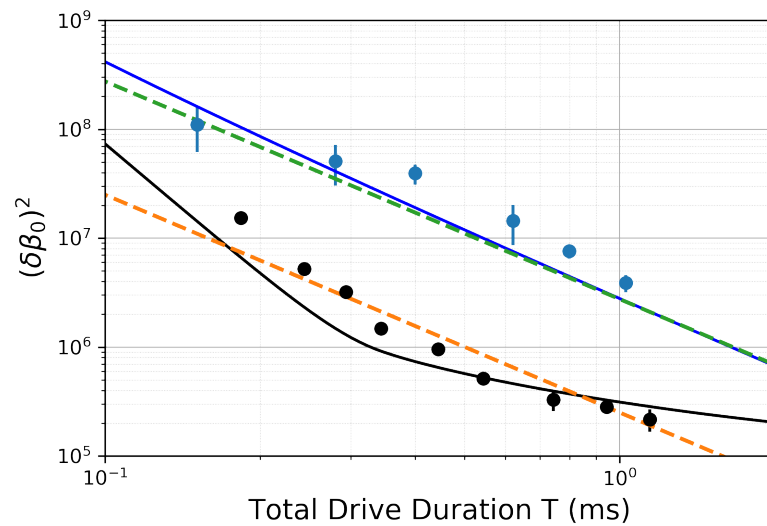
Figure 7.12: Sensitivity - in units of variance of displacement/time $(\delta\beta_0)^2$ - for both classical and quantum protocols (see Fig. 7.11) as a function of the total drive duration T. The blue points and line correspond to experimental data and theory comparison for the classical protocol. The black points and line correspond to experimental data and theory comparison for the quantum protocol. The orange dashed line is the SQL, while the green dashed line is the thermal limit (both described in the text). The theory assumes COM mode frequency fluctuations of $\sigma/(2\pi) = 40$ Hz. Relative to the classical experiment, the quantum experiment performs 14 dB better at the optimal point. The quantum experiment is optimally 2.6 dB below the SQL.

sensitivity of the chosen protocols to first displacement amplitudes (Sec. 7.2) and then electric fields (Sec. 7.5). We find that displacements ~ 7 dB smaller than the axial extent of the ground state wavefunction (and correspondingly, the SQL) can be detected in a single shot of the experiment, corresponding to a displacement sensitivity of 60 pm/$\sqrt{\text{Hz}}$. By applying the driving field for a longer period of time and ringing up an amplitude of motion, the sensitivity to electric fields is enhanced. By comparing a protocol that makes use of spin-motion entanglement to one that does not, we find an enhancement in sensitivity to electric fields of 14 dB. In addition, we can compare this quantum enhanced measurement to the SQL for a parameter driven over a period of time, and find that we surpass the SQL for electric field sensing by 2.6 dB. The resulting electric field sensitivity is 250 nV/(m/$\sqrt{\text{Hz}}$).

Chapter 8

Outlook and conclusion

In this thesis I have presented an overview of a series of experiments which have heightened the capabilities of the NIST Penning trap apparatus and pushed the limits of displacement and electric field sensing. Ground-state cooling of the axial drumhead modes of a two-dimensional crystal of over one hundred ions will enable a new generation of quantum experiments unhindered by the limitations imposed by thermal noise. Improvements made to the apparatus to achieve optical phase stabilization of the ODF beams also increase the prospects for future work, including the implementation of parametric amplification. Representing the culmination of a series of quantum sensing experiments documented here, the demonstrated sensitivity of the entanglement sensing protocol surpasses the standard quantum limit for both amplitude and electric field sensing. Possible extensions, applications, and improvements are discussed in what follows.

8.1 Dark matter

It is well known from astronomical observation that there is a great deal of matter currently invisible to us. The presence of this dark matter is inferred from observed gravitational effects which cannot be explain with current theories of gravity without including a great deal more matter than is observed. Though it is not known what might make up the dark matter, two related postulations are axions and hidden photons. Both of these proposed types of dark matter would have light masses and behave as classical fields, with a frequency set by the (unknown) mass of the particle and an amplitude set by its (also unknown) coupling to photons (for axions, this occurs only in the

presence of a magnetic field). As a result of these unknown values, a large parameter range exists and is currently being experimentally explored. Thus, devices sensitive to very weak electric fields may be useful for searching for dark matter.

Though a dark matter search is not currently underway at NIST with the Penning trap, it is a not-implausible extension of the work described in this thesis. With a current sensitivity to electric fields of $\sim 250~(\mathrm{nV/m})/\sqrt{\mathrm{Hz}}$, further improvements to the stability of the center-of-mass mode frequency may allow for sub-nV/m electric field detection in 1 second. Electric field sensing below ~ 1 nV/m enables searches for hidden-photon dark matter [83, 84, 85], although shielding effects must be carefully considered. Ion traps typically operate with frequencies $\omega_z/2\pi$ between 50 kHz and 5 MHz, providing a sensitivity to hidden-photon masses from 2×10^{-10} eV to 2×10^{-8} eV.

8.2 Enhancing the ODF: angle of incidence & parametric amplification

One of the fundamental limitations of all experiments performed with the NIST Penning trap is decoherence due to photon scattering from the off-resonant ODF lasers. Improving the ratio of the spin-dependent force to the spontaneous decay rate F_0/Γ would improve this limitation and allow for increasing the speed of interactions without the penalty of increased spin dephasing noise from the photon scattering (elastic Rayleigh scattering). This can result in improved fidelity of producing interesting entangled states [14, 15, 16] and increased sensitivity to electric fields [18, 19].

One method to do this is to increase the angle of incidence of the ODF beams at the ions from $\pm 10°$ to $\pm 20°$ (see Ch. 2.4.1). This involves replacing the in-bore mirrors used to reflect the beams onto the ions. However, doing so would reduce the effective wavelength of the running 1D optical lattice. If the ions are only Doppler cooled, this is problematic. With the implementation of EIT cooling, the near ground-state cooled ions will remain in the Lamb-Dicke regime despite this reduced ODF lattice wavelength. As a result, the magnitude F_0 of the spin-dependent optical-dipole force may be increased with no increase in the photon scattering rate Γ.
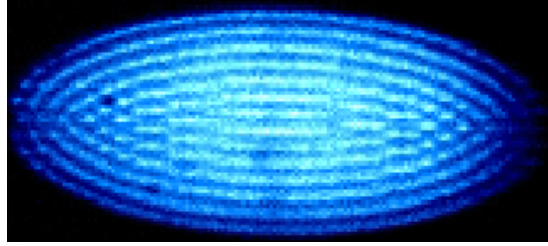
Figure 8.1: A view from the side of a 3D crystal of ions.

A second approach to increasing the ration F_0/Γ is to use parametric amplification to augment the strength of the ODF [73, 86]. Some preliminary work has been done on this front with the Penning trap, and it will be a high priority moving forward. Parametric amplification has been recently demonstrated in another trapped-ion experiment, where squeezed motional states were produced [66] and quantum gates sped up [87].

8.3   Three dimensional crystals

Though all the work summarized in this thesis made use of two-dimensional crystals of trapped ions, three-dimensional crystals of many hundreds to thousands of ions are routinely trapped and controlled in the NIST Penning trap. Increasing the number and dimension of ions used adds complexity as well as increased sensitivity to electric fields. Using the protocol described in Ch. 7, the sensitivity for detecting electric fields improves with the number of trapped ions, with $\sqrt{N}$ scaling. If future efforts can initialize the spins in an entangled state [14], this scaling may be improved. In particular, for a maximally entangled cat-state the Heisenberg limit is reached with a scaling of N [5, 16]. Controlling single-plane arrays of more than about 500 ions has been challenging, possibly because of the high density of modes. Multi-plane, three-dimensional crystals may get around these problems. With the appropriate setup [88] it may be possible to generate phase-coherent spin-dependent forces on three-dimensional ion crystals, where $N > 10^5$ ions are readily formed and controlled [89].

Bibliography

[1] C. L. Degen, F. Reinhard, and P. Cappellaro, "Quantum sensing," <u>Rev. Mod. Phys.</u>, vol. 89, p. 035002, Jul 2017.

[2] D. P. DiVincenzo, "The physical implementation of quantum computation," <u>Fortschritte der Physik</u>, vol. 48, pp. 771–783, 2000.

[3] N. F. Ramsey, "A molecular beam resonance method with separated oscillating fields," <u>Phys. Rev.</u>, vol. 78, pp. 695–699, Jun 1950.

[4] H. Lee, P. Kok, and J. P. Dowling, "A quantum rosetta stone for interferometry," <u>Journal of Modern Optics</u>, vol. 49, no. 14-15, pp. 2325–2338, 2002.

[5] J. J. . Bollinger, W. M. Itano, D. J. Wineland, and D. J. Heinzen, "Optimal frequency measurements with maximally correlated states," <u>Phys. Rev. A</u>, vol. 54, pp. R4649–R4652, Dec 1996.

[6] V. Giovannetti, S. Lloyd, and L. Maccone, "Quantum-enhanced measurements: Beating the standard quantum limit," <u>Science</u>, vol. 306, no. 5700, pp. 1330–1336, 2004.

[7] C. J. Ballance, T. P. Harty, N. M. Linke, M. A. Sepiol, and D. M. Lucas, "High-fidelity quantum logic gates using trapped-ion hyperfine qubits," <u>Phys. Rev. Lett.</u>, vol. 117, p. 060504, Aug 2016.

[8] J. P. Gaebler, T. R. Tan, Y. Lin, Y. Wan, R. Bowler, A. C. Keith, S. Glancy, K. Coakley, E. Knill, D. Leibfried, and D. J. Wineland, "High-fidelity universal gate set for $^9\text{Be}^+$ ion qubits," <u>Phys. Rev. Lett.</u>, vol. 117, p. 060505, Aug 2016.

[9] A. Friedenauer, H. Schmitz, J. T. Glueckert, D. Porras, and T. Schaetz, "Entanglement and tunable spin-spin couplings between trapped ions using multiple transverse modes," <u>Nature Physics</u>, vol. 4, pp. 757–761, 2008.

[10] K. Kim, M.-S. Chang, R. Islam, S. Korenblit, L.-M. Duan, and C. Monroe, "Entanglement and tunable spin-spin couplings between trapped ions using multiple transverse modes," <u>Phys. Rev. Lett.</u>, vol. 103, p. 120502, Sep 2009.

[11] J. J. Bollinger, J. W. Britton, and B. C. Sawyer, "Simulating quantum magnetism with correlated non-neutral ion plasmas," <u>AIP Conference Proceedings</u>, vol. 1521, pp. 200–209, 2013.

[12] B. C. Sawyer, J. W. Britton, and J. J. Bollinger, "Spin dephasing as a probe of mode temperature, motional state distributions, and heating rates in a two-dimensional ion crystal," Phys. Rev. A, vol. 89, p. 033408, Mar 2014.

[13] J. W. Britton, B. C. Sawyer, A. C. Keith, C.-C. J. Wang, J. K. Freericks, H. Uys, M. J. Biercuk, and J. J. Bollinger, "Engineered two-dimensional Ising interactions in a trapped-ion quantum simulator with hundreds of spins," Nature, vol. 484, no. 7395, pp. 489–492, 2012.

[14] J. G. Bohnet, B. C. Sawyer, J. W. Britton, M. L. Wall, A. M. Rey, M. Foss-Feig, and J. J. Bollinger, "Quantum spin dynamics and entanglement generation with hundreds of trapped ions," Science, vol. 352, no. 6291, pp. 1297–1301, 2016.

[15] M. Gärttner, J. G. Bohnet, A. Safavi-Naini, M. L. Wall, J. J. Bollinger, and A. M. Rey, "Measuring out-of-time-order correlations and multiple quantum spectra in a trapped-ion quantum magnet," Nature Physics, vol. 13, p. 781, 2017.

[16] A. Safavi-Naini, R. J. Lewis-Swan, J. G. Bohnet, M. Gärttner, K. A. Gilmore, J. E. Jordan, J. Cohn, J. K. Freericks, A. M. Rey, and J. J. Bollinger, "Verification of a many-ion simulator of the dicke model through slow quenches across a phase transition," Phys. Rev. Lett., vol. 121, p. 040503, Jul 2018.

[17] E. Jordan, K. A. Gilmore, A. Shankar, A. Safavi-Naini, J. G. Bohnet, M. J. Holland, and J. J. Bollinger, "Near ground-state cooling of two-dimensional trapped-ion crystals with more than 100 ions," Phys. Rev. Lett., vol. 122, p. 053603, Feb 2019.

[18] K. A. Gilmore, J. G. Bohnet, B. C. Sawyer, J. W. Britton, and J. J. Bollinger, "Amplitude sensing below the zero-point fluctuations with a two-dimensional trapped-ion mechanical oscillator," Phys. Rev. Lett., vol. 118, p. 263602, Jun 2017.

[19] A. Shankar, C. Tang, M. Affolter, K. Gilmore, D. H. E. Dubin, S. Parker, M. J. Holland, and J. J. Bollinger, "Broadening of the drumhead-mode spectrum due to in-plane thermal fluctuations of two-dimensional trapped ion crystals in a penning trap," Phys. Rev. A, vol. 102, p. 053106, Nov 2020.

[20] L. S. Brown and G. Gabrielse, "Geonium theory: Physics of a single electron or ion in a penning trap," Rev. Mod. Phys., vol. 58, pp. 233–311, Jan 1986.

[21] X.-P. Huang, F. Anderegg, E. M. Hollmann, C. F. Driscoll, and T. M. O'Neil, "Steady-state confinement of non-neutral plasmas by rotating electric fields," Phys. Rev. Lett., vol. 78, pp. 875–878, Feb 1997.

[22] J. J. Bollinger, J. S. Wells, D. J. Wineland, and W. M. Itano, "Hyperfine structure of the $2p^2p_{\frac{1}{2}}$ state in ^{9}Be$^+$," Phys. Rev. A, vol. 31, pp. 2711–2714, Apr 1985.

[23] G. Breit and I. I. Rabi, "Measurement of nuclear spin," Phys. Rev., vol. 38, pp. 2082–2083, Dec 1931.

[24] N. Shiga, W. M. Itano, and J. J. Bollinger, "Diamagnetic correction to the ^{9}be$^+$ ground-state hyperfine constant," Phys. Rev. A, vol. 84, p. 012510, Jul 2011.

[25] M. J. Biercuk, H. Uys, A. P. Vandevender, N. Shiga, W. M. Itano, and J. J. Bollinger, "High-fidelity quantum control using ion crystals in a penning trap," Quantum Inf. Comput., vol. 9, pp. 920–949, 2009.

[26] W. M. Itano and D. J. Wineland, "Precision measurement of the ground-state hyperfine constant of ^{25}Mg$^+$," Phys. Rev. A, vol. 24, pp. 1364–1373, Sep 1981.

[27] S. B. Torrisi, J. W. Britton, J. G. Bohnet, and J. J. Bollinger, "Perpendicular laser cooling with a rotating-wall potential in a penning trap," Phys. Rev. A, vol. 93, p. 043421, Apr 2016.

[28] A. Shankar, C. Tang, M. Affolter, K. Gilmore, D. H. E. Dubin, S. Parker, M. J. Holland, and J. J. Bollinger, "Broadening of the drumhead-mode spectrum due to in-plane thermal fluctuations of two-dimensional trapped ion crystals in a penning trap," Phys. Rev. A, vol. 102, p. 053106, Nov 2020.

[29] D. J. Wineland, C. Monroe, W. M. Itano, D. Leibfried, B. E. King, and D. M. Meekhof, "Experimental Issues in Coherent Quantum-State Manipulation of Trapped Atomic Ions," Journal of Research of the National Institute of Standards and Technology, vol. 103, no. 103, p. 259, 1998.

[30] D. H. E. Dubin, "Structure of two-dimensional plasma crystals in anharmonic penning traps," Phys. Rev. A, vol. 88, p. 013403, Jul 2013.

[31] A. Kramida and W. C. Martin, "A compilation of energy levels and wavelengths for the spectrum of neutral beryllium (be i)," Journal of Physical and Chemical Reference Data, vol. 26, no. 5, pp. 1185–1194, 1997.

[32] A. C. Wilson, C. Ospelkaus, A. P. VanDevender, J. A. Mlynek, K. R. Brown, D. Liebfried, and D. J. Wineland, "A 750-mw, continuous-wave, solid-state laser source at 313 nm for cooling and manipulating trapped 9be+ ions," Applied Physics B, vol. 105, p. 741–748, 2011.

[33] Y. Lin, "Quantum entanglement generation in trapped ions using coherent and dissipative methods," PhD Thesis, 2015.

[34] D. Leibfried, B. DeMarco, V. Meyer, D. Lucas, M. Barrett, J. Britton, W. M. Itano, B. Jelenković, C. Langer, T. Rosenband, and D. J. Wineland, "Experimental demonstration of a robust, high-fidelity geometric two ion-qubit phase gate.," Nature, vol. 422, no. 6930, pp. 412–5, 2003.

[35] H. Uys, M. J. Biercuk, A. P. VanDevender, C. Ospelkaus, D. Meiser, R. Ozeri, and J. J. Bollinger, "Decoherence due to elastic Rayleigh scattering," Physical Review Letters, vol. 105, no. 20, p. 200401, 2010.

[36] J. W. Britton, J. G. Bohnet, B. C. Sawyer, H. Uys, M. J. Biercuk, and J. J. Bollinger, "Vibration-induced field fluctuations in a superconducting magnet," Phys. Rev. A, vol. 93, p. 062511, Jun 2016.

[37] B. C. Sawyer, J. W. Britton, A. C. Keith, C.-C. Joseph Wang, J. K. Freericks, H. Uys, M. J. Biercuk, and J. J. Bollinger, "Spectroscopy and Thermometry of Drumhead Modes in a Mesoscopic Trapped-Ion Crystal Using Entanglement," Physical Review Letters, vol. 108, no. 21, p. 213003, 2012.

[38] C.-C. J. Wang, A. C. Keith, and J. K. Freericks, "Phonon-mediated quantum spin simulator employing a planar ionic crystal in a penning trap," Phys. Rev. A, vol. 87, p. 013422, Jan 2013.

[39] J. J. Bollinger, D. J. Heinzen, F. L. Moore, W. M. Itano, D. J. Wineland, and D. H. E. Dubin, "Electrostatic modes of ion-trap plasmas," Phys. Rev. A, vol. 48, pp. 525–545, Jul 1993.

[40] D. J. Heinzen, J. J. Bollinger, F. L. Moore, W. M. Itano, and D. J. Wineland, "Rotational equilibria and low-order modes of a non-neutral ion plasma," Phys. Rev. Lett., vol. 66, pp. 2080–2083, Apr 1991.

[41] M. W. Anderson, T. M. O'Neil, D. H. E. Dubin, and R. W. Gould, "Degenerate mixing of plasma waves on cold, magnetized single-species plasmas," Physics of Plasmas, vol. 18, no. 10, p. 102113, 2011.

[42] A. Shankar, E. Jordan, K. A. Gilmore, A. Safavi-Naini, J. J. Bollinger, and M. J. Holland, "Modeling near ground-state cooling of two-dimensional ion crystals in a penning trap using electromagnetically induced transparency," Phys. Rev. A, vol. 99, p. 023409, Feb 2019.

[43] A. Shankar, "Tools for improved quantum metrology on atomic platforms," PhD Thesis, 2020.

[44] B. E. King, C. S. Wood, C. J. Myatt, Q. A. Turchette, D. Leibfried, W. M. Itano, C. Monroe, and D. J. Wineland, "Cooling the collective motion of trapped ions to initialize a quantum register," Phys. Rev. Lett., vol. 81, pp. 1525–1528, Aug 1998.

[45] G. Stutter, P. Hrmo, V. Jarlaud, M. K. Joshi, J. F. Goodwin, and R. C. Thompson, "Sideband cooling of small ion coulomb crystals in a penning trap," Journal of Modern Optics, vol. 65, no. 5-6, pp. 549–559, 2018.

[46] G. Morigi, J. Eschner, and C. H. Keitel, "Ground state laser cooling using electromagnetically induced transparency," Phys. Rev. Lett., vol. 85, pp. 4458–4461, Nov 2000.

[47] G. Morigi, "Cooling atomic motion with quantum interference," Phys. Rev. A, vol. 67, p. 033402, Mar 2003.

[48] C. F. Roos, D. Leibfried, A. Mundt, F. Schmidt-Kaler, J. Eschner, and R. Blatt, "Experimental demonstration of ground state laser cooling with electromagnetically induced transparency," Phys. Rev. Lett., vol. 85, pp. 5547–5550, Dec 2000.

[49] Y. Lin, J. P. Gaebler, T. R. Tan, R. Bowler, J. D. Jost, D. Leibfried, and D. J. Wineland, "Sympathetic electromagnetically-induced-transparency laser cooling of motional modes in an ion chain," Physical Review Letters, vol. 110, pp. 153002–1 – 153002–5, apr 2013.

[50] K. Xia and J. Evers, "Ground state cooling of a nanomechanical resonator in the nonresolved regime via quantum interference," Phys. Rev. Lett., vol. 103, p. 227203, Nov 2009.

[51] R. Lechner, C. Maier, C. Hempel, P. Jurcevic, B. P. Lanyon, T. Monz, M. Brownnutt, R. Blatt, and C. F. Roos, "Electromagnetically-induced-transparency ground-state cooling of long ion strings," Phys. Rev. A, vol. 93, p. 053401, May 2016.

[52] M. Qiao, Y. Wang, Z. Cai, B. Du, P. Wang, C. Luan, W. Chen, H.-R. Noh, and K. Kim, "Double-eit ground-state cooling of stationary two-dimensional ion lattices," 2020.

[53] B. Lounis and C. Cohen-Tannoudji, "Coherent population trapping and fano profiles," J. Phys. II France, vol. 2, pp. 579 – 592, 04 1992.

[54] M. J. Biercuk, H. Uys, J. W. Britton, A. P. VanDevender, and J. J. Bollinger, "Ultrasensitive detection of force and displacement using trapped ions.," Nature Nanotechnology, vol. 5, no. 9, pp. 646–650, 2010.

[55] J. Weber, "Observation of the Thermal Fluctuations of a Gravitational-Wave Detector," Physical Review Letters, vol. 17, pp. 1228–1230, dec 1966.

[56] C. M. Caves, "Quantum-Mechanical Radiation-Pressure Fluctuations in an Interferometer," Physical Review Letters, vol. 45, pp. 75–79, jul 1980.

[57] B. P. Abbott et al., "Observation of Gravitational Waves from a Binary Black Hole Merger," Physical Review Letters, vol. 116, no. 6, p. 061102, 2016.

[58] M. Aspelmeyer, T. J. Kippenberg, and F. Marquardt, "Cavity optomechanics," Reviews of Modern Physics, vol. 86, no. 4, pp. 1391–1452, 2014.

[59] D. Wilson, V. Sudhir, N. Piro, R. Schilling, A. Ghadimi, and T. J. Kippenberg, "Measurement-based control of a mechanical oscillator at its thermal decoherence rate," Nature, vol. 524, no. 7565, pp. 325–329, 2015.

[60] N. S. Kampel, R. W. Peterson, R. Fischer, P.-L. Yu, K. Cicak, R. W. Simmonds, K. W. Lehnert, and C. A. Regal, "Improving broadband displacement detection with quantum correlations," Phys. Rev. X, vol. 7, p. 021008, Apr 2017.

[61] S. Schreppler, N. Spethmann, N. Brahms, T. Botter, M. Barrios, and D. M. Stamper-Kurn, "Quantum metrology. Optically measuring force near the standard quantum limit.," Science, vol. 344, no. 6191, pp. 1486–9, 2014.

[62] D. Mason, J. Chen, M. Rossi, Y. Tsaturyan, and A. Schliesser, "Continuous force and displacement measurement below the standard quantum limit," Nature Physics, vol. 15, no. 8, pp. 745–749, 2019.

[63] R. Maiwald, D. Leibfried, J. Britton, J. C. Bergquist, G. Leuchs, and D. J. Wineland, "Stylus ion trap for enhanced access and sensing," Nature Physics, vol. 5, no. 8, pp. 551–554, 2009.

[64] C. Hempel, B. P. Lanyon, P. Jurcevic, R. Gerritsma, R. Blatt, and C. F. Roos, "Entanglement-enhanced detection of single-photon scattering events," Nature Photonics, vol. 7, no. 8, pp. 630–633, 2013.

[65] R. Shaniv and R. Ozeri, "Quantum Lock-in Force Sensing using Optical Clock Doppler," Nature Communications, vol. 8, p. 14157, 2017.

[66] S. C. Burd, R. Srinivas, J. J. Bollinger, A. C. Wilson, D. J. Wineland, D. Leibfried, D. H. Slichter, and D. T. C. Allcock, "Quantum amplification of mechanical oscillator motion," Science, vol. 364, no. 6446, pp. 1163–1165, 2019.

[67] V. Blums, M. Piotrowski, M. I. Hussain, B. G. Norton, S. C. Connell, S. Gensemer, M. Lobino, and E. W. Streed, "A single-atom 3d sub-attonewton force sensor," Science Advances, vol. 4, no. 3, 2018.

[68] J. D. Jost, J. P. Home, J. M. Amini, D. Hanneke, R. Ozeri, C. Langer, J. J. Bollinger, D. Leibfried, and D. J. Wineland, "Entangled mechanical oscillators," Nature, vol. 459, no. 7247, pp. 683–685, 2009.

[69] F. Wolf, C. Shi, J. C. Heip, M. Gessner, L. Pezzè, A. Smerzi, M. Schulte, K. Hammerer, and P. O. Schmidt, "Motional fock states for quantum-enhanced amplitude and phase measurements with trapped ions," Nature communications, vol. 10, no. 1, pp. 1–8, 2019.

[70] W. M. Itano, J. C. Bergquist, J. J. Bollinger, J. M. Gilligan, D. J. Heinzen, F. L. Moore, M. G. Raizen, and D. J. Wineland, "Quantum projection noise: Population fluctuations in two-level systems," Phys. Rev. A, vol. 47, pp. 3554–3570, May 1993.

[71] S. Kotler, N. Akerman, Y. Glickman, A. Keselman, and R. Ozeri, "Single-ion quantum lock-in amplifier," Nature, vol. 473, no. 7345, pp. 61–65, 2011.

[72] J. Johansson, P. Nation, and F. Nori, "Qutip 2: A python framework for the dynamics of open quantum systems," Computer Physics Communications, vol. 184, no. 4, 2013.

[73] W. Ge, B. C. Sawyer, J. W. Britton, K. Jacobs, J. J. Bollinger, and M. Foss-Feig, "Trapped ion quantum information processing with squeezed phonons," Phys. Rev. Lett., vol. 122, p. 030501, Jan 2019.

[74] D. H. Meyer, Z. A. Castillo, K. C. Cox, and P. D. Kunz, "Assessment of rydberg atoms for wideband electric field sensing," Journal of Physics B: Atomic, Molecular and Optical Physics, vol. 53, p. 034001, jan 2020.

[75] A. Facon, E.-K. Dietsche, D. Grosso, S. Haroche, J.-M. Raimond, M. Brune, and S. Gleyzes, "A sensitive electrometer based on a Rydberg atom in a Schrödinger-cat state," Nature, vol. 535, pp. 262–265, jul 2016.

[76] S. Kumar, H. Fan, H. Kübler, J. Sheng, and J. P. Shaffer, "Atom-based sensing of weak radio frequency electric fields using homodyne readout," Scientific Reports, vol. 7, p. 42981, Feb 2017.

[77] C. L. Holloway, J. A. Gordon, S. Jefferts, A. Schwarzkopf, D. A. Anderson, S. A. Miller, N. Thaicharoen, and G. Raithel, "Broadband rydberg atom-based electric-field probe for si-traceable, self-calibrated measurements," IEEE Transactions on Antennas and Propagation, vol. 62, no. 12, pp. 6169–6182, 2014.

[78] F. Toscano, D. A. R. Dalvit, L. Davidovich, and W. H. Zurek, "Sub-planck phase-space structures and heisenberg-limited measurements," Phys. Rev. A, vol. 73, p. 023803, Feb 2006.

[79] R. J. Lewis-Swan and B. D., "Private communication," 2020.

[80] S. Pang and T. A. Brun, "Quantum metrology for a general hamiltonian parameter," Phys. Rev. A, vol. 90, p. 022117, Aug 2014.

[81] L. J. Fiderer and D. Braun, "Quantum metrology with quantum-chaotic sensors," Nature Communications, vol. 9, p. 1351, Apr 2018.

[82] M. Penasa, S. Gerlich, T. Rybarczyk, V. Métillon, M. Brune, J. M. Raimond, S. Haroche, L. Davidovich, and I. Dotsenko, "Measurement of a microwave field amplitude beyond the standard quantum limit," Physical Review A, vol. 94, p. 022313, aug 2016.

[83] P. Arias, D. Cadamuro, M. Goodsell, J. Jaeckel, J. Redondo, and A. Ringwald, "WISPy cold dark matter," Journal of Cosmology and Astroparticle Physics, vol. 2012, no. 06, pp. 013–013, 2012.

[84] D. Horns, J. Jaeckel, A. Lindner, A. Lobanov, J. Redondo, and A. Ringwald, "Searching for WISPy cold dark matter with a dish antenna," Journal of Cosmology and Astroparticle Physics, vol. 2013, pp. 016–016, apr 2013.

[85] S. Chaudhuri, P. W. Graham, K. Irwin, J. Mardon, S. Rajendran, and Y. Zhao, "Radio for hidden-photon dark matter detection," Physical Review D, vol. 92, no. 7, p. 075012, 2015.

[86] W. Ge, B. C. Sawyer, J. W. Britton, K. Jacobs, M. Foss-Feig, and J. J. Bollinger, "Stroboscopic approach to trapped-ion quantum information processing with squeezed phonons," Phys. Rev. A, vol. 100, p. 043417, Oct 2019.

[87] S. C. Burd, R. Srinivas, H. M. Knaack, W. Ge, A. C. Wilson, D. J. Wineland, D. Leibfried, J. J. Bollinger, D. T. C. Allcock, and D. H. Slichter, "Quantum amplification of boson-mediated interactions," 2020.

[88] P. J. Lee, K.-A. Brickman, L. Deslauriers, P. C. Haljan, L.-M. Duan, and C. Monroe, "Phase control of trapped ion quantum gates," Journal of Optics B: Quantum and Semiclassical Optics, vol. 7, pp. S371–S383, sep 2005.

[89] W. M. Itano, J. J. Bollinger, J. N. Tan, B. Jelenković, X.-P. Huang, and D. J. Wineland, "Bragg diffraction from crystallized ion plasmas," Science, vol. 279, no. 5351, pp. 686–689, 1998.

[90] M. L. Wall, A. Safavi-Naini, and A. M. Rey, "Simulating generic spin-boson models with matrix product states," Phys. Rev. A, vol. 94, p. 053637, Nov 2016.

[91] F. Bolton and U. Rössler, "Classical model of a wigner crystal in a quantum dot," Superlattices and Microstructures, vol. 13, no. 2, p. 139, 1993.

[92] L. R. Brewer, J. D. Prestage, J. J. Bollinger, W. M. Itano, D. J. Larson, and D. J. Wineland, "Static properties of a non-neutral ^{9}be$^+$-ion plasma," Phys. Rev. A, vol. 38, pp. 859–873, Jul 1988.

[93] S. L. Gilbert, J. J. Bollinger, and D. J. Wineland, "Shell-structure phase of magnetically confined strongly coupled plasmas," Phys. Rev. Lett., vol. 60, pp. 2022–2025, May 1988.

[94] J. Johansson, P. Nation, and F. Nori, "Qutip: An open-source python framework for the dynamics of open quantum systems," Computer Physics Communications, vol. 183, no. 8, pp. 1760 – 1772, 2012.

[95] S. Peil and G. Gabrielse, "Observing the quantum limit of an electron cyclotron: Qnd measurements of quantum jumps between fock states," Phys. Rev. Lett., vol. 83, pp. 1287–1290, Aug 1999.

[96] H. Perrin, A. Kuhn, I. Bouchoule, and C. Salomon, "Sideband cooling of neutral atoms in a far-detuned optical lattice," EPL (Europhysics Letters), vol. 42, no. 4, p. 395, 1998.

[97] F. Diedrich, J. C. Bergquist, W. M. Itano, and D. J. Wineland, "Laser cooling to the zero-point energy of motion," Phys. Rev. Lett., vol. 62, pp. 403–406, Jan 1989.

[98] M. Hofheinz, M. Ansmann, R. C. Bialczak, M. Lenander, E. Lucero, M. Neeley, D. Sank, H. Wang, M. Weides, J. Wenner, J. M. Martinis, and A. N. Cleland, "Laser cooling to the zero-point energy of motion," Nature, vol. 464, pp. 697–703, 2010.

[99] J. D. Teufel, T. Donner, D. Li, J. W. Harlow, M. S. Allman, K. Cicak, A. J. Sirois, J. D. Whittaker, K. W. Lehnert, and R. W. Simmonds, "Sideband cooling of micromechanical motion to the quantum ground state," Nature, vol. 475, p. 359, 2011.

[100] J. Chan, T. P. M. Alegre, A. H. Safavi-Naeini, J. T. Hill, A. Krause, S. Gröblacher, M. Aspelmeyer, and O. Painter, "Laser cooling of a nanomechanical oscillator into its quantum ground state," Nature, vol. 478, p. 89, 2011.

[101] S. J. Asztalos et al., "SQUID-based microwave cavity search for dark-matter axions," Physical Review Letters, vol. 104, no. 4, p. 041301, 2010.

[102] D. B. Hume, C. W. Chou, D. R. Leibrandt, M. J. Thorpe, D. J. Wineland, and T. Rosenband, "Trapped-ion state detection through coherent motion," Physical Review Letters, vol. 107, no. 24, p. 243902, 2011.

[103] T. Westphal, D. Friedrich, H. Kaufer, K. Yamamoto, S. Goßler, H. Müller-Ebhardt, S. L. Danilishin, F. Y. Khalili, K. Danzmann, and R. Schnabel, "Interferometer readout noise below the standard quantum limit of a membrane," Physical Review A, vol. 85, no. 6, p. 063806, 2012.

[104] C. M. Caves, K. S. Thorne, R. W. P. Drever, V. D. Sandberg, and M. Zimmermann, "On the measurement of a weak classical force coupled to a quantum-mechanical oscillator. I. Issues of principle," Reviews of Modern Physics, vol. 52, no. 2, pp. 341–392, 1980.

[105] P. A. Ivanov, "Force sensors with precision beyond the standard quantum limit," Physical Review A, vol. 94, no. 2, p. 022330, 2016.

[106] J. B. Clark, F. Lecocq, R. W. Simmonds, J. Aumentado, and J. D. Teufel, "Observation of Strong Radiation Pressure Forces from Squeezed Light on a Mechanical Oscillator," arXiv preprint arXiv:1601.02689v1, vol. 12, no. 1, pp. 683–687, 2016.

[107] G. Anetsberger, E. Gavartin, O. Arcizet, Q. P. Unterreithmeier, E. M. Weig, M. L. Gorodetsky, J. P. Kotthaus, and T. J. Kippenberg, "Measuring nanomechanical motion with an imprecision below the standard quantum limit," Physical Review A, vol. 82, p. 061804, dec 2010.

[108] S. Knünz, M. Herrmann, V. Batteiger, G. Saathoff, T. W. Hänsch, K. Vahala, and T. Udem, "Injection locking of a trapped-ion phonon laser," Physical Review Letters, vol. 105, no. 1, p. 013004, 2010.

[109] H. Fan, S. Kumar, J. Sedlacek, H. Kübler, S. Karimkashi, and J. P. Shaffer, "Atom based RF electric field sensing," Journal of Physics B: Atomic, Molecular and Optical Physics, vol. 48, no. 20, p. 202001, 2015.

[110] G. Anetsberger, O. Arcizet, Q. P. Unterreithmeier, R. Rivière, A. Schliesser, E. M. Weig, J. P. Kotthaus, and T. J. Kippenberg, "Near-field cavity optomechanics with nanomechanical oscillators," Nature Physics, vol. 5, pp. 909–914, dec 2009.

[111] A. A. Clerk, M. H. Devoret, S. M. Girvin, F. Marquardt, and R. J. Schoelkopf, "Introduction to quantum noise, measurement, and amplification," Reviews of Modern Physics, vol. 82, no. 2, pp. 1155–1208, 2010.

[112] S. Kotler, N. Akerman, Y. Glickman, and R. Ozeri, "Nonlinear single-spin spectrum analyzer," Physical Review Letters, vol. 110, no. 11, p. 110503, 2013.

[113] H.-J. Butt, B. Cappella, and M. Kappl, "Force measurements with the atomic force microscope: Technique, interpretation and applications," Surface Science Reports, vol. 59, pp. 1–152, oct 2005.

[114] R. W. Peterson, T. P. Purdy, N. S. Kampel, R. W. Andrews, P. L. Yu, K. W. Lehnert, and C. A. Regal, "Laser Cooling of a Micromechanical Membrane to the Quantum Backaction Limit," Physical Review Letters, vol. 116, no. 6, pp. 1–6, 2016.

[115] D. H. E. Dubin, "Theory of structural phase transitions in a trapped coulomb crystal," Phys. Rev. Lett., vol. 71, pp. 2753–2756, Oct 1993.

[116] P. A. Ivanov, N. V. Vitanov, and K. Singer, "High-precision force sensing using a single trapped ion," Sci Rep, vol. 28078, no. 8, 2016.

[117] M. J. Biercuk, H. Uys, J. W. Britton, A. P. VanDevender, and J. J. Bollinger, "Phase-coherent detection of an optical dipole force by Doppler velocimetry.," Optics Express, vol. 19, no. 11, pp. 10304–10316, 2011.

[118] T. A. Palomaki, J. W. Harlow, J. D. Teufel, R. W. Simmonds, and K. W. Lehnert, "Coherent state transfer between itinerant microwave fields and a mechanical oscillator.," Nature, vol. 495, no. 7440, pp. 210–4, 2013.

[119] D. Horns, J. Jaeckel, A. Lindner, A. Lobanov, J. Redondo, and A. Ringwald, "Searching for WISPy Cold Dark Matter with a Dish Antenna," arXiv, p. 16, 2012.

[120] P. H. Kim, B. D. Hauer, C. Doolin, F. Souris, and J. P. Davis, "Approaching the Standard Quantum Limit of Mechanical Torque Sensing," Nature Communications, vol. 7, p. 25, 2016.

[121] J. D. Teufel, T. Donner, M. A. Castellanos-Beltran, J. W. Harlow, and K. W. Lehnert, "Nanomechanical motion measured with precision beyond the standard quantum limit," Nature Nanotechnology, vol. 4, no. 12, p. 820, 2009.

Appendix A

Off-resonance sensing derivations

This appendix provides some derivations and details pertinent to Ch. 6. It is reproduced from the supplementary information of [18].

A.1   CPMG lineshape derivation

For simplicity, we first derive the lineshape for the $m = 2$ CPMG sequence (Fig. A.1). For a delta function source $Z_c \cos(\omega t + \delta)$, the spin precession accumulated in a general sequence like that shown in Fig. A.1 is

$$\theta(\mu) = F_0 \, Z_c \frac{2 \sin\left(\frac{1}{2}\left(\omega - \mu\right) T\right)}{(\omega - \mu)} \chi(\mu, \omega), \tag{A.1}$$

where $\chi(\mu, \omega) = \sum_i \chi_i(\mu, \omega)$ is determined by the particular sequence used. In the case of the $m = 2$ CPMG sequence, the phase accumulated through four terms corresponding to four separate applications of the ODF (Fig. A.1) must be considered:

$$\chi_1 = \cos\left[(\omega - \mu)\frac{T}{2} + \delta - \phi\right], \tag{A.2}$$

$$\chi_2 = -\cos\left[(\omega - \mu)\left(\frac{3T}{2} + t_\pi\right) + \delta - \phi + \mu(T + t_\pi)\right], \tag{A.3}$$

$$\chi_3 = -\cos\left[(\omega - \mu)\left(\frac{5T}{2} + t_\pi\right) + \delta - \phi + \mu(T + t_\pi)\right], \tag{A.4}$$
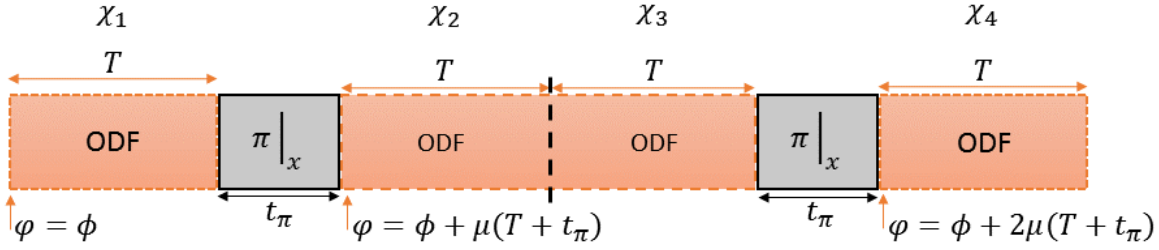
Figure A.1: $m = 2$ CPMG sequence with total ODF interaction time $4T$. φ is the phase of the ODF beatnote. The χ_i labels represent the periods over which the accumulated phase is considered in the text.

$$\chi_4 = \cos\left[(\omega - \mu)\left(\frac{7T}{2} + 2t_\pi\right) + \delta - \phi + 2\mu(T + t_\pi)\right]. \tag{A.5}$$

Note these terms now include a phase ϕ for the ODF interaction, which in the previous section was set to zero with no loss of generality. Adding these terms up, pairwise:

$$\chi_1 + \chi_2 = 2\sin\left(\frac{1}{2}\left[(\omega - \mu)(T + t_\pi) + \mu(T + t_\pi)\right]\right) \tag{A.6}$$

$$\sin\left[(\omega - \mu)\left(T + \frac{t_\pi}{2}\right) + \delta - \phi + \frac{\mu(T + t_\pi)}{2}\right], \tag{A.7}$$

$$\chi_3 + \chi_4 = -2\sin\left(\frac{1}{2}\left[(\omega - \mu)(T + t_\pi) + \mu(T + t_\pi)\right]\right) \tag{A.8}$$

$$\sin\left[(\omega - \mu)\left(3T + \frac{3t_\pi}{2}\right) + \delta - \phi + \frac{3\mu(T + t_\pi)}{2}\right]. \tag{A.9}$$

Summing all four terms yields

$$\chi(\mu, \omega) = \sum_i \chi_i(\mu, \omega) = 2\sin\left(\frac{\omega}{2}(T + t_\pi)\right)\left[\sin(\xi + \delta - \phi) - \sin(3\xi + \delta - \phi)\right], \tag{A.10}$$

where $\xi = (\omega - \mu)(T + \frac{t_\pi}{2}) + \frac{\mu(T + t_\pi)}{2} = \frac{1}{2}(\omega(T + t_\pi) + T(\omega - \mu))$. Then, simplifying:

$$\chi(\mu, \omega) = 2\sin\left(\frac{\omega}{2}(T + t_\pi)\right)2\sin(-\xi)\cos(2\xi + \delta - \phi). \tag{A.11}$$

Using Eqs. 13 and 5,

$$\theta(\mu) = DWF \cdot U \cdot \delta k \cdot Z_c \cdot T\operatorname{sinc}\left(\frac{T}{2}(\omega - \mu)\right)4\sin\left(\frac{\omega}{2}(T + t_\pi)\right)\sin(\xi)\cos(2\xi + \delta - \phi). \tag{A.12}$$

Since $4T = \tau$ for the $m = 2$ CPMG, then

$$\theta(\mu) = \theta_{max} \operatorname{sinc}\left(\frac{T}{2}\left(\omega - \mu\right)\right) \sin\left(\frac{\omega}{2}\left(T + t_\pi\right)\right) \sin\left(\xi\right) \cos\left(2\xi + \delta - \phi\right), \tag{A.13}$$

where $\theta_{max} \equiv (F_0/\hbar) Z_c \tau$, the maximum precession angle on resonance as defined in the previous section. Then, $\theta_{max}(\mu)$, defined as $\theta(\mu) = \theta_{max}(\mu) \cos\left(2\xi + \delta - \phi\right)$, is the μ-dependent generalization of θ_{max}. From Eq. (A.13), this is

$$\theta_{max}(\mu) = \theta_{max} \operatorname{sinc}\left(\frac{T}{2}\left(\omega - \mu\right)\right) \sin\left(\frac{\omega}{2}\left(T + t_\pi\right)\right) \sin\left(\xi\right). \tag{A.14}$$

For the $m = 8$ CPMG sequence the same procedure is used, but now with 16 periods of accumulated phase. We obtain

$$\theta_{max}(\mu) = \theta_{max} \operatorname{sinc}\left(\frac{T}{2}\left(\omega - \mu\right)\right) \sin\left(\frac{\omega}{2}\left(T + t_\pi\right)\right) \sin(\xi) \cos(2\xi) \cos(4\xi). \tag{A.15}$$

A.2   Phase-incoherent sensing limits

Here we derive Eq. (5) from the main text and provide additional mathematical background for the phase-incoherent experimental protocol, wherein the phase of the measured quadrature varies randomly from one iteration of the experimental sequence to the next. Following earlier discussions, the probability of measuring $|\uparrow\rangle$ at the end of the Ramsey sequence is

$$\langle P_\uparrow \rangle = \frac{1}{2}\left[1 - e^{-\Gamma\tau} J_0\left(\theta_{max}\right)\right], \tag{A.16}$$

where $\langle\,\rangle$ denotes an average over many experimental trials and therefore over the random phase between the 1D traveling-wave potential and the classically driven COM motion, and

$$\theta_{max} = (F_0/\hbar) \cdot Z_c \cdot \tau. \tag{A.17}$$

Defining $G\left(\theta_{max}^2\right) \equiv \left(1 - J_0\left(\theta_{max}\right)\right)/2$ and denoting $\langle P_\uparrow \rangle_{bck} = \left[1 - e^{-\Gamma\tau}\right]/2$ as the probability of measuring $|\uparrow\rangle$ at the end of the sequence in the absence of a classically driven motion, θ_{max}^2 can be determined from a measurement of the difference $\langle P_\uparrow \rangle - \langle P_\uparrow \rangle_{bck}$ through

$$G\left(\theta_{max}^2\right) = e^{\Gamma\tau}\left(\langle P_\uparrow \rangle - \langle P_\uparrow \rangle_{bck}\right). \tag{A.18}$$

The standard deviation $\delta\theta^2_{max}$ in estimating θ^2_{max} is determined from the standard deviation $\sigma\left(P_\uparrow - P_{\uparrow,bck}\right)$ of the $\langle P_\uparrow \rangle - \langle P_\uparrow \rangle_{bck}$ difference measurements through

$$\delta\theta^2_{max} = \frac{e^{\Gamma\tau}\sigma\left(\langle P_\uparrow \rangle - \langle P_\uparrow \rangle_{bck}\right)}{\frac{\mathrm{d}G(\theta^2_{max})}{\mathrm{d}\theta^2_{max}}} \ . \tag{A.19}$$

The signal-to-noise ratio of a measurement of θ^2_{max} (and therefore Z^2_c) is $\theta^2_{max}/\delta\theta^2_{max} = Z^2_c/\delta Z^2_c$. In general this signal-to-noise ratio depends on θ^2_{max} and the experimental parameters $U \cdot \tau$, $\Gamma \cdot \tau$, δk, and N.

We use Eq. (A.19) to theoretically estimate $Z^2_c/\delta Z^2_c$ and the amplitude sensing limits. We assume the only sources of noise are projection noise in the measurement of the spin state and fluctuations in $P_\uparrow$ due to the random variation in the relative phase of the 1D traveling-wave potential and the driven COM motion. Experimentally this is obtained by collecting 10 photons for each $|\uparrow\rangle$ state, so photon counting shot noise can be neglected [14]. In this case $\sigma\left(P_\uparrow - P_{\uparrow,bck}\right) = \sqrt{\sigma^2_{P_\uparrow} + \sigma^2_{P_{\uparrow,bck}}}$ where the relevant variances are

$$\sigma^2_{P_{\uparrow,bck}} = \frac{1}{N}\langle P_\uparrow \rangle_{bck}\left(1 - \langle P_\uparrow \rangle_{bck}\right) = \frac{1}{4N}\left(1 - e^{-2\Gamma\tau}\right) \tag{A.20}$$

and

$$\sigma^2_{P_\uparrow} = \sigma^2_\delta + \frac{1}{N}\langle P_\uparrow \rangle\left(1 - \langle P_\uparrow \rangle\right) \ . \tag{A.21}$$

Here N is the number of spins. Equation (A.20) and the second term in Eq. (A.21) are projection noise. The variance

$$\sigma^2_\delta = \left\langle P^2_\uparrow - \langle P_\uparrow \rangle^2 \right\rangle = \frac{e^{-2\Gamma\tau}}{8}\left(1 + J_0\left(2\theta_{max}\right) - 2J_0\left(\theta_{max}\right)^2\right) \tag{A.22}$$

is due to the random variation in the relative phase of the 1D traveling-wave and the driven COM motion. For our set-up, $DWF = \exp(-\delta k^2 \langle \hat{z}^2_i \rangle /2) = 0.86$ and $\delta k = 2\pi/\left(900\,\mathrm{nm}\right)$ are fixed, the decoherence Γ is a function of U, $\Gamma = \xi\left(U/\hbar\right)$ where $\xi = 1.156 \times 10^{-3}$, and $F_0 = DWF \cdot U \cdot \delta k$. For a given Z_c we use Eqs. (A.17) and (A.19)-(A.22) to find the optimum $Z^2_c/\delta Z^2_c$ as a function of $(U\tau)/\hbar$. This optimum value is the red dashed theoretical curve plotted in Fig. 6.14 of the main text.

The signal-to-noise $Z_c^2/\delta Z_c^2$ is optimized for relatively small values of θ_{max}^2 where $G\left(\theta_{max}^2\right) \approx$ $\theta_{max}^2/8$ is a good approximation. This leads to some simplifications for Eqs. (A.18) and (A.19),

$$\theta_{max}^2 \approx 8e^{\Gamma\tau}\left(\langle P_\uparrow\rangle - \langle P_\uparrow\rangle_{bck}\right) \tag{A.23}$$

and

$$\delta\theta_{max}^2 \approx 8e^{\Gamma\tau}\sigma\left(P_\uparrow - P_{\uparrow,bck}\right) , \tag{A.24}$$

and to the following estimate for the signal-to-noise ratio of a single experimental trial,

$$\frac{\theta_{max}^2}{\delta\theta_{max}^2} = \frac{Z_c^2}{\delta Z_c^2} \approx \frac{\langle P_\uparrow\rangle - \langle P_\uparrow\rangle_{bck}}{\sigma\left(P_\uparrow - P_{\uparrow,bck}\right)} . \tag{A.25}$$

Figure 6.14 of the main text uses Eq. (A.25), along with repeated measurements of $P_\uparrow - P_{\uparrow,bck}$, to experimentally determine the signal-to-noise ratio as a function of the imposed amplitude Z_c of the COM motion.

Finally we use Eqs. (A.17) and (A.19)-(A.22) to calculate the sensing limits for very small Z_c. For small Z_c the variance σ_δ^2 can be neglected compared to projection noise and $\sigma_{P_\uparrow}^2 \approx \sigma_{P_{\uparrow,bck}}^2$. In this case we obtain the following expression for the signal-to-noise ratio,

$$\frac{Z_c^2}{\delta Z_c^2} = \frac{\sqrt{N}}{4\sqrt{2}}\frac{DWF^2\cdot(\delta k\,Z_c)^2\,(U\tau/\hbar)^2}{\sqrt{e^{2\xi U\tau/\hbar}-1}} . \tag{A.26}$$

Equation (A.26) is maximized for $\xi U\tau \approx 1.9603$, resulting in

$$\left.\frac{Z_c^2}{\delta Z_c^2}\right|_{limiting} \approx 0.097\frac{\sqrt{N}(DWF)^2(\delta k)^2}{\xi^2}Z_c^2 , \tag{A.27}$$

which is Eq. 6.13 of the main text. With $DWF = 0.86$, $\delta k = 2\pi/(900\,\mathrm{nm})$, $\xi = 1.156\times 10^{-3}$, and $N = 85$,

$$\left.\frac{Z_c^2}{\delta Z_c^2}\right|_{optimum} = \left[\frac{Z_c}{0.2\,\mathrm{nm}}\right]^2 . \tag{A.28}$$

For our set-up and available ODF power, $\xi U\tau/\hbar \approx 1.9603$ is realized for $\tau \approx 20\,\mathrm{ms}$. A measurement of the signal and a measurement of the background requires ~ 60 ms, allowing for 16 independent measurements of $P_\uparrow - P_{\uparrow,bck}$ in 1 s. The limiting sensitivity is approximately $(100\,\mathrm{pm})^2$ in a 1 s measurement time, or $(100\,\mathrm{pm})^2/\sqrt{\mathrm{Hz}}$. We note that the limiting sensitivity is determined by the ratio $\xi = \Gamma/(U/\hbar)$. In particular, the optimum value for Eq. (A.26) scales as $1/\xi^2$.

A.3 Phase-coherent sensing limits

With appropriate care the phase of the 1D traveling-wave potential can be stable for long periods of time with respect to the ion trapping electrodes [102], enabling repeated phase-coherent sensing of the same quadrature of the COM motion $Z_c \cos(\omega t)$. In this case the same spin precession $\theta_{max} = DWF \cdot (U/\hbar) \cdot \delta k\, Z_c \cdot \tau$ occurs for each experimental trial, which can be detected to first order in θ_{max} (or Z_c) in a Ramsey sequence with a $\pi/2$ phase shift between the two $\pi/2$-pulses. Assuming $\sin(\theta_{max}) \approx \theta_{max}$, appropriate for small amplitudes Z_c, the equivalent phase-coherent sensing expressions for Eqs. (A.23) and (A.24) are

$$\theta_{max} = 2e^{\Gamma \tau} \left(\langle P_\uparrow \rangle - \langle P_\uparrow \rangle_{bck} \right) \tag{A.29}$$

and

$$\delta\theta_{max} = 2e^{\Gamma \tau} \sigma \left(P_\uparrow - P_{\uparrow,bck} \right) . \tag{A.30}$$

For a Ramsey experiment with a $\pi/2$ phase shift, $\langle P_\uparrow \rangle_{bck} = 1/2$. If projection noise is the only source of noise, then for small Z_c, $\sigma^2_{P_\uparrow} \approx \sigma^2_{P_{\uparrow,bck}} = \frac{1}{N} \cdot \frac{1}{2} \cdot \frac{1}{2}$ and $\sigma\left(P_\uparrow - P_{\uparrow,bck} \right) \approx \frac{1}{\sqrt{2N}}$. The limiting signal-to-noise ratio $\theta_{max}/\delta\theta_{max}$ of a $\left(P_\uparrow - P_{\uparrow,bck} \right)$ measurement is

$$\frac{\theta_{max}}{\delta\theta_{max}} = \frac{Z_c}{\delta Z_c} = DWF \cdot (\delta k\, Z_c) \cdot \sqrt{\frac{N}{2}} \cdot \frac{(U\tau)}{\hbar} e^{-\xi U \tau/\hbar} . \tag{A.31}$$

Equation (A.31) is maximized for $\xi U \tau/\hbar = 1$. With $DWF = 0.86$, $\delta k = 2\pi/(900\,\text{nm})$, $\xi = 1.156 \times 10^{-3}$, and $N = 100$,

$$\left. \frac{Z_c}{\delta Z_c} \right|_{optimum} = \frac{Z_c}{0.074\,\text{nm}} . \tag{A.32}$$

With 16 independent measurements of $\langle P_\uparrow \rangle - \langle P_\uparrow \rangle_{bck}$ in 1 s, this corresponds to a limiting sensitivity of $\sim (20\,\text{pm})/\sqrt{\text{Hz}}$. The optimum value for the signal-to-ratio of Eq. (A.31) scales as $1/\xi$.